The Measurement of the Neutral Current Interaction at the Sudbury Neutrino Observatory

Gordon Allan McGregor
Merton College, Oxford University

Thesis submitted in partial fulfilment of the requirements
for the degree of Doctor of Philosophy
at the University of Oxford
Hilary Term 2002

The Measurement of the Neutral Current Interaction at the Sudbury Neutrino Observatory

Gordon Allan McGregor
Merton College, Oxford University

Thesis submitted for the degree of Doctor of Philosophy
Hilary Term 2002

Abstract

The Sudbury Neutrino Observatory (SNO) is a 1 kilotonne heavy water Čerenkov detector. SNO is able to separately determine the flux of electron neutrinos and the flux of all active neutrinos from the Sun by measuring the rate of neutrino charged current (CC) and neutral current (NC) interactions with deutrons.

This thesis first describes a method that removes a rate dependence in the photo-multiplier time calibration. This was essential for the first SNO publication of the CC neutrino flux and will be used in the determination of the NC neutrino flux. The model used in this correction is discussed and the resulting reconstruction performance presented.

To enhance the NC signal, ^{35}Cl is added to the D_2O. NaCl was considered as a possible additive containing ^{35}Cl and an investigation of the production of ^{24}Na in the D_2O recirculation loop is described. ^{24}Na production was found to be tolerably low and this resulted in the decision to add NaCl to the D_2O. This addition gave the possibility of producing ^{24}Na within the D_2O as a low energy container-less calibration source. The analysis of such a source is presented.

Upgrading of the neutron transport code in SNOMAN, the SNO collaboration's official Monte Carlo package, to fulfil all outstanding requirements is described and detailed. Comparisons of simulated neutron transport with data are presented. Agreement is very good, with the overall neutron capture efficiency predicted to better than 5%.

These analyses are combined with a method which evaluates the levels of radioactive contaminants in the D_2O. This allows the neutral current interaction background from photodisintegration in the D_2O to be calculated. This background is $317.0\pm34.8(stat.)\pm60.8(sys.)$ neutrons in the entire D_2O dataset, which is equivalent to $0.077\pm0.008(stat.)\pm0.015(sys.)$ BP2000 SSM.

Finally, the full 307.1 days of D_2O data from SNO is analysed giving a NC flux of $1.59\pm0.42(stat.)\pm0.12(sys.)$ BP2000 SSM. When combined with the CC flux measurement from SNO, this result is evidence at the 2.8σ level that solar neutrinos oscillate to active flavours during their journey to the Earth and that the predicted BP2000 SSM ^{8}B neutrino flux is correct.

To my parents

Acknowledgements

Firstly, I would like to thank my supervisor Nick Jelley for his unwavering support, encouragement and guidance. He has been instrumental in the completion of this thesis. I also wish to thank the other members of the Oxford group: Dave Wark, Steve Biller, George Doucas, Kate Frame, Xiongxin Dai, Nick West (a.k.a. Mr. SNOMAN) and Mike Bowler (who started me on this path as an undergraduate many years ago). Their combined knowledge, enthusiasm and sense of humour (cludeo anyone?) has made working with them a pleasure.

Beverly Roger deserves my thanks for organising my frequent visits to Sudbury, and Shari Moss for helping me when I got there. Thanks also to Pete Gronbech for ensuring that I could always rely on the computer systems at Oxford.

James Cameron and Neil McCauley, my fellow graduate students, have both made working on SNO much more enjoyable. James was always ready to tutor me in the ways of PAW, and spend the occasional day on the slopes or the fairways.

Derek Sweezey, John Roberts, Carol Woodliffe and Hadi Fergani all made life in Sudbury more enjoyable. Thanks also to the entire PENN group, Rich Helmer and Mike Dragowsky.

My parents have been a constant source of love and support, not only for the duration of this thesis, but for my entire life. I cannot thank them enough. This thesis is dedicated to them.

Finally, I would like to thank Ha for all her love, support and patience, especially in the last weeks of writing. I look forward to spending the rest of my life with her.

Thesis Overview

This thesis discusses work done by the author on a wide range of topics for the SNO collaboration directed towards the measurement of the neutral current interaction. A short overview of this thesis now follows:

Chapter 1 begins with an overview of the rich subject of solar neutrinos and presents the 30 year old enigma of the solar neutrino problem. A brief discussion of neutrino oscillations is given, and the results prior to the SNO experiment summarised.

Chapter 2 describes the SNO experiment in some detail and presents the first results from the SNO collaboration, published on 18th June, 2001.

Chapter 3 presents the History Calibration (HCA). This is a PMT timing calibration which was written by the author. It removes the PMT timing calibration dependence on the PMT readout history. Utilising the HCA, reconstruction of high and low rate calibration sources is considered and their puzzling behaviour explained. Confidence in the PMT timing calibration is restored, allowing the uncertainties in neutrino reconstruction to be estimated.

Chapter 4 presents a comparison between neutron data (taken after salt had been added to the D_2O) and SNOMAN, the official collaboration Monte Carlo package. The author has been responsible for the neutron transport code in SNOMAN from the commencement of this thesis and a considerable amount of effort has been spent by the author upgrading the code after its initial implementation. Comparisons between data and SNOMAN show good agreement which should be improved further when more precise optical and energy calibrations become available.

Chapter 5 presents a Monte Carlo study to estimate the amount of ^{24}Na that would be produced in the D_2O recirculation loop if NaCl was used as the salt additive in the salt phase of the experiment. ^{24}Na production is found to be acceptably low, leading to the approval and deployment of NaCl in the D_2O on 28th May, 2001.

Chapter 6 presents the analysis of activated ^{24}Na in the D_2O. This was an unanticipated benefit of adding NaCl to the D_2O. Good agreement between this low energy source and SNOMAN is found, giving confidence in the ability to simulate the low energy $\beta\gamma$ events of ^{208}Tl and ^{214}Bi. The total ^{24}Na produced in the detector is determined using two techniques and when compared with predictions from SNOMAN allowed the uncertainty in the overall normalisation for low energy events to be estimated.

Chapter 7 presents a method of determining the number of ^{208}Tl and ^{214}Bi decays within the D_2O using the Čerenkov light produced in the $\beta\gamma$ decays of these particles. From this the number of neutrons produced by D_2O based radioactivity is calculated. This is crucial to the accurate measurement of the neutral current interaction rate.

Chapter 8 presents such a measurement using the extended likelihood method. It is not a final analysis of the SNO D_2O data, and serves more as an illustration of the usage of the results of chapter 7 and to whet the appetite for the upcoming SNO collaboration results.

Finally, chapter 9 summarises the significant conclusions of this thesis.

Contents

Chapter 1

Solar Neutrinos

1.1 The Neutrino

In 1930, Wolfgang Pauli postulated the existence of the neutrino to explain the continuous energy spectra of electrons emitted in nuclear beta decay. Within the Standard Model of particle physics, the neutrino is the electro-weak partner of the charged lepton. Three neutrinos are included in the standard model: the electron, muon and tau neutrinos (ν_e, ν_μ, ν_τ).

All the neutrinos within the standard model have been observed via their interactions with matter[1], and measurements of the width of the Z° boson at LEP [2] indicate that there are only three active neutrinos with masses less than half of the Z° boson.

Neutrinos are unique among the fundamental fermions in that they carry no electric or colour charge, and therefore only interact via the weak force (and gravity). They are assumed to be massless, with upper limits on their masses of: m_{ν_e}<2.2 eV [3][4], m_{ν_μ}<0.19 MeV [5] and m_{ν_τ}<15.5 MeV[6]. These limits are determined from the kinematics of decays in which neutrinos are produced.

The mass of the electron neutrino can be constrained further by studies of

[1]The tau neutrino has recently been observed by the DONUT experiment [1].

neutrinoless double β-decay, the upper limit then becoming $m_{\nu_e}<0.4\,\mathrm{eV}$ [7]. This assumes that neutrinos are Majorana particles: they are their own antiparticle.

1.2 The Sun and Standard Solar Models

The Sun is a main sequence star around 4.6 billion years old. The only types of processes capable of sustaining the Sun for such a long period of time are nuclear reactions. In the Sun, this is the conversion of hydrogen to helium.

$$2e^- + 4\mathrm{p} \;\rightarrow\; {}^4\mathrm{He} + 2\nu_e + 26.7\,\mathrm{MeV} \tag{1.1}$$

The two neutrinos in equation 1.1 carry away on average 0.6 MeV. 98.5% of the energy produced by the Sun is from the *pp* chain, shown in figure 1.1, with the remaining 1.5% from the CNO cycle.

Several standard solar models (SSM) of the Sun exist. In these models the Sun is modelled as a spherical body in hydrostatic equilibrium, with the radiative and particle outward pressures supporting the inward pressures due to gravity. This assumption is well justified as the time scale for gravitational collapse of the Sun is about an hour.

The Bahcall Pinsonneault 2000 (BP2000) SSM [9] (one of the most widely used SSMs) is constructed with the OPAL [10] equation of state and OPAL radiative opacities. It uses nuclear reaction data, with electron and ion weak screening effects taken into account, and incorporates helium and heavy element diffusion.

The current state of the Sun is calculated by recursively numerically solving and evolving a coupled set of differential equations from the time the Sun began burning hydrogen to the present day. The initial conditions, such as the initial abundance of hydrogen and helium, are varied to maximise the agreement between

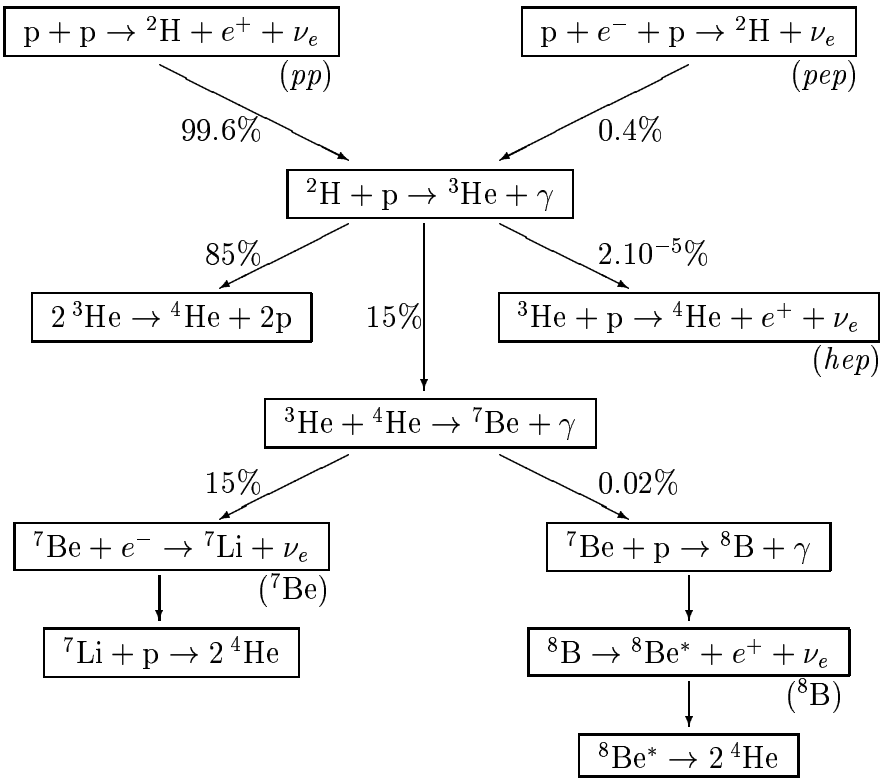

Figure 1.1: The *pp* chain [8].

the model and present day observations, such as the luminosity, radius, surface temperature and the surface heavy element to hydrogen ratio.

One of the greatest triumphs of the BP2000 SSM is the level of agreement with the predictions made in the field of helioseismology (no helioseismology data is used to constrain the SSM). Helioseismology is the study of the acoustic waves supported in the Sun between its surface and the base of the convective zone. By studying the effects that the supported modes have on the surface of the Sun, the speed of sound in the interior of the Sun can be calculated. Figure 1.2 shows a comparison between the BP2000 SSM predicted speed of sound, and the measured values obtained with the combination of BiSON (Birmingham Solar Oscillation Network) and LOWL1 (the Low-l instrument). The agreement is better than

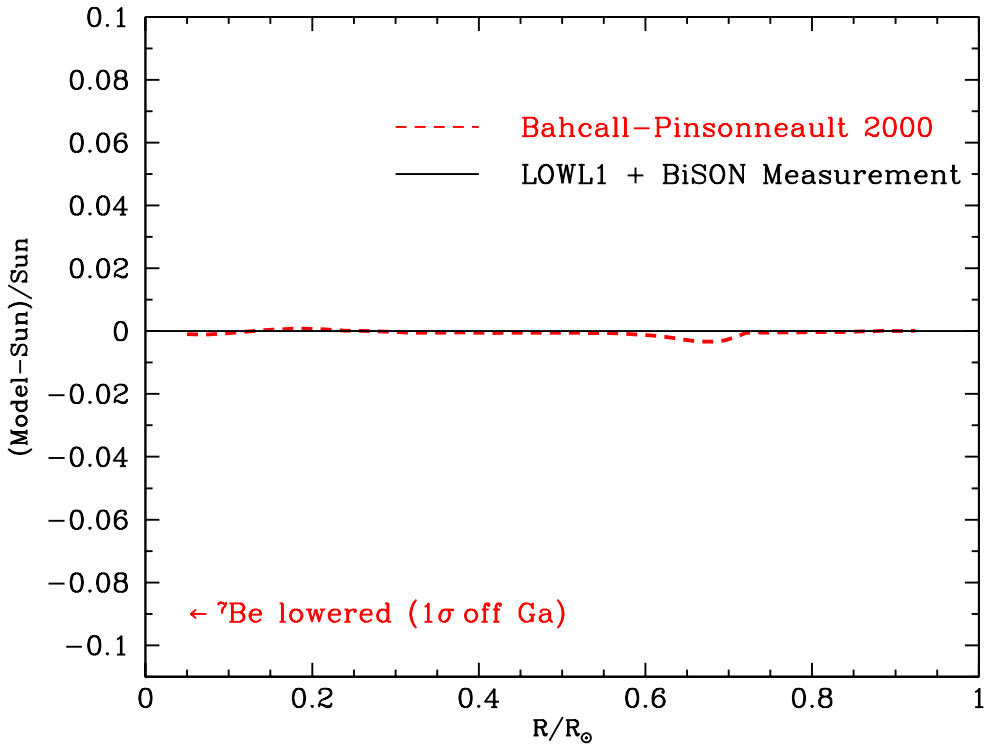

Figure 1.2: A comparison of the predicted (BP2000) and measured (helioseismology) sound speeds as a function of radius. There is excellent agreement over all radii, including the deep interior region, $r \leq 0.25 R_{\odot}$, in which neutrinos are produced. Also shown is the level of disagreement required to account for the gallium results (see section 1.3.1). Taken from [9].

0.1% at all solar radii, which gives confidence that the model is indeed describing both the interior and exterior of the Sun correctly.

Among the many predictions made by solar models is the neutrino flux from the Sun. Neutrinos, born in the core of the Sun, provide a means to probe the interior directly. They also escape the Sun quickly, arriving at the Earth approximately 8 minutes after their creation. This is in stark contrast with light from the Sun, which can take tens of thousands of years to exit the Sun.

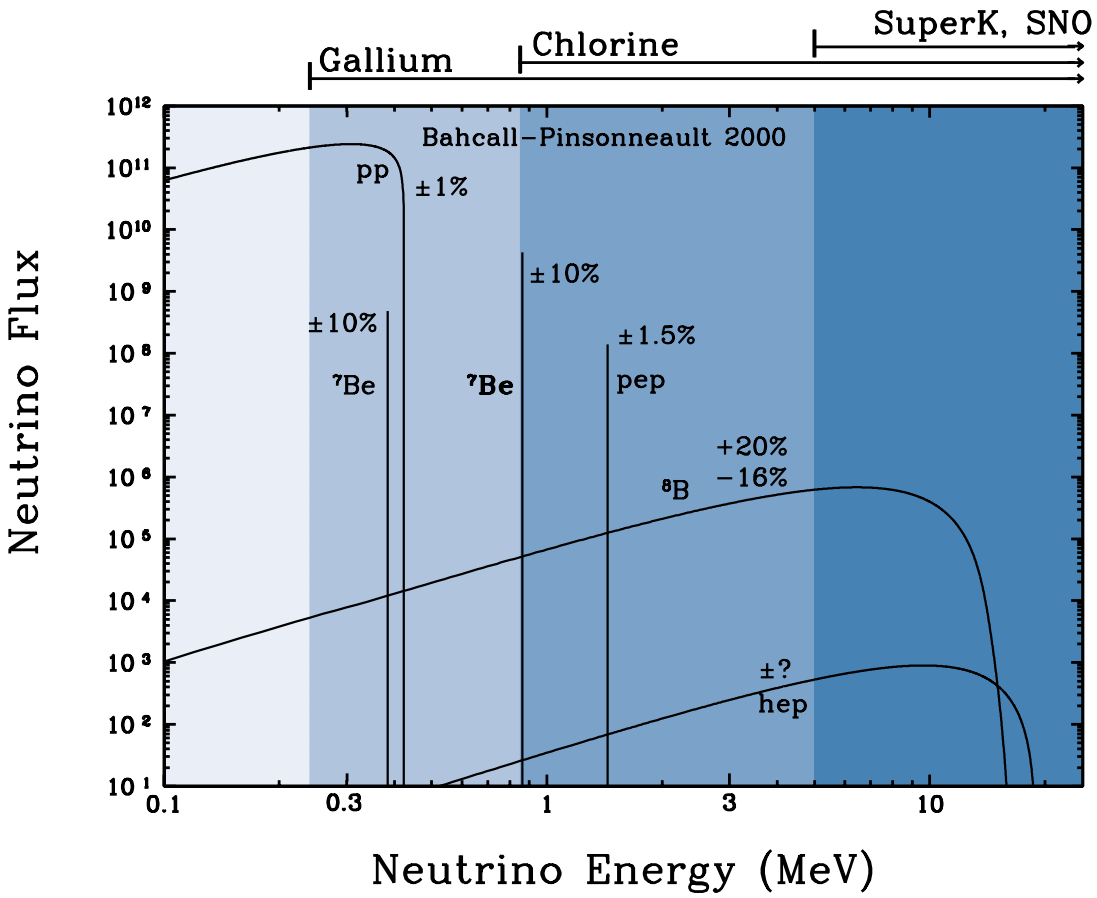

Figure 1.3: The BP2000 standard solar model prediction of solar neutrino energy spectra. Errors correspond to 1σ uncertainties. Fluxes from continuum sources are given in neutrinos per cm^2 per second per MeV. Line fluxes are given in neutrinos per cm^2 per second. All fluxes are for a distance of one astronomical unit. Experimental energy thresholds are also shown. Taken from [11].

1.3 Solar Neutrino Experiments

Figure 1.3 shows the predicted neutrino flux from the BP2000 SSM. Since 1967, experiments have been conducted to measure these fluxes.

Because neutrinos interact weakly they are very difficult to detect. To overcome this problem, neutrino detectors usually employ large target masses and accumulate data over long periods of time. Of the neutrino experiments that

have been built to date, there are two distinct types: radiochemical experiments and water Čerenkov experiments.

1.3.1 Radiochemical Experiments

Radiochemical experiments utilise a target material which neutrinos interact with to produce a different element. The target material is typically exposed for a period of several weeks and then assayed for the element produced. The integrated neutrino flux can then be inferred but no spectral (other than threshold), directional or time variation (shorter than the exposure time) information is obtained.

When presenting results, radiochemical experiments commonly use Solar Neutrino Units (SNU). One SNU is equal to 10^{-36} captures per target atom per second.

The Homestake Chlorine Experiment

The first experiment to detect solar neutrinos was pioneered by Ray Davis Jr. and used ^{37}Cl as the target [12]. The experiment was located in the Homestake Gold Mine, South Dakota, at a depth of 4850 feet. 615 tonnes of C_2Cl_4 was used as the target material. The neutrino interaction utilised was the conversion of ^{37}Cl into ^{37}Ar:

$$\nu_e + {}^{37}\mathrm{Cl} \;\rightarrow\; e^- + {}^{37}\mathrm{Ar}$$

This reaction has a threshold of 0.814 MeV and is therefore sensitive to all solar neutrinos except the lower ^{7}Be line and the *pp* neutrinos. An analysis of 108 extractions made between April 1970 and May 1994 [12] gives a capture rate of:

$$2.56 \pm 0.16(stat.) \pm 0.16(sys.)\ \mathrm{SNU}$$

The BP2000 SSM [9] predicts a capture rate of:

$$7.6^{+1.3}_{-1.1}\ \mathrm{SNU}$$

The Gallium Experiments: SAGE, GALLEX and GNO

Gallium experiments, three of which have been undertaken to date, are very similar in principle to the chlorine experiment. The interaction utilised is the conversion of ^{71}Ga into ^{71}Ge:

$$\nu_e + {}^{71}\mathrm{Ga} \;\rightarrow\; e^- + {}^{71}\mathrm{Ge}$$

This reaction has a threshold of 0.233 MeV and therefore the gallium experiments are sensitive to all sources of solar neutrinos. This is very important, as the *pp* flux is very tightly constrained by luminosity measurements and predicted with a very low uncertainty ($\sim$1%).

Although all three experiments utilise the same interaction, the form of the gallium target differs considerably (between SAGE and the other two). This makes the systematics of each experiment rather different, in particular, systematics resulting from the methods used to assay the ^{71}Ge in the ^{71}Ga. The SAGE experiment [13] uses 50 tonnes of gallium metal as the target, while the GALLEX [14] and GNO [15] experiments use 30.3 tonnes of natural gallium in hydrochloric solution as the target.

The overall result from SAGE, from 70 runs taken from January 1990 to October 1999 [13][16], is:

$$75.4^{+7.0}_{-6.8}(stat.)^{+3.5}_{-3.0}(sys.)\ \mathrm{SNU}$$

The overall result from GALLEX, from 65 runs taken from May 1991 to January 1997 [14], is:

$$77.5 \pm 6.2(stat.)^{+4.3}_{-4.7}(sys.)\ \mathrm{SNU}$$

The overall result from GNO, from 19 runs taken from May 1998 to January 2000 [15] [17], is:

$$65.8^{+10.2}_{-9.6}(stat.)^{+3.4}_{-3.6}(sys.)\ \mathrm{SNU}$$

In contrast to these results, the BP2000 SSM prediction [9] (for all the above results) is:

$$128^{+9}_{-7} \text{ SNU}$$

1.3.2 Water Čerenkov Experiments

Water Čerenkov detectors detect neutrinos by neutrino-electron scattering:

$$\nu_x + e^- \quad \rightarrow \quad \nu_x + e^-$$

If the scattered electron is energetic enough, it will produce Čerenkov radiation. Čerenkov radiation is emitted when a charged particle travels through a medium faster than the speed at which light propagates through the medium. The number of Čerenkov photons emitted per unit track length per unit wavelength is given by [18] :

$$\frac{d^2N}{dx\,d\lambda} = \frac{2\pi\alpha Z^2}{\lambda^2}\left(1 - \frac{1}{n^2\beta^2}\right)$$

where α is the fine structure constant, n is the refractive index of the medium and Z is the charge of the relativistic particle. The light is emitted in a cone of half angle θ_C=$\cos^{-1}(1/n\beta)$. For an electron in water with 5-15 MeV of kinetic energy about 220 Čerenkov photons, between 250 and 600 nm, per MeV are emitted at a Čerenkov cone angle of 42°.

The Čerenkov light produced is detected by an array of photo-multiplier tubes (PMTs). These detectors therefore detect neutrinos in real time, making them sensitive to variations occurring over short time-scales such as day-night effects. The Čerenkov light also allows information about the energy and direction of the detected neutrino to be inferred[2].

[2]Because of the directional sensitivity, these experiments are credited with the first demonstration that the neutrinos detected were actually from the Sun.

The reaction is sensitive to all types of active neutrinos, although the sensitivity to electron neutrinos is enhanced by the charge current channel. The cross section for ν_μ or ν_τ scattering is only about one sixth of that for ν_e.

The reaction has no energy threshold[3], although the scattered electron must have at least $\sim$0.26 MeV to produce Čerenkov light in water. Unfortunately this does not represent a realistic threshold for analysis as signals within water Čerenkov detectors are overwhelmed at low energies by naturally occurring radioactivity. As a result, water Čerenkov detectors have a practical threshold of about 5 MeV. They are therefore only sensitive to ^{8}B and *hep* neutrinos.

Kamiokande

The Kamiokande experiment is located in the Kamioka mine, in the Japanese Alps about 200 km west of Tokyo, at a depth of 1000 metres. The original experiment was designed to search for proton decay, but was upgraded in 1985 to realise its potential as a solar neutrino detector (becoming Kamiokande II). The target is 3000 tonnes of H_2O contained in a cylindrical tank. The inner volume, some 2140 tonnes of water, is viewed by 948 20-inch PMTs and the outer volume, viewed by 123 PMTs, is used as a cosmic ray veto and a shield from backgrounds from the surrounding rock. The experiment was upgraded again in 1990 (becoming Kamiokande III). Dead PMTs were replaced, light reflectors and new electronics installed, and radon levels reduced. The combined ^{8}B flux measurement from Kamiokande II and III [19], made with an energy threshold of 7 MeV, is:

$$2.80 \pm 0.19(stat.) \pm 0.33(sys.) \times 10^6 \,\mathrm{cm}^{-2}\,\mathrm{s}^{-1}$$

The BP2000 SSM ^{8}B flux [9] is:

$$5.05 \times 10^6 \,(1.00^{+0.20}_{-0.16})\,\mathrm{cm}^{-2}\,\mathrm{s}^{-1}$$

[3] neglecting the small atomic binding energy of the electrons

Super-Kamiokande

Super-Kamiokande[4] is a much larger version of the Kamiokande detector. The target is 50000 tonnes of H_2O. Of this, 32000 tonnes constitutes the inner volume which is viewed by 11,146 20-inch PMTs. 1,885 8-inch PMTs view the outer volume. The measured ^{8}B flux [20] over the period from May 1996 to September 2000, made with an energy threshold of 5 MeV, is:

$$2.32 \pm 0.03(stat.)^{+0.08}_{-0.07}(sys.) \times 10^6 \,\mathrm{cm}^{-2}\,\mathrm{s}^{-1}$$

In addition to a flux measurement, Super-Kamiokande also measured the shape of the ^{8}B spectrum and the day-night flux ratio. No energy distortions in the ^{8}B neutrino spectrum were seen, with a fit to an undistorted spectrum giving a χ^2/d.o.f. of 19.0/18. The day-night flux asymmetry, defined as $\mathcal{A} = (\Phi_n - \Phi_d)/\frac{1}{2}(\Phi_n + \Phi_d)$, is:

$$\mathcal{A} = 0.033 \pm 0.022(stat.)^{+0.013}_{-0.012}(sys.)$$

These measurements are important when considering matter effects in neutrino oscillation solutions (see section 1.5.2).

The Sudbury Neutrino Observatory

The Sudbury Neutrino Observatory (SNO) is the latest water Čerenkov detector. It is unique among water Čerenkov detectors because it uses heavy water (D_2O) as its target material. This expensive alternative to light water (H_2O) provides additional neutrino detection capabilities which enable SNO to measure the total active neutrino flux and the electron neutrino flux separately. The Sudbury Neutrino Observatory is described in detail in chapter 2, as are its first results and their implications.

[4]This description is of the detector before the accident on 12th November, 2001.

1.4 The Solar Neutrino Problem

Every solar neutrino experiment to date has successfully measured a neutrino flux from the Sun. While this is a great achievement, none of the measurements agree with the predicted neutrino flux; they are all between 30 and 60% low. The results from the various experiments, along with the BP2000 SSM predictions are shown in figure 1.4. This disagreement has come to be known as the solar neutrino problem and has existed for more than 30 years without a definitive solution.

Possible Solutions

It was first thought that the problem was due to an error in either the SSM or the experiments. Indeed, with the prediction of the ^{8}B flux being very sensitive to the stellar core temperature, the disagreement with the Homestake result could conceivably be merely a slight error in the SSM. However, with the additional results of the other experiments this became less likely. The gallium experiments, in particular, were difficult to explain in this manner as the *pp* flux was thought to be known to within 1%. In addition, it became increasingly unlikely that experimental error was to blame as three completely independent techniques had been used. This eliminated the possibility that a common systematic error was responsible for the observed deficits.

Considering the measured fluxes in terms of the neutrino production processes they are sensitive to, gives another possible explanation. The Homestake result has a larger deficit than the water Čerenkov results, suggesting that the ^{7}Be line has been suppressed more than the ^{8}B neutrinos. The gallium results also give weight to this idea, as the neutrinos they detect could be interpreted as purely *pp* neutrinos. However, this leads to the conclusion of a non-existent ^{7}Be flux

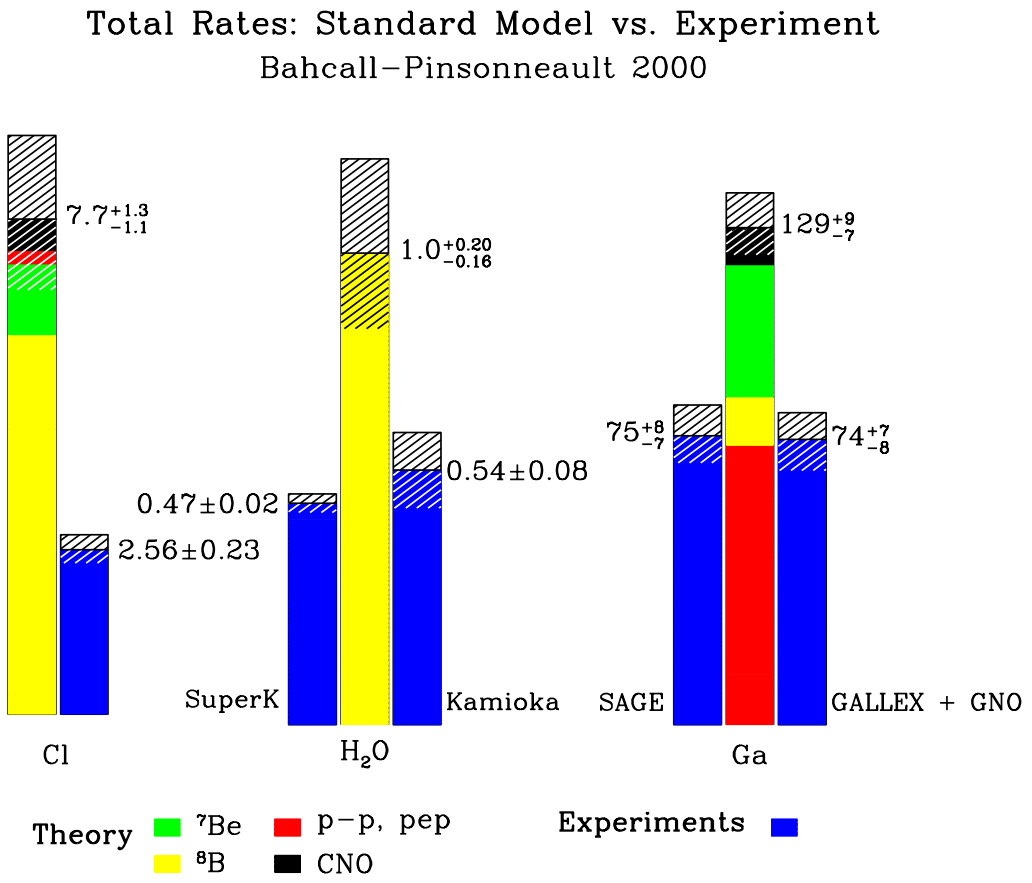

Figure 1.4: A comparison of the BP2000 standard solar model predictions (broken into neutrino production processes) and the actual experimental results. The cross hatching represents 1σ errors. The discrepancies between the predicted and observed neutrino fluxes embodies the solar neutrino problem: experimental observations are always lower than the SSM prediction. Taken from [11].

despite the presence of ^{8}B neutrinos. This is very difficult to reconcile as ^{7}Be is required to produce ^{8}B (see figure 1.1). In the context of an error in the SSM, this is very difficult to understand.

This is summarised in figure 1.5 which shows the results of a fit, described in [21], of the ^{7}Be and ^{8}B neutrino fluxes using the results from the Cl, Ga and Kamioka experiments. As can be seen, the best fit is a negative ^{7}Be flux. Excluding the results from any of the experimental techniques (water, Cl or Ga)

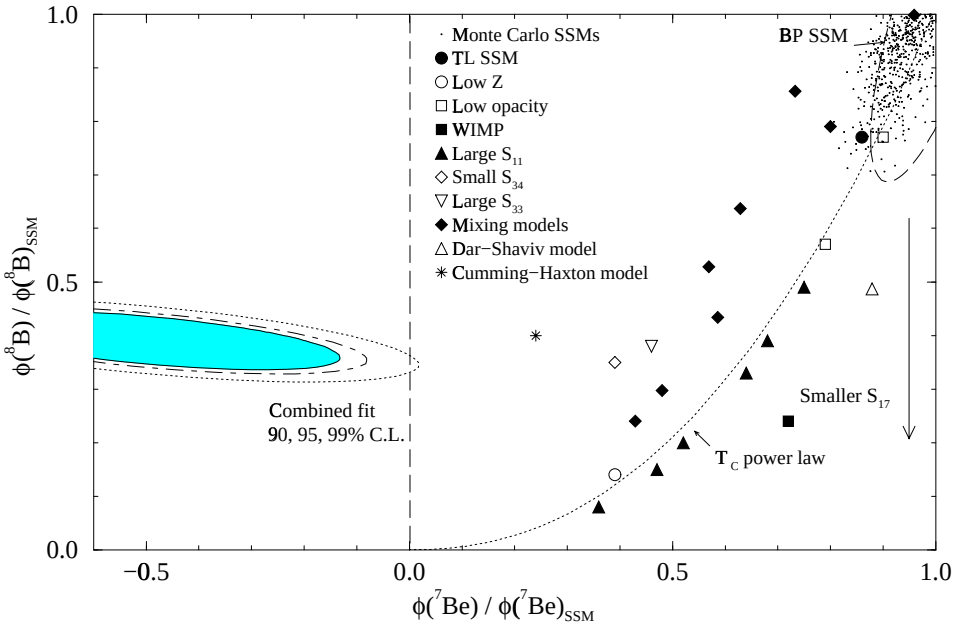

Figure 1.5: The results of a fit of the ^{7}Be and ^{8}B neutrino fluxes given the results from the Cl, Ga and Kamioka experiments. The best fit, which is largely unchanged if any one experimental result is excluded, is an unphysical ^{7}Be flux. Also shown is the BP1995 SSM 90% confidence region, the Bahcall-Ulrich Monte Carlo SSMs, and a variety of non-standard solar models. The S factors S_{11}, S_{33}, S_{34} and S_{17} are the energy independent component of the cross sections for the reactions p+p$\rightarrow^2$H+e^++ν_e, 2 ^{3}He$\rightarrow^4$He+2p, ^{3}He+^{4}He$\rightarrow^7$Be+γ and p+^{7}Be$\rightarrow^8$B+γ respectively. The T_C power law model parameterises the neutrino fluxes by power laws dependent on the core temperature (thus describing a large class of non-standard models). No solar model, standard or non-standard, has been found which can describe observed neutrino fluxes. Taken from [21].

still results in an unphysical fit. No solar model has been found which can explain the observed neutrino flux.

There remains one solution to the solar neutrino problem which can allow both the experiments and the SSM to be correct: the Sun is producing the predicted number of neutrinos, but something is happening to them on their way to the Earth. The most popular suggestion is flavour oscillations.

1.5 Oscillations of Massive Neutrinos

The concept of flavour oscillations is not a new one. In the quark sector, the eigenstates of the weak and strong interactions are known to be rotated with respect to each other. Although leptons do not feel the strong force, there is no reason for their mass eigenstates to be the same as their weak interaction eigenstates. Flavour changing oscillations can then occur if the different neutrino generations have different masses. With neutrino experiments being primarily sensitive to electron neutrinos, this could account for the observed deficit. This idea was first suggested by Pontecorvo and Gribov [22][23].

A brief outline of neutrino oscillations is given below, for a full discussion see Bahcall chapter 9 [8].

1.5.1 Vacuum Oscillations

For simplicity, consider vacuum oscillations between two neutrino flavours: ν_e and ν_x; where ν_x may be identified with ν_μ, ν_τ, a linear combination of ν_μ and ν_τ, or even with a fourth-generation neutrino (possibly sterile). The flavour eigenstates $|\nu_e\rangle$ and $|\nu_x\rangle$ are related to the mass eigenstates $|\nu_1\rangle$ and $|\nu_2\rangle$ by the unitary transformation:

$$\begin{pmatrix} |\nu_e\rangle \\ |\nu_x\rangle \end{pmatrix} = \begin{pmatrix} \cos\theta_\nu & \sin\theta_\nu \\ -\sin\theta_\nu & \cos\theta_\nu \end{pmatrix} \begin{pmatrix} |\nu_1\rangle \\ |\nu_2\rangle \end{pmatrix} \tag{1.2}$$

where θ_ν is the vacuum mixing angle. The three flavour version of the above matrix is known as the MNS matrix [24], and is analogous to the CKM matrix which specifies mixing in the quark sector.

The mass eigenstates evolve in time in the usual way, thus the time evolution of an electron-neutrino state, created at $t = 0$, is given by:

$$|\nu_e\rangle_t = \cos\theta_\nu \exp(-iE_1 t/\hbar)|\nu_1\rangle + \sin\theta_\nu \exp(-iE_2 t/\hbar)|\nu_2\rangle \tag{1.3}$$

where E_1 and E_2 are the energies of the two mass eigenstates with the same momentum. The probability amplitude for the detection[5] of an electron neutrino remaining after a time t is then:

$$\langle \nu_e | \nu_e \rangle_t = \cos^2\theta_\nu \exp(-iE_1 t/\hbar) + \sin^2\theta_\nu \exp(-iE_2 t/\hbar) \tag{1.4}$$

which corresponds to a probability of:

$$\mathcal{P}(\nu_e \to \nu_e) = |\langle \nu_e | \nu_e \rangle_t|^2 = 1 - \sin^2 2\theta_\nu \sin^2[(E_2 - E_1)t/2\hbar] \tag{1.5}$$

Assuming that the two mass eigenstates have the same momentum and therefore different energies (a more general discussion, with the proper wave-packet treatment, can be found in [25]), equation 1.5 can be re-written in terms of the mass difference of the mass eigenstates. Using $E \approx p + m^2/2p$ gives:

$$\mathcal{P}(\nu_e \to \nu_e) = 1 - \sin^2 2\theta_\nu \sin^2\left(\frac{1.27\Delta m^2 L}{E}\right) \tag{1.6}$$

where $\Delta m^2 \equiv |m_2^2 - m_1^2|$ in eV^2, L is the distance between creation and detection in metres, and E is the energy of the neutrino in MeV. Alternatively, equation 1.5 can be re-written in terms of the vacuum oscillation length, L_ν :

$$\mathcal{P}(\nu_e \to \nu_e) = 1 - \sin^2 2\theta_\nu \sin^2\left(\frac{\pi L}{L_\nu}\right) \tag{1.7}$$

where

$$L_\nu = \frac{4\pi E\hbar}{\Delta m^2 c^3} = \frac{2.48E\,(\mathrm{MeV})}{\Delta m^2\,(\mathrm{eV}^2)}\ \text{metres} \tag{1.8}$$

As can be seen from equation 1.5 the detection probability can be less than unity after some distance. For a given θ_ν, the maximum sensitivity to vacuum oscillations occurs when $\Delta m^2 \sim E/L$. With the very long baseline available to solar neutrino experiments, very small values of Δm^2 can be probed; far smaller than can be achieved with terrestrial neutrino sources.

[5] using a charge current channel

1.5.2 Matter Enhanced Oscillations

The effect of matter on neutrino oscillations was first studied by Wolfenstein [26]. Later, Mikheyev and Smirnov extended this work to the propagation of neutrinos within the Sun [27][28]. The dramatic enhancement in neutrino oscillations that can be caused by matter in the Sun is called the MSW effect.

The basis of the MSW effect is that electron neutrinos can scatter via a charged-current neutrino-electron process in matter. This interaction, which is absent for the other neutrino flavours, introduces an additional mass term in the mass matrix. The contribution to the mass matrix is:

$$M_{matter} = \sqrt{2} G_F n_e P_e \tag{1.9}$$

where n_e is the electron number density and P_e is the projection operator for electron neutrinos. The solution for the case of a constant electron density has the same form as the vacuum solution:

$$\mathcal{P}(\nu_e \to \nu_e) = 1 - \sin^2 2\theta_{\mathcal{M}} \sin^2 \left(\frac{\pi L}{L_{\mathcal{M}}} \right) \tag{1.10}$$

where the mixing angle in matter, $\theta_{\mathcal{M}}$, is:

$$\tan 2\theta_{\mathcal{M}} = \frac{\tan 2\theta_{\mathcal{V}}}{[1 \pm (L_{\mathcal{V}}/L_e) \sec 2\theta_{\mathcal{V}}]} \tag{1.11}$$

where the plus sign applies if $m_2 < m_1$ and the minus sign otherwise. The matter oscillation length, $L_{\mathcal{M}}$, is:

$$L_{\mathcal{M}} = L_{\mathcal{V}} / \left[1 - 2 \left(\frac{L_{\mathcal{V}}}{L_e} \right) \cos 2\theta_{\mathcal{V}} + \left(\frac{L_{\mathcal{V}}}{L_e} \right)^2 \right]^{1/2} \tag{1.12}$$

and the neutrino-electron interaction length, L_e, is:

$$L_e = \frac{\sqrt{2} \pi \hbar c}{G_F n_e} \tag{1.13}$$

From equation 1.11 it can be seen that, providing $m_2 \geq m_1$, maximal mixing ($\theta_{\mathcal{M}} = \pi/4$) is possible when $L_{\mathcal{V}}/L_e = \cos 2\theta_{\mathcal{V}}$. This condition is referred to as the 'resonance condition' and occurs when:

$$n_e = \frac{\Delta m^2 \cos 2\theta_{\mathcal{V}}\, c^4}{2\sqrt{2} G_F E} \tag{1.14}$$

An electron neutrino will always pass through a region where this resonance condition is satisfied if its energy exceeds the resonance value for an electron density corresponding to the solar centre.

The effect of the resonance condition can be increased in the Sun because of the electron density radial profile. If, after passing through resonance, the electron density is slowly varying (the adiabatic condition) then no further transitions occur between the mass eigenstates. Because the value of the electron density at resonance is energy dependent, the resonance effect can be strongly energy dependent. In this way, it may be possible to pick between different solutions.

Figure 1.6 shows the energy dependence of various solutions, including solutions in which matter effects are unimportant. The matter solutions are usually referred to as the large mixing angle (LMA), small mixing angle (SMA) and low Δm^2 (LOW) solutions. Of the solutions in which matter effects are unimportant (vacuum solutions (VAC)), the Just So^2 solution refers to the precise tuning of the parameters to give the observed experimental results assuming a single neutrino oscillation.

One last feature of matter enhanced oscillations is that the Earth can also cause observable effects. Such effects would appear as a day-night asymmetry and would also help to constrain the allowed parameter space.

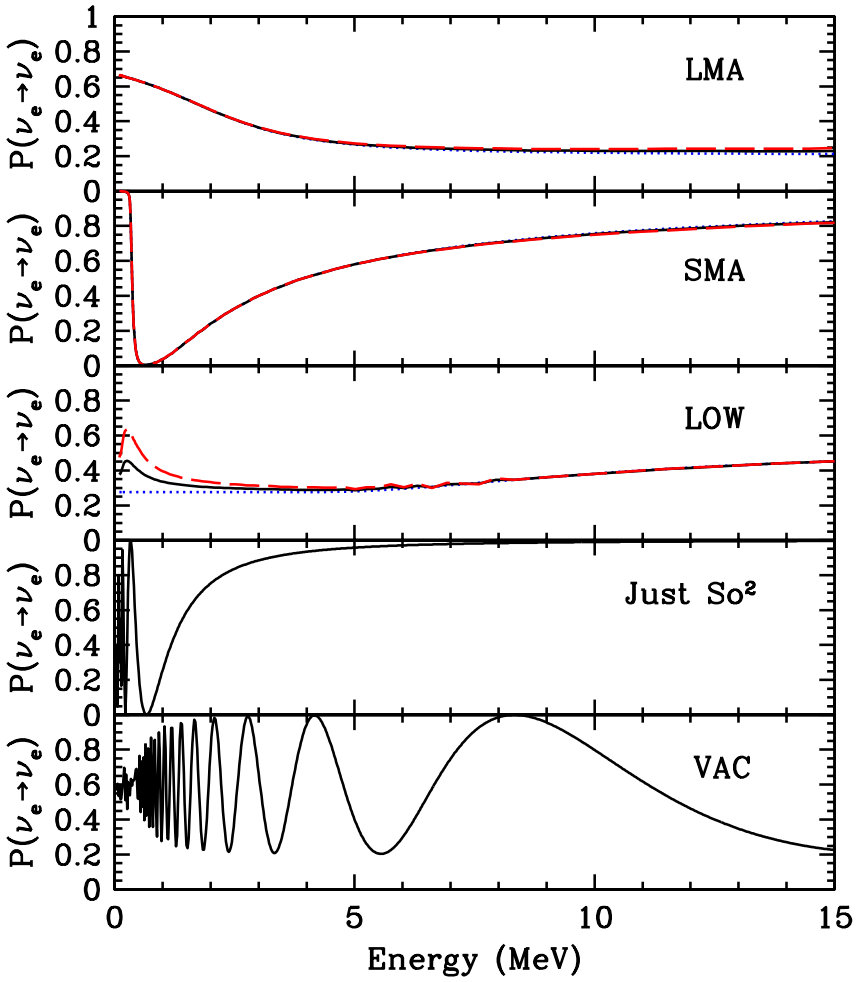

Figure 1.6: The survival probability as a function of energy for typical solutions in MSW space. The solid line is the yearly average, whereas the dotted and dashed line correspond to data taken only in the day or night respectively. Taken from [29]. The parameters used are:

	Δm^2	$\tan^2\theta$
LMA	4.2×10^{-5}	2.6×10^{-1}
SMA	5.2×10^{-6}	5.5×10^{-4}
LOW	7.6×10^{-8}	7.2×10^{-1}
Just So^2	5.5×10^{-12}	1.0×10^{0}
VAC	1.4×10^{-10}	3.8×10^{-1}

1.5.3 Allowed Oscillation Solutions

A global analysis can be performed to find the allowed values of $\tan^2\theta_\nu$ and Δm^2 given the experimental rates. Figure 1.7 shows the result of such an analysis for active neutrinos [30]. This analysis uses the predictions from the BP2000 SSM and the results from the chlorine, gallium, Super-Kamiokande (including day-night spectral shape) and the CHOOZ [31] experiments. The SMA and Just So^2 solutions are disfavoured with this data. The recent SNO results have not been included and will be discussed in chapter 2.

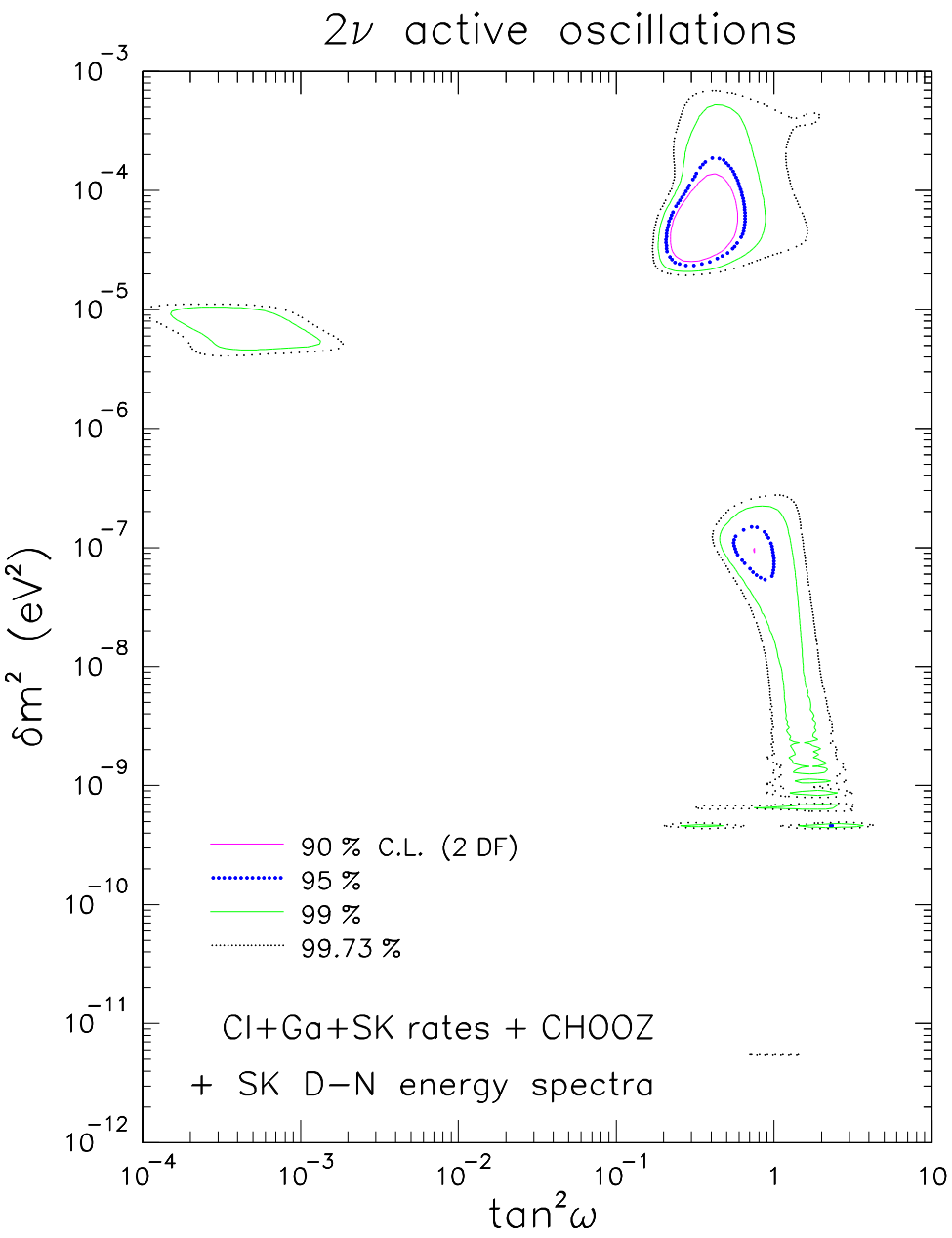

Figure 1.7: The results from a two flavour active neutrino global analysis using results from the Cl, Ga, Super-Kamiokande and CHOOZ experiments and predictions from the BP2000 SSM. The SMA solution appears in the upper left of the figure, the LMA in the upper right, the LOW in the middle right, the VAC solution below the LOW solution and the Just So^2 in the bottom right. Confidence limits on the allowed parameters are shown and should be interpreted as the probability that the correct solution lies within the given contour. Taken from [30].

Chapter 2

The Sudbury Neutrino Observatory

The Sudbury Neutrino Observatory (SNO) was proposed by H. Chen in 1985 [32]. It is the most recently constructed water Čerenkov solar neutrino detector. The detector is located near Sudbury, Canada, in an active nickel mine operated by Inco Limited. SNO is the deepest neutrino experiment to date, some 2040 metres underground (equivalent to 6000 metres of water). Utilising a D_2O target, it is the first experiment to have equal sensitivity to all flavours of active neutrinos (in the neutral current channel, see section 2.2) and arguably represents the best chance to solve the solar neutrino problem.

2.1 The SNO Detector

A diagram of the SNO detector is shown in figure 2.1. The detector is situated in a large barrel shaped cavity 22 m in diameter and 34 m in height. The 1 kilotonne ultra-pure D_2O target is contained within a transparent acrylic vessel (AV) 12 m in diameter and 5.5 cm thick. A 17.8 m diameter geodesic sphere[1] surrounds the AV and supports 9456 inward looking and 91 outward looking 20 cm PMTs. The

[1]Known as the PSUP - the Pmt SUPport structure

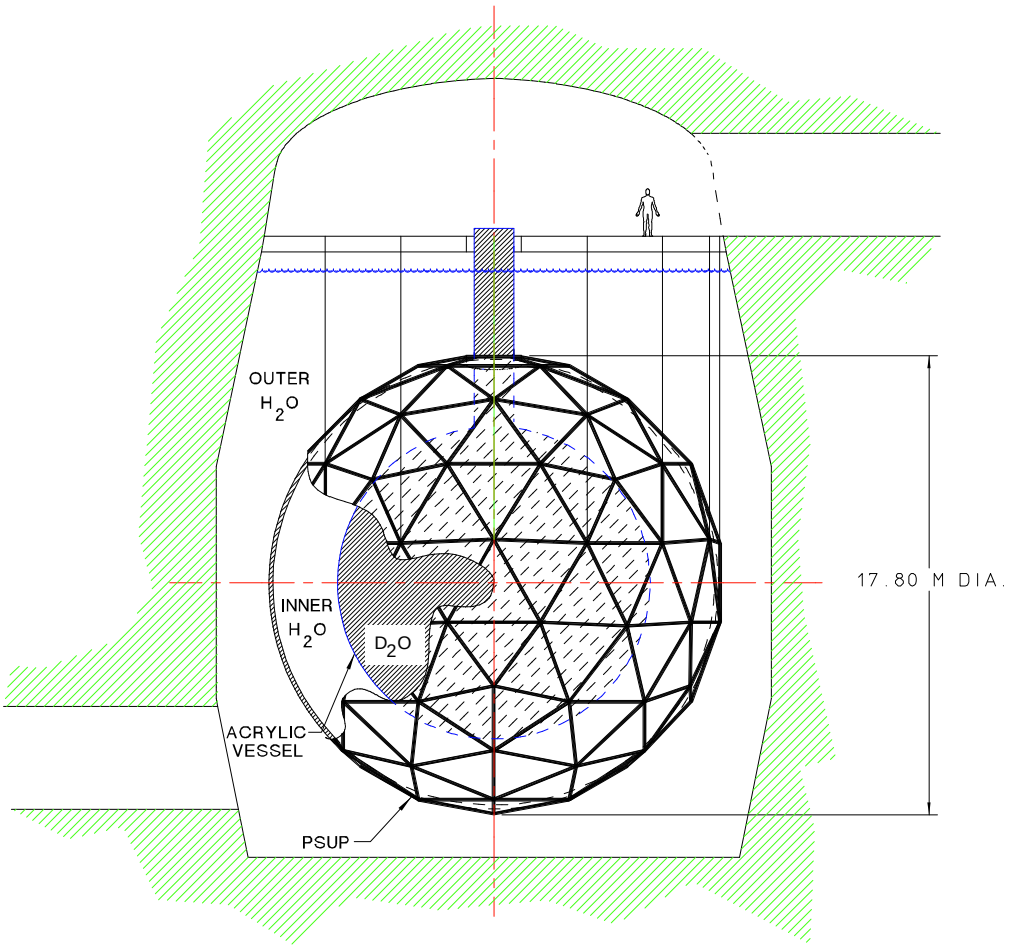

Figure 2.1: The SNO detector. Taken from [33].

PSUP is supported by steel ropes attached to the deck. The remaining volume is filled with ultra-pure H_2O which acts as a cosmic ray veto and as a shield from naturally occurring radioactivity in both the construction materials and the surrounding rock. The light water also supports the D_2O and AV with the remaining weight supported by 10 Vectran rope loops.

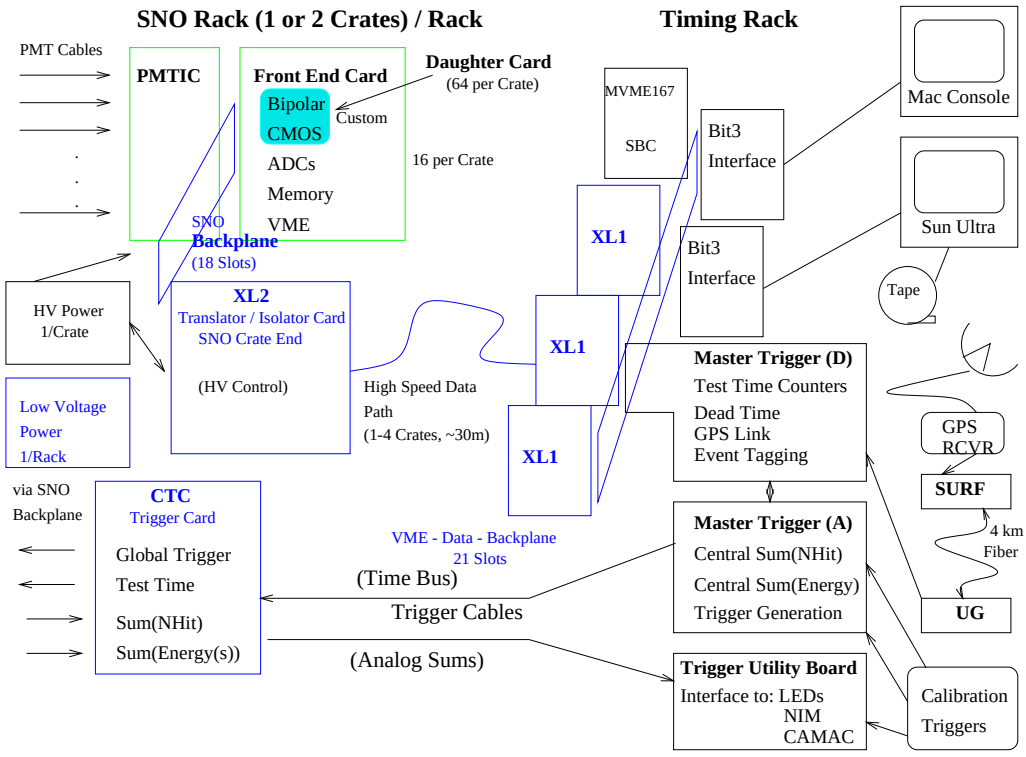

Figure 2.2: The SNO electronics and data acquisition hardware. The front-end system responsible for PMT signal processing is shown in the upper left part of the figure, with the components of the central trigger system and DAQ shown on the right. Taken from [36].

2.1.1 The SNO Electronics

The electronics for the SNO experiment [34][35] are housed in the deck area directly above the detector. They are responsible for measuring the hit time and charge information from the PMT pulses, and to generate a trigger if the event satisfies triggering requirements. A schematic overview of the SNO electronics is shown in figure 2.2.

The Front End Electronics

The SNO electronics occupies 19 crates on the deck. Each crate contains 16 cards, with each card capable of handling signals from 32 PMTs. Cards are composed of

a PMT interface card (PMTIC) and a front-end card (FEC). Every PMTIC has four paddle cards, to which the cables from the PMTs are connected in groups of eight. The PMTIC supplies the high voltage to the PMTs and, as single cables are used for carrying high voltage and PMT signals, passes the decoupled signals to the FEC for processing. Mounted on each FEC are four daughter boards (DBs). These mirror the paddle cards on the PMTIC and perform the signal processing.

A signal received by a DB is delivered to a four-channel discriminator chip (SNOD). This chip triggers if the signal crosses a preset threshold. The PMT current is also split (approximately in the ratio 1:16 to provide high and low gain measurements) and fed into two channels of an eight-channel charge integrator (SNOINT). If the SNOD chip triggers, signals are sent to the SNOINT chip to provide the timing functions necessary for both the long ($\sim$400 ns) and short ($\approx$70 ns) charge integrations.

A signal is also sent by the SNOD chip to the CMOS member of the SNO chip set (QUSN7) to initiate the time-to-amplitude converter (TAC) (of which QUSN7 has two, used alternatively to reduced dead-time) and the other timing sequences (used to create trigger primitives). QUSN7 provides the analogue memory in which the outputs from the SNOINT chip (QHS, QHL, QLX[2]) and the TAC value are held if a global trigger (GT) arrives. Each QUSN7 chip has 16 analogue memory banks for this purpose, which are referred to as cells. A field-programmable gate array (FPGA) then controls the digitisation of these signals and storage in the onboard DRAM before they are passed to the DAQ.

[2]The charge measurements: high gain short (QHS) and long (QHL) time integration and low gain with selectable time integration (QLX); usually low gain with long time integration (QLL) is used.

The SNO Trigger System

The SNO trigger system [37] is responsible for determining whether a potentially interesting event has occurred within the detector based on information from the PMTs. If this is the case, the information from the PMTs must be stored and subsequently read out. The trigger system in SNO principally uses two types of triggers. The first type is based on the number of PMTs that fire (NHITS), and the second on the total amount of light produced in the detector (ESUM).

The NHITS trigger inputs are generated by the QUSN7 chip. The QUSN7 chip generates two trigger primitive signals, a short coincidence (20 ns) and a long coincidence (100 ns). These signals contribute to two analogue sums. If either of these sums exceeds the corresponding programmable threshold, a GT is generated. The 100 ns trigger serves as the primary physics trigger. It has three separate thresholds, the lowest of which can be prescaled to provide a monitor of very low energy backgrounds.

The ESUM trigger inputs are generated by the SNOINT chip. The SNOINT chip provides high and low gain analogue sums of the PMT signals for inclusion into two detector wide analogue sums. Like the NHITS sums, if these exceed a programmable threshold a GT is generated. These triggers are used primarily to provide continual diagnostic information about the detector.

In addition to these triggers, several others exist. There are equivalent NHITS and ESUM triggers for the outward looking tubes. The detector is triggered at a rate of 5 Hz with a pulser, the 'pulse-GT' trigger, which is used to determine the PMT noise rate. A pedestal trigger, or forced readout, is used to perform electronics calibration (see chapter 3 for more details) and some calibration sources also provide their own triggers.

Two separate clocks are used to timestamp triggers: a GPS synchronised

10 MHz clock, used for absolute time, and a highly stable 50 MHz quartz oscillator, for inter-event timing. This information, in addition to the trigger that created the GT, any other triggers that are satisfied in a ± 10 ns window and a unique trigger number (GTID) is written out with the other event information. This information is assembled into a complete event by the DAQ.

For the SNO experiment the primary physics trigger (the 100 ns NHITS trigger) has a typical threshold of 18 NHITS. As analysis thresholds are typically much higher than this (usually above 30 NHITS), the trigger can be considered to be 100% efficient and trigger inefficiencies need not be considered.

Data Acquisition (DAQ)

The SNO detector is both controlled and monitored via a user interface program called SHARC (SNO Hardware Acquisition and Readout Control). Event building is performed by a Sun Ultra-1 workstation running the 'event builder' program. During periods of sustained high rate in the detector the builder can be overwhelmed and fail to build full events. Information not assigned to a specific event is written out as an orphan event. This is potentially very dangerous as the resulting partial events are indistinguishable from full events. Fortunately, this is a rare occurrence under normal operating conditions and is estimated to contribute to a NHITS error of $<0.1\%$ [38].

2.1.2 The Water Systems

The SNO detector cannot tolerate normal levels of uranium and thorium as these elements can create an irreducible background to the neutral current signal. This will be discussed in more detail later. To minimise the potential background, the detector was constructed with materials which had very low levels of thorium and uranium. The cleanliness of both the D_2O and H_2O is of paramount importance

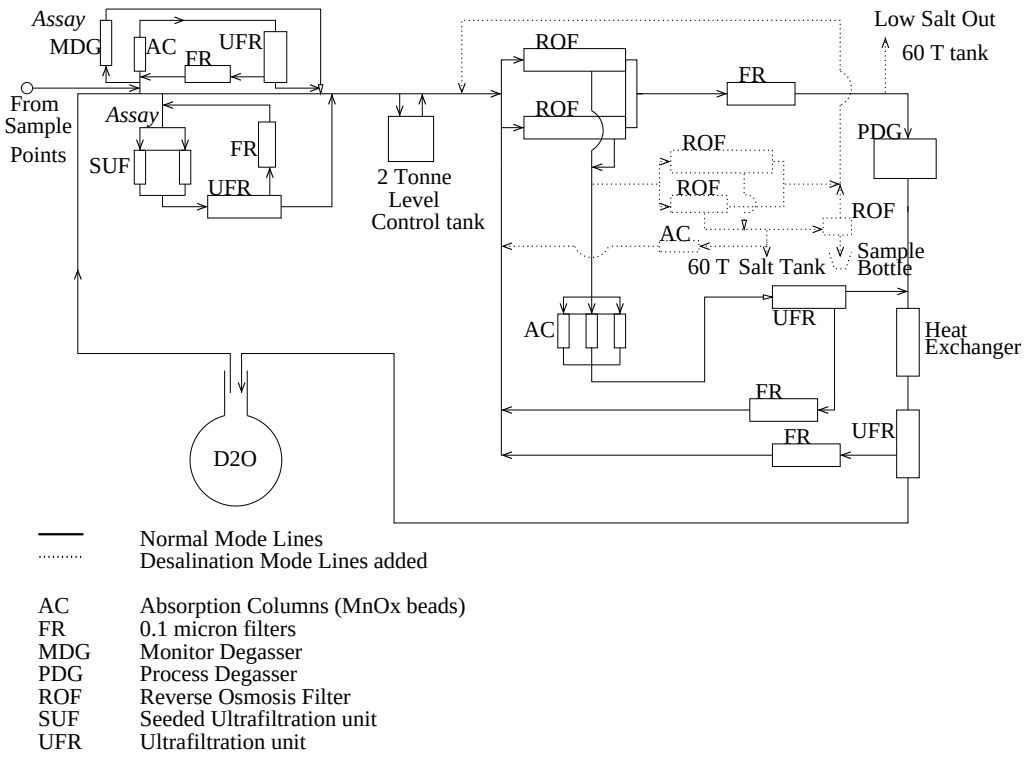

Figure 2.3: The SNO heavy water systems. Taken from [33].

and ensuring that thorium and uranium levels are not too high is the responsibility of the water systems [39].

Heavy Water Systems

The heavy water systems, shown schematically in figure 2.3, are responsible for purifying and assaying the D_2O. They must do this without significant loses of D_2O or degradation of its isotopic purity. The heavy water systems must also facilitate the addition and removal of NaCl, the presence of which must not compromise their operation.

The purification capability in the D_2O systems is given principally by ion-exchange columns and a large reverse osmosis (RO) system. A seeded ultra-filtration plant (SUF) [40] (for which the author was responsible for overhauling

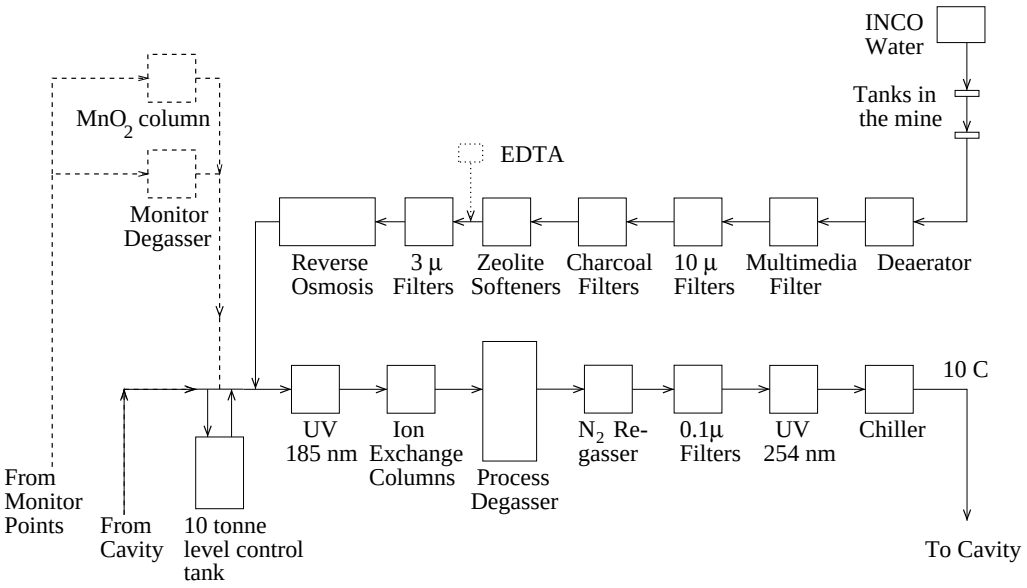

Figure 2.4: The SNO light water systems. Taken from [33].

and maintaining the $\beta\alpha$ coincidence counters used to determine the activity assayed) and MnO_x beads [41] provide assay capabilities (for Th and Ra), although these systems can also be used for purification. Indeed, after NaCl was added to the D_2O both these systems were used to purify and assay the D_2O as the RO would remove the salt. The D_2O is also degassed with a Liqui-Cell to remove radon; the extracted radon is counted to determine the radon levels in the D_2O.

Light Water Systems

The light water systems are shown schematically in figure 2.4. The light water used in SNO is from a surface purification plant that serves the mine. After being piped underground, the incoming water is supersaturated with air and so is first de-aerated. It is then passed through a series of filters to remove particulate matter before entering the H_2O RO to achieve ultra-high purity. After the RO the water is exposed to mercury UV lamps to break any remaining organic compounds into ionic form and then passed through an ion-exchange.

The water is then degassed to remove Rn and O_2. Initially, the water was introduced to the detector cavity at this point but this led to problems with breakdown in the PMT connectors [42]. The water is therefore regassed to atmospheric pressure (at a depth of 2000 m) with pure N_2 before being cooled to 10°C and put into the detector.

The water is continually recirculated to maintain purity levels (using a partial loop composed of the systems after the RO). This water is also assayed to determine the water's properties, including levels of radioactivity.

The Cover Gas System

The air in the mine is radon rich and therefore must not be allowed to enter either the D_2O or H_2O water volumes. To achieve this a nitrogen cover gas system is used. Nitrogen gas, boiled off from a liquid nitrogen dewar, provides a physical barrier between the water volumes and the laboratory air. Independent systems are used for the D_2O and H_2O volumes.

2.2 Neutrino Interactions in SNO

2.2.1 The Charged Current Interaction

The SNO experiment's primary method of detecting electron neutrinos is by the charged current (CC) interaction:

$$\nu_e + \mathrm{d} \;\rightarrow\; \mathrm{p} + \mathrm{p} + e^-$$

where the d is a deuteron atom. This interaction occurs via the W^+ boson and has a threshold of 1.44 MeV. Since the protons emerge almost stationary from the interaction, the energy of the emitted electron is essentially 1.44 MeV less than the energy of the neutrino. The electron is detected by observing the Čerenkov light produced, and this can also be used to infer the neutrino energy.

The charged current interaction has an electron angular distribution, relative to the neutrino direction (denoted by $\cos\theta_\odot$, the cosine of the angle to the direction of the Sun), given by [43]:

$$I(\theta_\odot) = 1 - 0.340\cos\theta_\odot \approx 1 - \frac{1}{3}\left(\frac{v}{c}\right)\cos\theta_\odot$$

2.2.2 The Neutral Current Interaction

The SNO experiment is equally sensitive to all active (non-sterile) neutrino flavours because of the neutral current (NC) interaction:

$$\nu_x + \mathrm{d} \quad \rightarrow \quad \nu_x + \mathrm{p} + \mathrm{n}$$

This interaction has a threshold of 2.2 MeV and it is the neutron which is detected. Detection of the neutron is particular to the phase of the SNO experiment, and this is discussed in more detail in section 2.3.

All active neutrino flavours can disintegrate a deuteron atom and thus this interaction will allow the measurement of the total neutrino flux from the Sun. As it is the neutron which is detected, no spectral (other than the threshold) or directional (because of neutron thermalisation) information is obtained.

2.2.3 The Elastic Scattering Interaction

The standard reaction utilised by light water Čerenkov detectors is also present in SNO:

$$\nu_x + e^- \quad \rightarrow \quad \nu_x + e^-$$

As mentioned before, the electron direction is sharply peaked away from the Sun. The cross-section for this interaction is [44]:

$$\frac{d\sigma}{dT} = \frac{2G_F^2 m_e}{\pi}\left[g_L^2 + g_R^2\left(1 - \frac{T}{E_\nu}\right)^2 - g_L g_R\left(\frac{m_e T}{E_\nu^2}\right)\right]$$

where E_ν is the initial neutrino energy, T is the electron recoil kinetic energy, g_L=$(\pm 1/2 + \sin^2\theta_W)$ and g_R=$\sin^2\theta_W$. The plus sign applies to ν_e scattering and the minus sign to ν_μ and ν_τ.

The cross-section for electron neutrinos is approximately a factor of 6.5 larger than that for the other neutrinos because the electron neutrinos can interact via $W^\pm$ exchange in addition to Z° exchange, which is available to all active neutrino flavours.

2.2.4 Anti-Neutrino Interactions

The SNO detector is also sensitive to electron anti-neutrinos via two further interactions based on the inverse β decay of the proton:

$$\begin{aligned} \bar{\nu}_e + \mathrm{d} &\rightarrow \mathrm{n} + \mathrm{n} + e^+ \\ \bar{\nu}_e + \mathrm{p} &\rightarrow \mathrm{n} + e^+ \end{aligned}$$

The first reaction will occur within the D_2O and the second within the H_2O. The signature of these reactions is Čerenkov light from the positron in delayed coincidence with the detection of the neutron capture. This will probably be impossible for the H_2O reaction as SNO's neutron detection capability is principally within the D_2O.

It is unlikely that these interactions will be relevant to the solar neutrino problem, but will be of interest if a galactic supernova occurs within the duration of the SNO experiment.

2.3 Phases of the SNO Experiment

The SNO experiment is planned to operate in several phases. In each phase, the characteristics of the NC response are changed. Each phase will be discussed

below. Currently (Jan 2002), the SNO experiment is in the second phase (D_2O with salt) of data taking.

Pure D_2O

The first phase of the SNO experiment is to operate with pure D_2O. In this configuration, neutrons produced by the NC interaction are detected when they capture on a deuteron atom:

$$n + d \rightarrow t + \gamma\,(6.25\,\mathrm{MeV})$$

As only ~30% of neutrons capture on deuteron atoms (the others either capturing on hydrogen or ^{17}O, or escape the D_2O) and the energy of the γ-ray is only 6.25 MeV, this configuration has a relatively low overall neutron detection efficiency. Additionally, there is no way to distinguish a single γ-ray from a single electron based on the PMT hit pattern they produce. The ability to identify neutral current events therefore relies on the differences in radial and energy distributions between charged current and neutral current events.

D_2O with NaCl

The second phase of the SNO experiment is to operate with ~2 tonnes of NaCl dissolved into the D_2O. Chlorine has a high thermal (n,γ) cross section (33.34 b) which causes the majority (>90%) of neutrons to capture on it. This produces an excited state of ^{36}Cl that decays to its ground state via a cascade of γ-rays:

$$n + {}^{35}Cl \rightarrow {}^{36}Cl + \gamma\,(8.6\,\mathrm{MeV\ total})$$

with an average of 2.6 γ-rays per cascade. In addition to a higher neutron capture efficiency, the higher total energy gives a higher detection efficiency over any given energy threshold. However, this is not the only reason for the addition of NaCl.

Because the excited state of ^{36}Cl decays via a γ-ray cascade, the resulting PMT hit pattern is more isotropic than that produced by a single γ-ray or electron. This allows neutral current events to be statistically separated from charged current events without relying on the radial or energy distributions.

^{3}He Proportional Counters

The ^{3}He proportional counters, or neutral current detectors (NCDs), will be deployed for the third phase of the SNO experiment. A total length of $\sim$770 m of counters will be suspended (actually anchored) in the D_2O and detect neutrons via the reaction:

$$n + {}^3He \rightarrow p + {}^3H \quad (Q = 0.764\,MeV)$$

The cross section for this interaction is 5327 b. The advantage of the NCDs is the ability to identify neutral current events on an event-by-event basis. Additionally, the neutral current Čerenkov signal is largely eliminated, potentially enabling an improved measurement of the charge current reaction energy spectrum (assuming the shadowing caused by the NCDs is well enough understood).

2.4 SNOMAN

SNOMAN is the SNO collaboration's Monte Carlo and ANalysis software package [45][46][47]. SNOMAN is primarily written in FORTRAN 77 with the ZEBRA [48] memory manager providing dynamic memory allocation.

SNOMAN provides a very comprehensive simulation of the detector and can model the propagation of all relevant particles (electrons, γ-rays, muons, neutrons, Čerenkov photons and hadrons) through the geometry and media of the detector, including the internal PMT geometry. The physical health (i.e. the number of PMTs working) of the detector at any given time can be included in

simulations, enabling SNOMAN to produce 'true to life' Monte Carlo data sets.

SNOMAN also provides a suite of analysis tools that can be applied to generated data as well as data from the detector. These tools include PMT calibration, event filters and reconstruction algorithms.

2.5 The First Results from SNO

The SNO collaboration announced its first results on 18th June, 2001 [49]. The results are based on data taken in pure D_2O between 2nd November, 1999 and 15th January, 2001 corresponding to a live time of 240.95 days.

Instrumental and other non-neutrino backgrounds (i.e. muons) are removed from the data set and the remaining events reconstructed. A fiducial volume cut of $R \leq 550\,\mathrm{cm}$ and an effective electron kinetic energy cut of $\mathrm{E} \geq 6.75\,\mathrm{MeV}$ are applied. The effective energy is based on the number of PMTs which fire, corrected for position, direction and detector conditions. The effective energy threshold allows low energy backgrounds from natural radioactivity in the D_2O to be ignored.

As was discussed in section 2.2, the interactions in SNO have different signatures in the detector. This is exploited by using PDFs (generated assuming no spectral distortions) in energy, radial position and direction with respect to the Sun to determine the relative contributions from each channel. An extended maximum likelihood technique is used to perform the fit, the results giving the following neutrino fluxes:

$$\begin{aligned} \Phi_{\mathrm{SNO}}^{\mathrm{CC}} &= 1.75 \pm 0.07(stat.)^{+0.12}_{-0.11}(sys.) \pm 0.05(theor.) \times 10^6\,\mathrm{cm}^{-2}\,\mathrm{s}^{-1} \\ \Phi_{\mathrm{SNO}}^{\mathrm{ES}} &= 2.39 \pm 0.34(stat.)^{+0.16}_{-0.14}(sys.) \times 10^6\,\mathrm{cm}^{-2}\,\mathrm{s}^{-1} \end{aligned}$$

where the theoretical uncertainty is the CC cross section uncertainty [50]. Repeat-

ing the signal extraction without using the energy PDF shows that the CC spectral shape is consistent with an undistorted ^{8}B spectral shape. SNO's ES measurement is consistent with the precision measurement from Super-Kamiokande:

$$\Phi_{\rm SK}^{\rm ES} = 2.32 \pm 0.03(stat.)^{+0.08}_{-0.07}(sys.) \times 10^6\,{\rm cm}^{-2}\,{\rm s}^{-1}$$

The SNO CC measurement is 3.3σ lower than the Super-Kamiokande ES measurement. Assuming the systematic errors are normally distributed, the probability that this is caused by a downward fluctuation is 0.04%. Remembering that SNO's CC measurement is only sensitive to electron neutrinos, whereas Super-Kamiokande's ES measurement has a weak sensitivity to all active flavours, this gives clear evidence of a non-electron neutrino component to the detected ^{8}B solar neutrino flux. Stated explicitly, the experimental sensitivities to neutrino flavours are:

$$\begin{aligned} \Phi_{\rm SNO}^{\rm CC} &= \Phi_e \\ \Phi_{\rm SK}^{\rm CC} &= \epsilon\Phi_{\mu\tau} \end{aligned}$$

where $\Phi_{\mu\tau}$ is the combined ν_μ and ν_τ flux and ϵ=1/6.481. These equations can be solved trivially for Φ_e and $\Phi_{\mu\tau}$. This is shown graphically in figure 2.5.

The preferred value of the total active neutrino ^{8}B flux is:

$$\Phi_{\rm SNO+SK}^{\rm TOT} = 5.44 \pm 0.99 \times 10^6{\rm cm}^{-2}\,{\rm s}^{-1}$$

which is in excellent agreement with the latest prediction:

$$\Phi_{\rm BP2001}^{\rm TOT} = 5.05^{+1.01}_{-0.81} \times 10^6{\rm cm}^{-2}\,{\rm s}^{-1}$$

The charged current result from SNO can be used to further constrain the allowed oscillation solutions to the solar neutrino problem. Figure 2.6 shows the results of a global analysis [30] using the results from all solar neutrino experiments including SNO. The result of this analysis without the SNO CC measurement was given in figure 1.7. As can be seen, the first results from SNO have

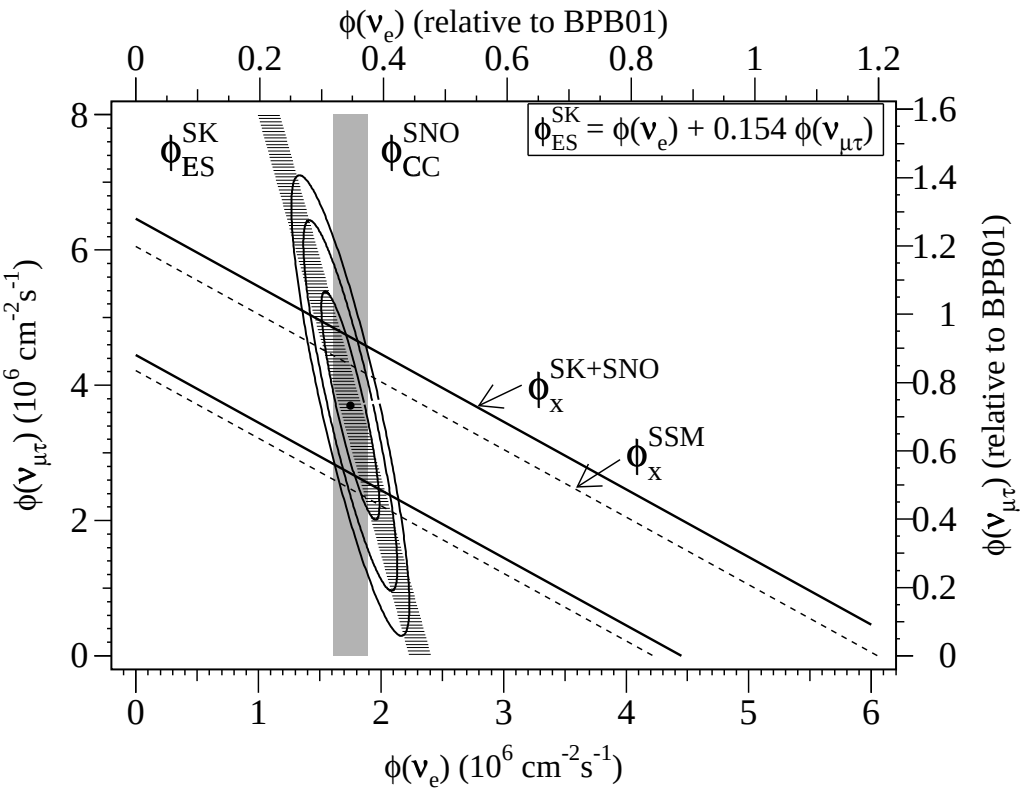

Figure 2.5: The CC result from SNO and the ES result from Super-Kamiokande expressed in terms of their ν_e and $\nu_{\mu\tau}$ components. Taken from [49].

further constrained the allowed solutions. The small mixing angle solution has been excluded at $>3\sigma$ and oscillations to purely sterile neutrinos (not shown) have been ruled out.

The remaining solutions favour near maximal mixing. With the future results from SNO, the remaining parameter space will be constrained further and hopefully reveal the exact nature of the solution to the solar neutrino problem.

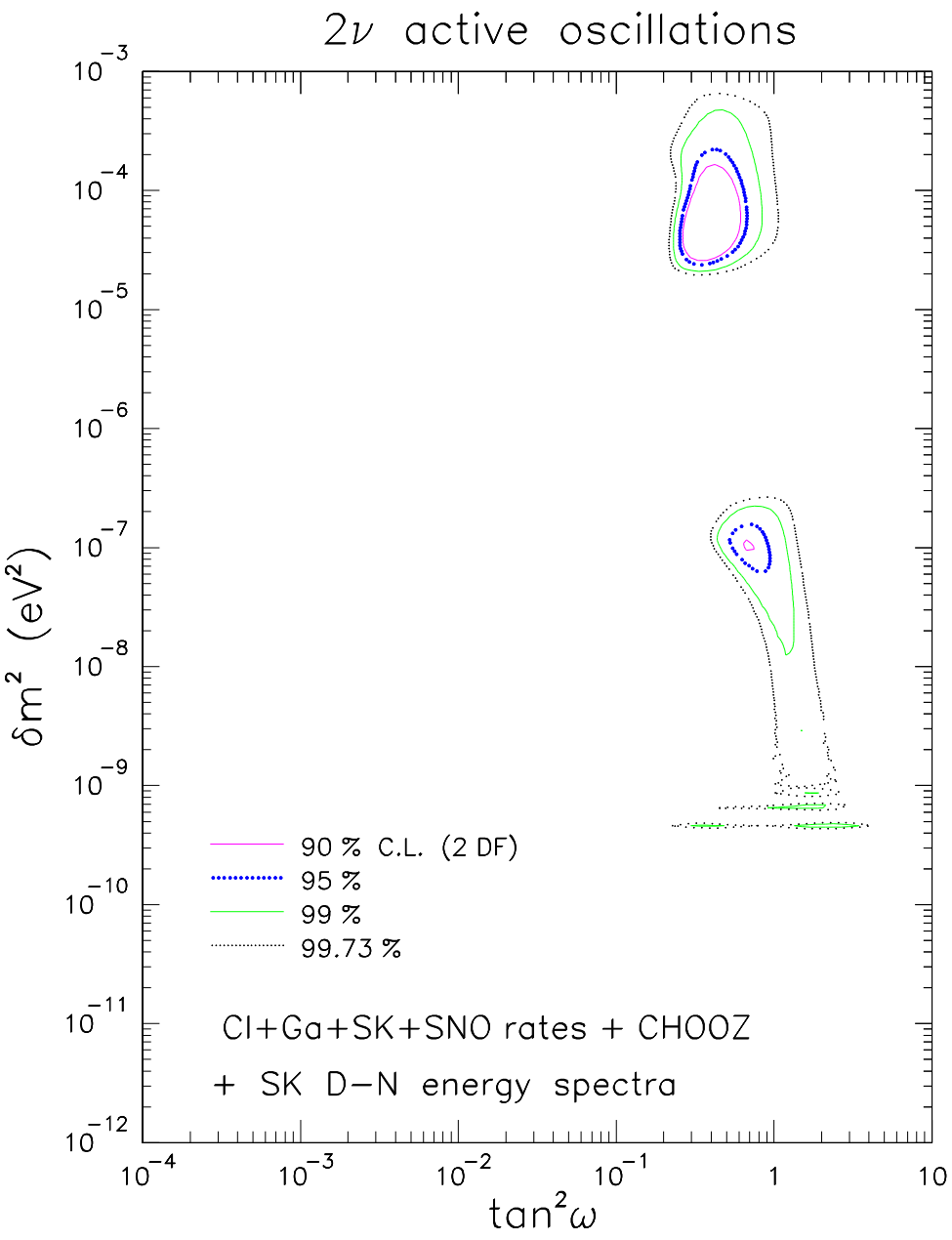

Figure 2.6: The results from a two flavour active neutrino global analysis using results from the Cl, Ga, Super-Kamiokande, CHOOZ and SNO experiments and predictions from the BP2000 SSM. The SMA solution is now excluded at $>3\sigma$. The LMA solution (top right) is now clearly favoured. Taken from [30].

Chapter 3

The History Calibrator (HCA)

This chapter discusses the history calibrator (HCA). This is a new timing calibration between the ECA and PCA which corrects a design oversight of the electronics which causes a channel's timing calibration to be dependent on the readout history of that channel, potentially invalidating the use of high rate calibration data.

The chapter begins with a brief overview of timing calibration in SNO. Next, the calibration problem is presented and characterised. The HCA is then introduced and its implementation and performance presented.

3.1 PMT Timing Calibration in SNO

PMT timing calibration in the SNO experiment is done in two steps: the electronics calibration (ECA) [51] and the photo-multiplier calibration (PCA) [52]. Each will be discussed briefly below.

3.1.1 Electronics Calibration (ECA)

For the timing measurement, the ECA is responsible for calibrating the TAC output of the QUSN7 chip (after it has been passed to an ADC). As was mentioned in section 2.1.1, the QUSN7 has two TACs to reduce dead-time and 16

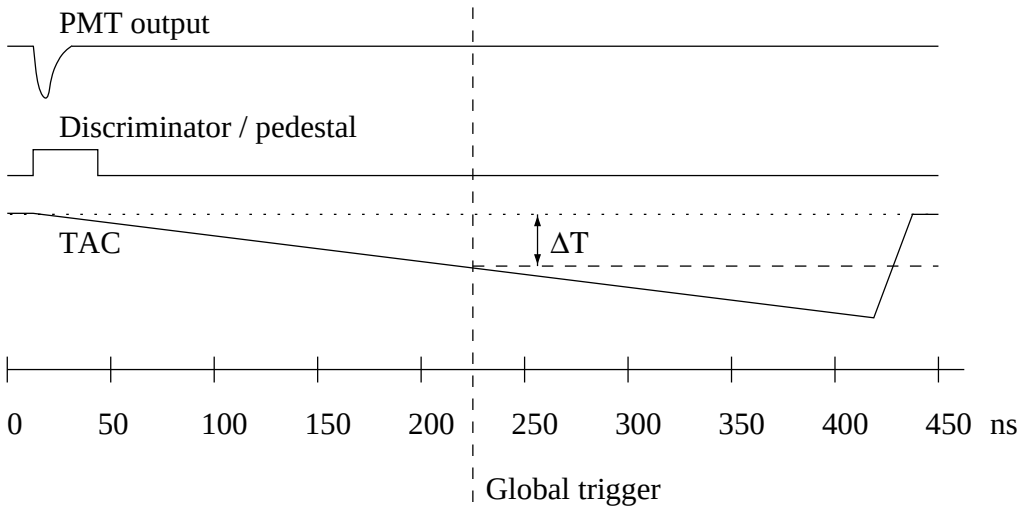

Figure 3.1: A schematic of the timing cycle for a single channel. The TAC begins to ramp when the discriminator is fired by a signal from the PMT or a pedestal pulse is received. On the arrival of a global trigger, the value of the TAC is stored. If no global trigger arrives after ~420 ns the channel is reset. (The PMT and discriminator/pedestal pulses are not drawn to scale).

analogue memory banks (cells) where signals are held if a global trigger arrives. Each of these cells must be individually calibrated. The ECA returns the time, in nanoseconds, between the discriminator firing (from SNOD) and the global trigger arriving, as shown in figure 3.1. Once the ECA has been applied, cell level dependence is removed.

ECA calibration data is obtained for a channel by artificially firing it using a 'pedestal' pulse. This causes the channel to behave as though its discriminator had fired. At some later time a global trigger is sent and the data is read out. The time between the pedestal pulse and the global trigger (PED-GT delay) can be varied, providing a mapping between ADC counts and the time the TAC has spent ramping.

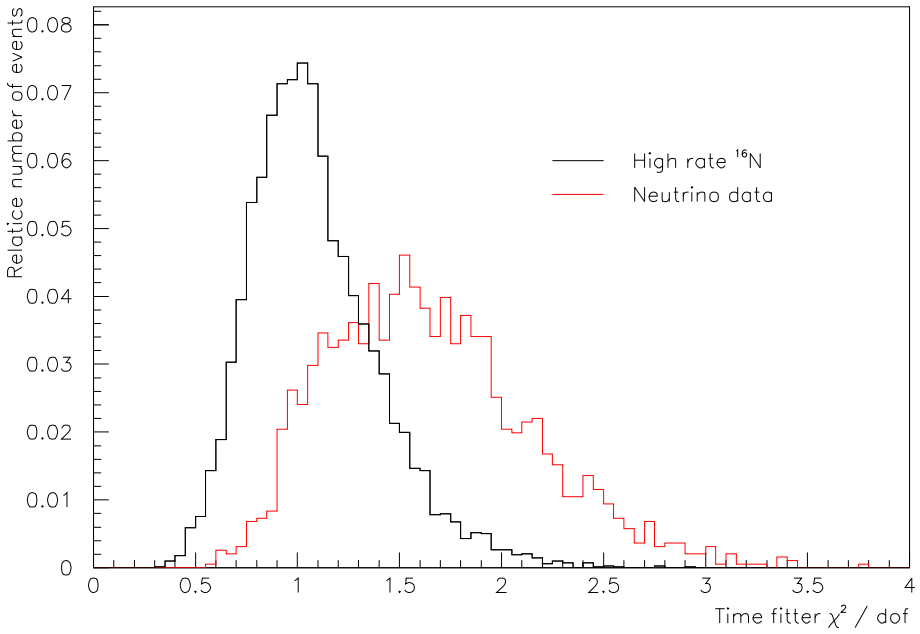

Figure 3.2: The time fitter χ^2 distributions for high rate ^{16}N data and neutrino data.

3.1.2 Photo-multiplier Calibration (PCA)

The PCA timing calibration is responsible for correcting the time measurement for physical cable delays and discriminator firing as a function of the signal height. After applying these corrections the PMT timing resolution is ~1.5 ns, approximately equal to the jitter time intrinsic to the PMT design.

3.2 The High χ^2 Anomaly

Several fitters are available for event reconstruction. The time fitter [45] is the simplest and fastest of the fitters and is used as a first pass fitter for rapid preliminary analysis. The method employed is a χ^2 minimisation of equation 3.1, where the sum is over N'_{pmt}, the number of in-time PMT hits (as determined by

recursive fit attempts of the fitter).

$$\chi^2(\vec{r_{fit}}, t_{fit}) = \sum_{i=1}^{N'_{pmt}} \left[\frac{t_i - t(\vec{r_i}, \vec{r_{fit}}, t_{fit})}{\sigma_{pmt}} \right]^2 \tag{3.1}$$

The χ^2 gives a good indication of the quality of the fit achieved and is extremely sensitive to the timing calibration of the hit PMTs. During early analysis of neutrino data, it was noticed that the χ^2 for neutrino data was significantly higher than the χ^2 for ^{16}N calibration data, as shown in figure 3.2.

This implied a problem with the PMT timing calibration that was present in the neutrino data but not in the ^{16}N calibration data. Such a scenario cast doubt on the validity of using the calibration source data to estimate the reconstruction performance of the fitters on neutrino data.

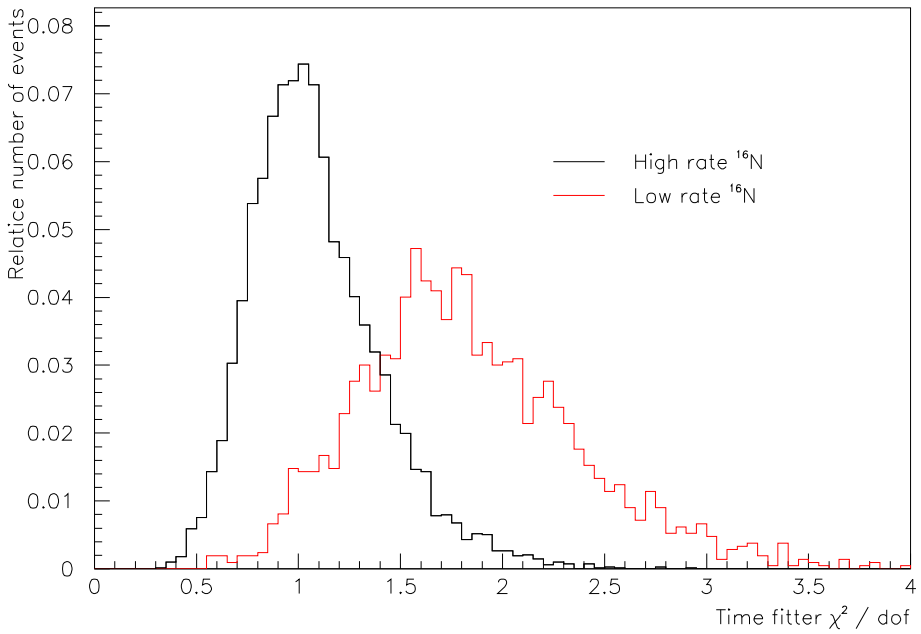

Figure 3.3: The time fitter χ^2 distributions for high and low rate ^{16}N data.

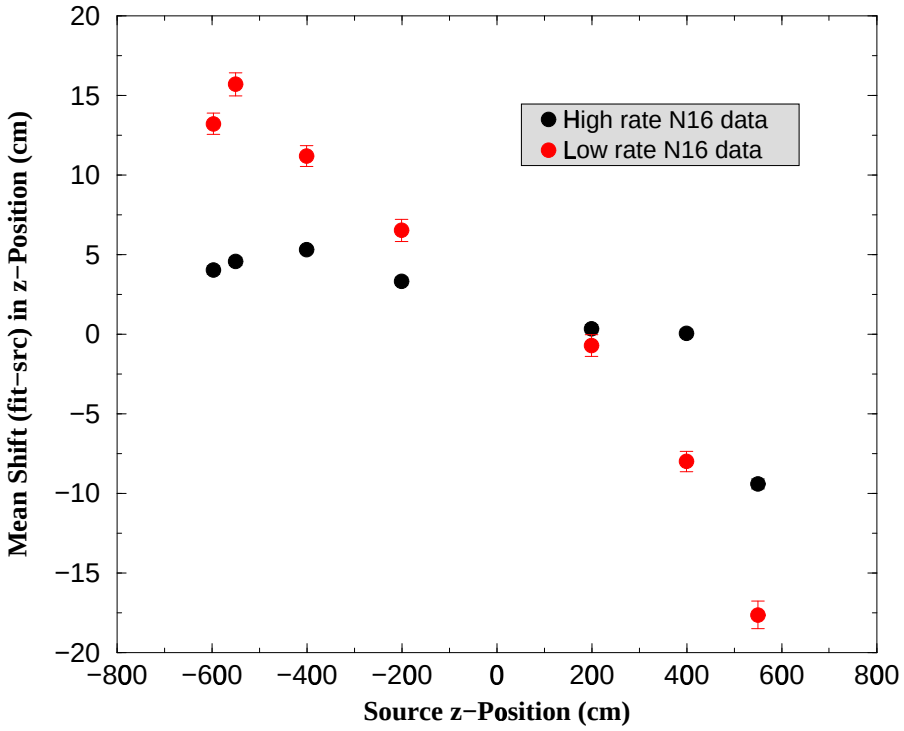

Figure 3.4: The shift in reconstructed position of the ^{16}N source as a function of source z position. Low rate data shows a shift inwards relative to high rate data. The effect at z=550 cm for the high rate data is caused by the neck of the acrylic vessel. Based on plots taken from [53].

The only significant difference between the ^{16}N source and neutrino data is the rate at which it is taken. ^{16}N source data is usually taken at high rate, with a detector PMT trigger rate[1] of typically $\sim$7 kHz, whereas neutrino data has a detector PMT rate of approximately 200 Hz. To determine the possible effect of this difference the ^{16}N source was run at low rate. The result is shown in figure 3.3. The χ^2 is higher for the low rate ^{16}N source and thus the detector rate has an effect on the timing calibration of the PMTs.

[1]Where detector PMT trigger rate is the detector trigger rate $\times$ average NHIT

A vertical scan of low rate ^{16}N runs was performed and reconstructed with the path fitter, the primary analysis fitter of SNO. A systematic shift inwards in the reconstructed position is seen between high and low rate runs, as shown in figure 3.4. If the same were true in neutrino data, this would represent a significant underestimation of the fiducial volume.

3.2.1 Characterising the Anomaly

The laserball was deployed in the centre of the detector, and operated at low rate. With the laserball equidistant from every PMT, the calibrated hit times should be equal. Figure 3.5 shows the average calibrated hit time as a function of the time since the PMT was last hit and read out. As this increases, the fully calibrated hit time becomes earlier.

Closer examination of ECA pedestal data provides another important aspect of the rate dependence. Figure 3.6 shows ECA pedestal data used to determine the charge pedestal of a particular channel. It was taken at a constant rate of 10 Hz and at a constant PED-GT delay of 150 ns.

It is important to stress that this data was taken at a constant rate and so, with the exception of the first data point, the time since the channel was last readout was constant. Nevertheless, the calibrated time is not constant and therefore it must be concluded that more than one effect is present. This is seen in figure 3.7 which shows data from a special ECA pedestal run where the readout rate was changed over the run: it was initially high and became progressively lower. This figure also shows a distinct difference between odd and even cells, presumably because of the two TACs used in the CMOS chip.

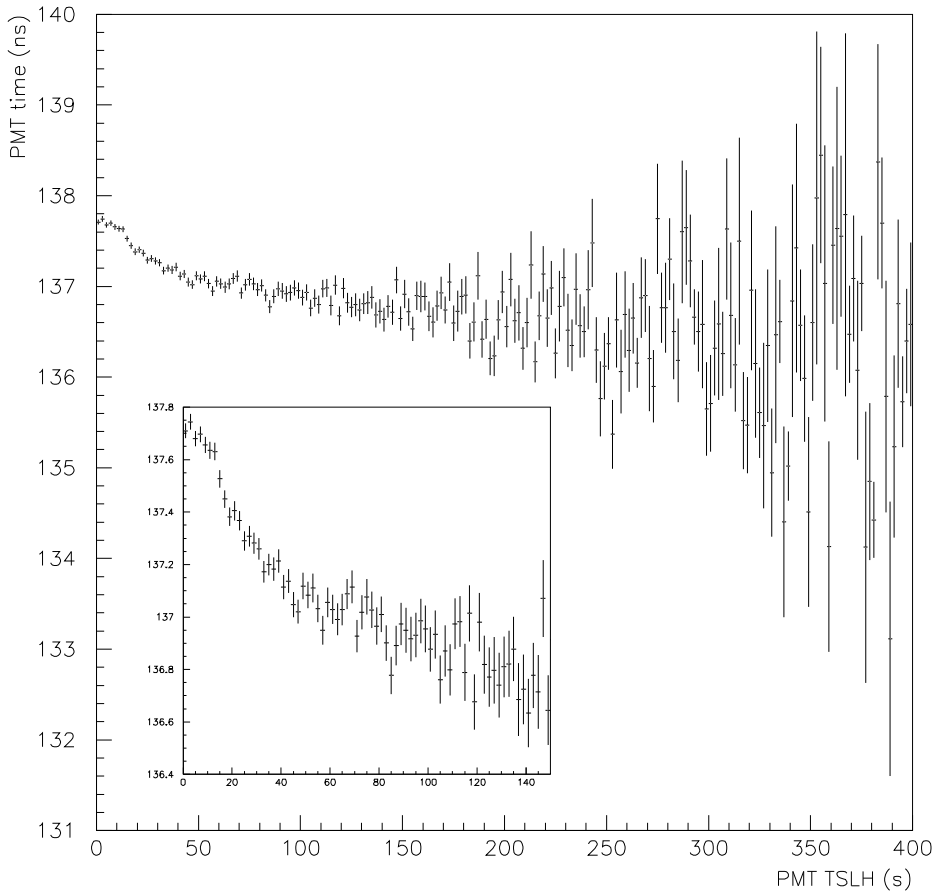

Figure 3.5: Calibrated PMT hit times (with a 100 ns offset) for a central low rate laserball run as a function of the time since the PMT was last hit (TSLH).

3.3 The HCA Model

As was mentioned in section 3.2.1 and can be seen clearly in figure 3.7, odd and even cells behave in a similar, yet distinct manner. There is no significant structure below this level indicating that although the ECA calibration does not return the correct time, it can still be used to remove the complexity inherent at the cell level. After the ECA has been applied, the HCA has only to consider the

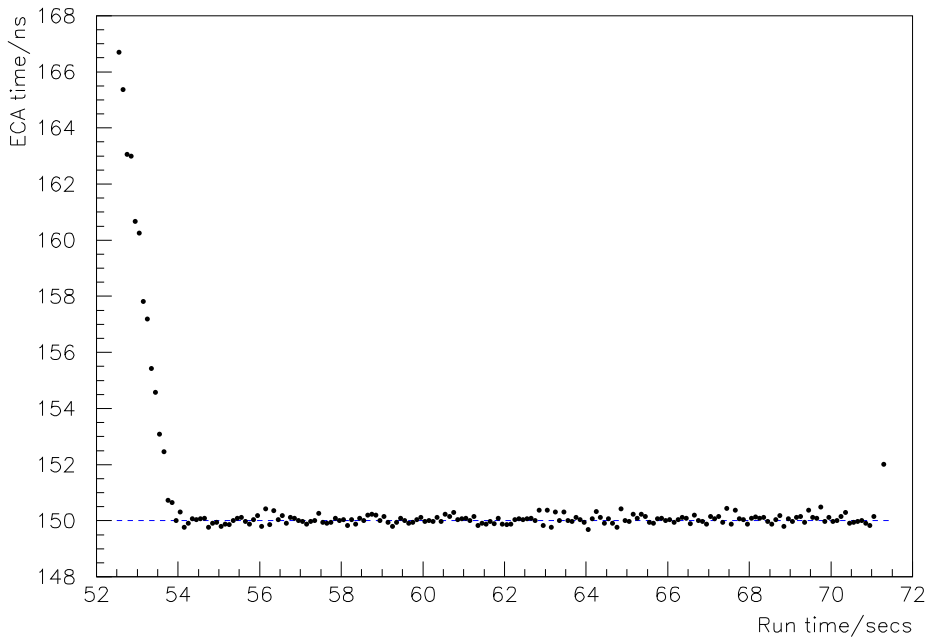

Figure 3.6: ECA calibrated PMT times for a single channel during an ECA pedestal calibration run (PED-GT delay of 150 ns).

two TACs (per channel) individually. This defines the HCA channel, the level at which the HCA operates.

One might wonder if, as the ECA calibration is incorrect, it is valid to use the returned ECA time. The answer is not clear. A simplified model of the ECA calibration is:

$$\text{calibrated time} = m \times (\text{TAC} - \text{pedestal}) \tag{3.2}$$

where m is the gradient of the TAC. Figure 3.7 implies that the pedestal subtraction in equation 3.2 is correct but m is not constant. In reality, the ECA calibration is not a linear transformation, but:

$$\text{calibrated time} = f(\text{TAC} - \text{pedestal}) \tag{3.3}$$

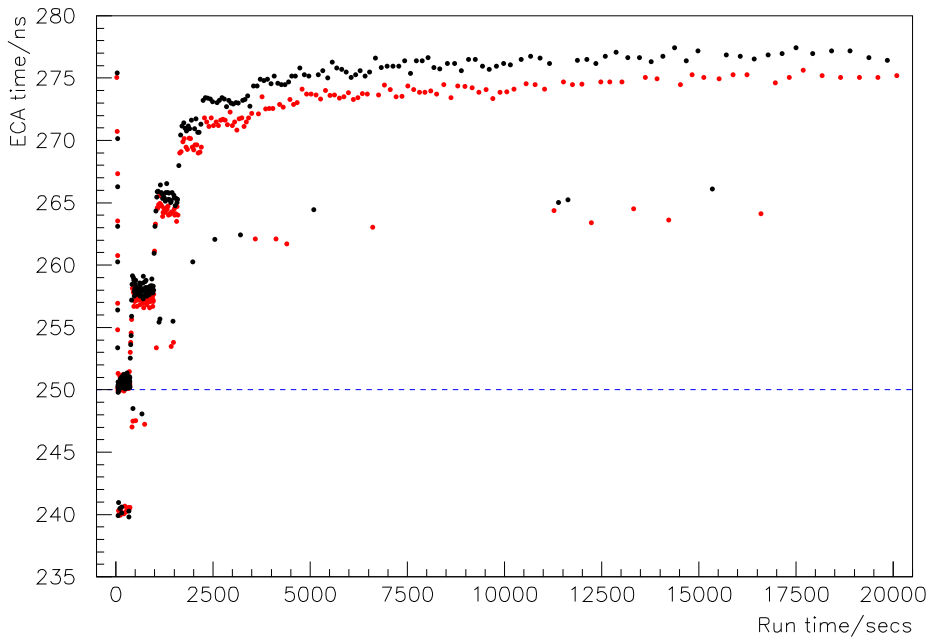

Figure 3.7: ECA calibrated PMT times for a single channel during a variable rate pedestal task run with PED-GT delay of 250 ns. The channel rate was initially high (1 Hz) and then lowered in discrete steps. Stable states are obtained during constant rate periods. The black and red points correspond to the two TACs (odd and even cells) for this channel. The readings offset by 10 ns are erroneous (caused by a fault in the SOFT GT trigger) and should be ignored.

where f is some arbitrary function determined from ECA calibration data and valid at high rate. If, at low rate, the functional form of f does not change:

$$\text{calibrated time} = f'(\text{channel state}) \times f(\text{TAC} - \text{pedestal}) \tag{3.4}$$

then the ECA calibration can be applied before the HCA. The HCA must simply apply $1/f'(\text{channel state})$. This is assumed to be the case and is justified by the resulting performance of the HCA.

The HCA must therefore track the state of each HCA channel. From the observations above it can be seen that HCA channels exhibit two distinct features.

Firstly, the action of reading out a HCA channel causes a discrete change in the ECA calibration of that channel. This can be seen in figure 3.6. For a pedestal event, this change is initially constant (approximately) for each HCA channel (remember figure 3.6 is for two HCA channels) but decreases as the ECA state is approached. Secondly, each HCA channel gradually returns to a low rate state if it is not read out as can be seen in figure 3.7.

Both these features are included in the HCA model. Considering a pedestal event at a constant PED-GT delay, the effect of readout is approximated by a constant and discrete change in the calibrated time. The functional form of the return to the zero read out state is approximated by simple exponential decay with time constant λ. These approximations are only valid when the channel is being readout at low rate.

Therefore, the ECA calibrated time of a fixed point on the TAC slope (constant PED-GT delay) will obey the following equations near the low rate state:

$$\text{Readout} \qquad \mathrm{T}^{\mathrm{ECA}}_{new} = \mathrm{T}^{\mathrm{ECA}}_{old} - h \tag{3.5}$$

$$\text{Recovery} \qquad \mathrm{T}^{\mathrm{ECA}}_{new} = \mathrm{T}^{\mathrm{ECA}}_{zero} - (\mathrm{T}^{\mathrm{ECA}}_{zero} - \mathrm{T}^{\mathrm{ECA}}_{old})e^{-\lambda t} \tag{3.6}$$

Where t is the time since the last readout, $\mathrm{T}^{\mathrm{ECA}}_{zero}$ is the theoretical ECA calibrated time corresponding to no readout and h is the change caused by readout.

Equations 3.5 and 3.6 can be used to track a fixed point on the TAC slope. This point can then be used to calculate the effective gradient of the TAC slope, as shown in figure 3.8. As a result of the approximations made in modelling the HCA behaviour, the correction is not valid close to the ECA state. If a HCA channel approaches this state, the ECA calibration is assumed to be correct. The HCA is not applied for the duration that the channel is in this regime. As neutrino data is typically taken at very low detector rates, the high rate ECA state rarely occurs.

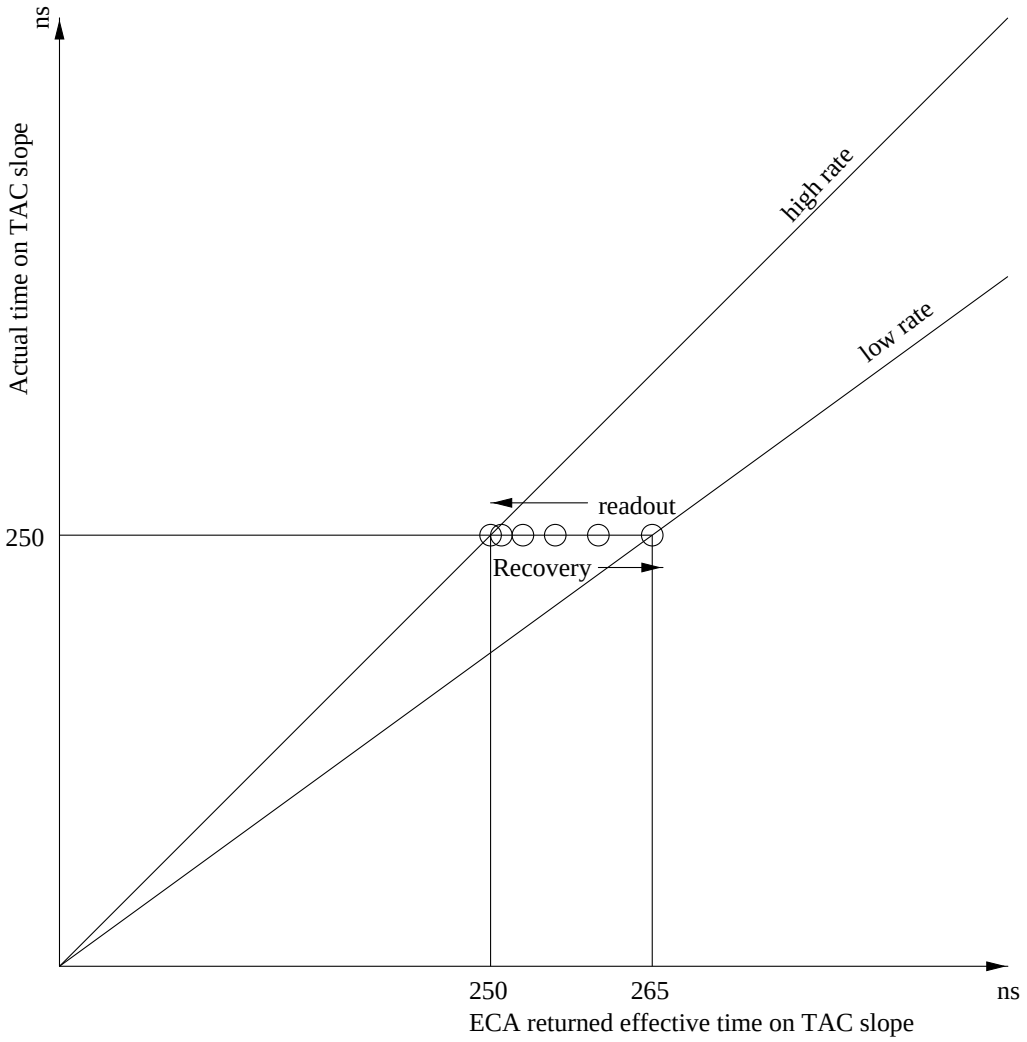

Figure 3.8: The HCA tracks the effective gradient of the TAC slope (using calibrated ECA times) so that the returned ECA time can be converted to the ECA time that would have been returned had the channel been in a high rate state. (The value of 265 ns for the 250 ns pedestal is purely illustrative).

3.4 Implementation of the HCA

3.4.1 The HCA RAA Subprocessor

The HCA is implemented as a RAA[2] subprocessor within SNOMAN. This is done to ensure that the data is time ordered. The subprocessor can be called in two

[2]Random Access Analyser

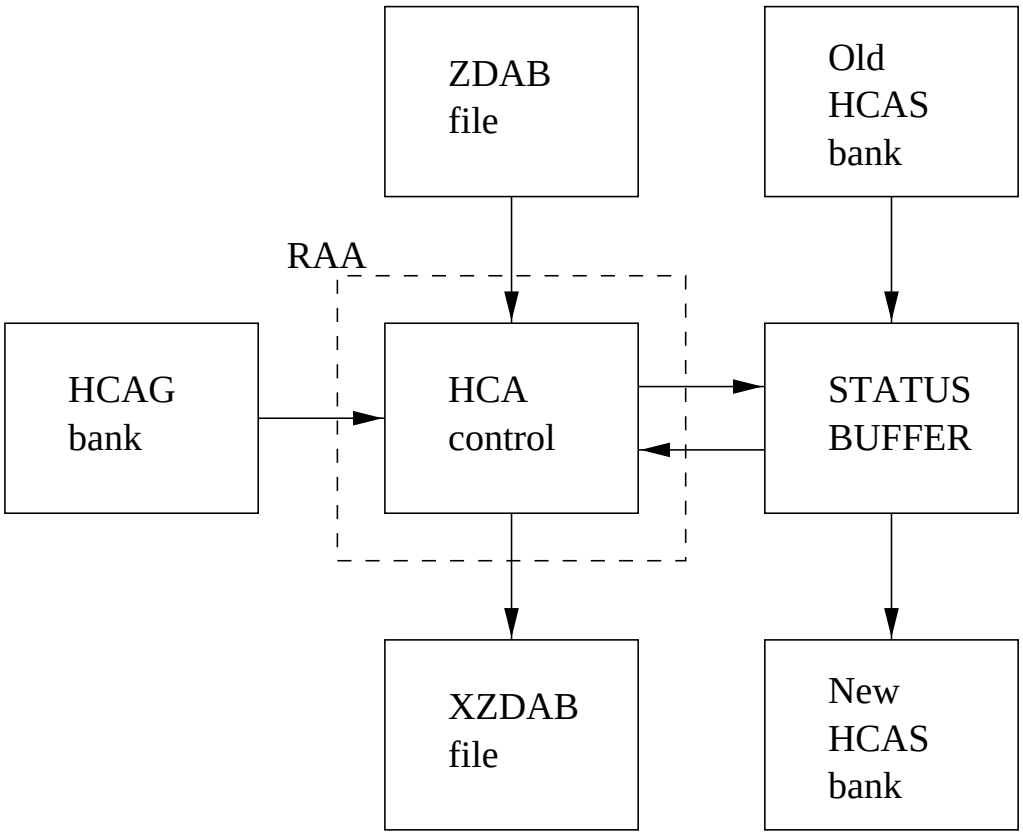

Figure 3.9: Operation of the HCA subprocessor when generating calibration information. The HCA initialises the status buffer of all channels using the preceeding HCAS bank and then, using calibration constants obtained from the HCAG bank, maintains the status buffer and generates calibration information as it reads the ZDAB file. This calibration information is packed into an extended ZDAB file, or XZDAB file. After the entire ZDAB file has been read, the status buffer is written out to a new HCAS bank for use with subsequent ZDAB files.

modes. The first mode processes HCAG runs (see section 3.4.2) and generates the calibration constants, while the second generates the calibration information and packs this into the data-structure for storage in the ZDAB[3] bank of the event. The calibration information, once present, is applied by the calibrator.

A flowchart showing the operation of the HCA when generating the calibration information in shown in figure 3.9. When performing a calibration the HCA

[3]Zebra Data Acquisition/Analysis Bank.

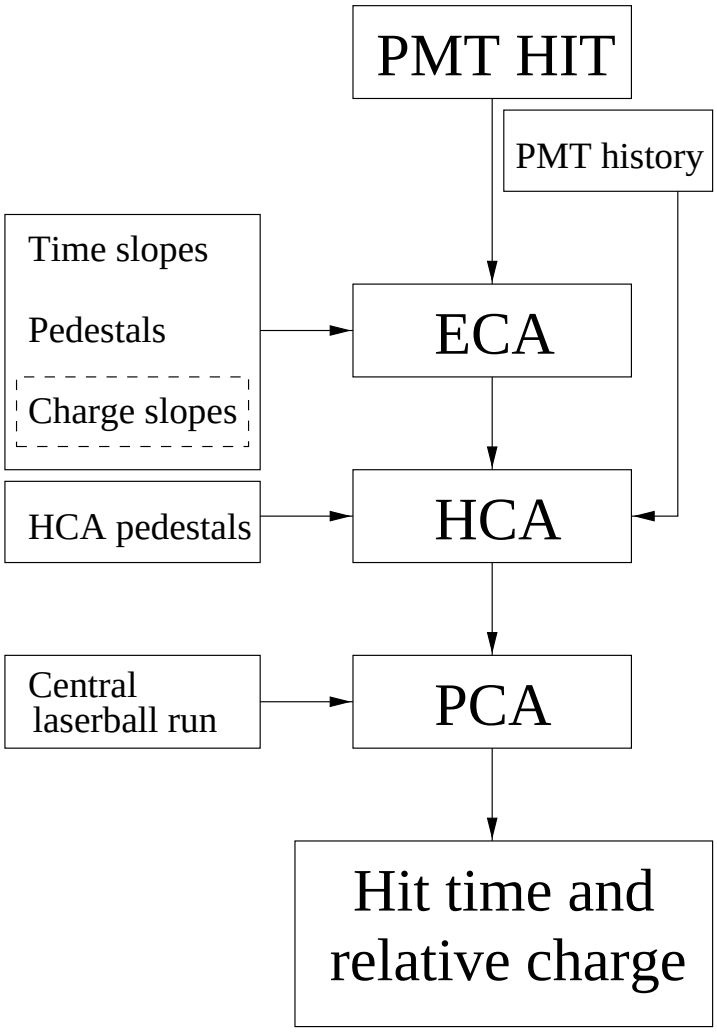

Figure 3.10: PMT calibration in SNO. The calibration flow is shown along with the information required for each stage. Charge slopes are not taken as a central laserball run provides the PCA with enough information for the charge calibration.

subprocessor maintains a record of the status of each HCA channel. This contains the effective position of a 250 ns pedestal and a timestamp of the last readout. Entire subruns must be processed without any data selection as every event must be considered in order to maintain an accurate channel status. At the end of each subrun the detector status is written out to a HCAS bank to provide the initial status of the next subrun.

The calibration information is packed and chained to the ZDAB bank. This allows ZDABs containing the calibration information to be written by SNOMAN without having to write out the full data-structure. When such an extended ZDAB is read by SNOMAN the extension is recognised and unpacked into the 'short fat' PMT banks, ready to be applied by the calibrator.

The full PMT calibration in SNO is shown as a flowchart in figure 3.10. After HCA has been applied upstream analysis can proceed as though the detector was at high rate.

3.4.2 Parameter Determination

For each HCA channel, the decay time constant λ, the effect of a readout h, and the state corresponding to no readout T_{ramp}^{ECA}, must be determined. These constants are obtained from dedicated pedestal runs, known as HCAG runs. In these runs pedestals are taken for the entire detector simultaneously at a constant PED-GT delay. The time between pedestal events is chosen randomly between 1 and 240 seconds, with the average channel readout rate forced to be close to neutrino readout rate.

Using SNOMAN, data from an HCAG run is processed and for each HCA channel the above parameters determined. A flowchart of this process is shown in figure 3.11. This is done by minimising the average difference between the predicted value of the pedestal and the actual value. Because the detector is triggered globally during HCAG runs, the builder is frequently overwhelmed and orphan production is significant. This results in events with large numbers of hits missing (lost to the orphan events). It is unwise to try to rebuild these partial events, but it is possible to keep track of channel triggers. This is because the only events are detector wide pedestals. Even if they have only been partially

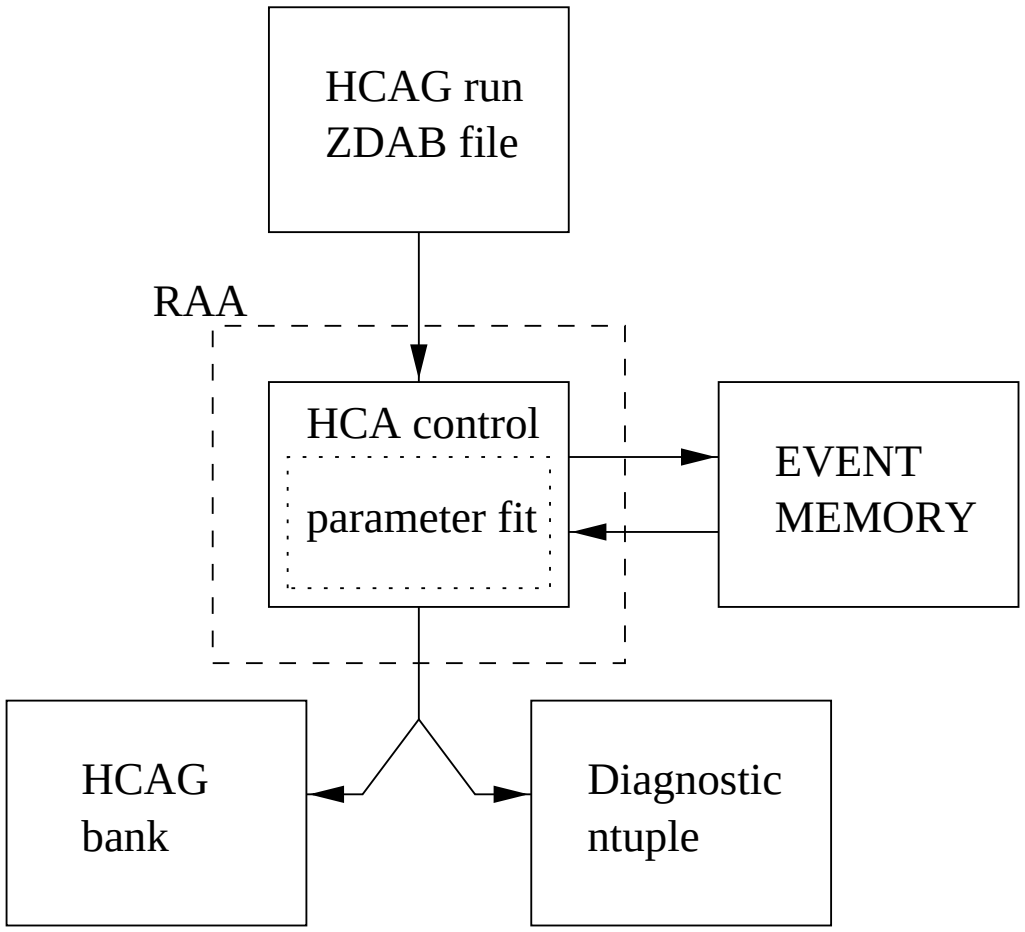

Figure 3.11: Operation of the HCA subprocessor when determining the calibration constants. A HCAG run (ZDAB file) is read in all events stored in memory. For each HCA channel, the memory is read and a fit done to determine the HCA calibration constants. The results are written to a HCAG bank for future use and diagnostic output is generated (if requested).

assembled by the builder, every channel has been readout. The code is therefore aware that a channel readout has taken place (and thus able to accurately track the channel's state) even if it is unable to use that readout's calibrated time in the fit.

The result of the parameter determination is shown in figure 3.12 which shows the improvement in the pedestal resolution. This is the correction acting on the

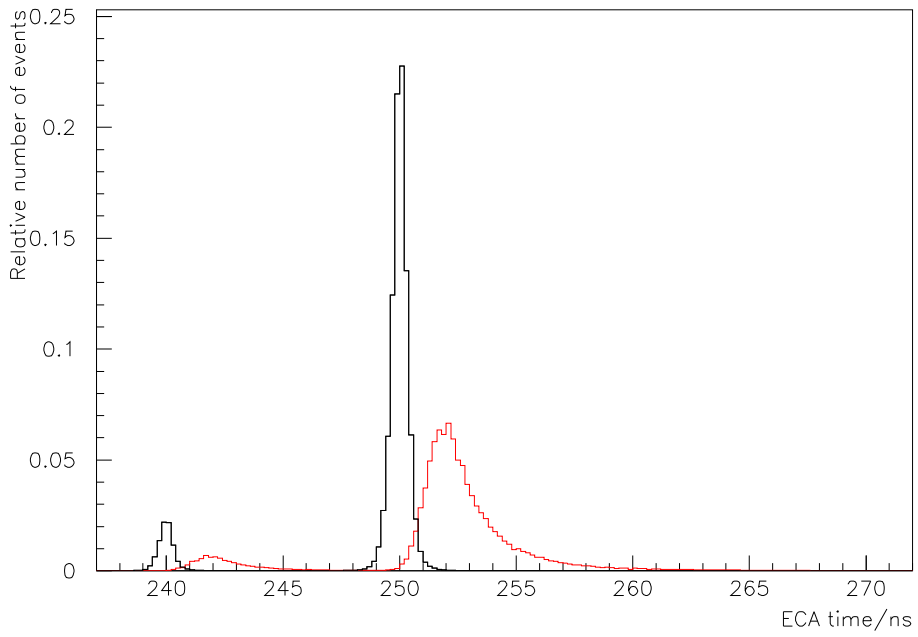

Figure 3.12: Neutrino rate pedestals at 250 ns. The red line is before calibration and the black line is after calibration. The small peak about 10 ns before is caused by a fault in the SOFT GT trigger and is not considered in the analysis.

data from which it is determined, so the dramatic improvement is somewhat artificial. However, it does demonstrate that the model is sufficient.

The extent by which channels are affected is shown in figure 3.13. The mean maximal correction (for a 250 ns pedestal) is about 3 ns but it is the large tail to over 20 ns which is important; over 5% of channels have a maximal correction larger than 10 ns.

Calibration constants are stored in the HCAG banks for use by SNOMAN.

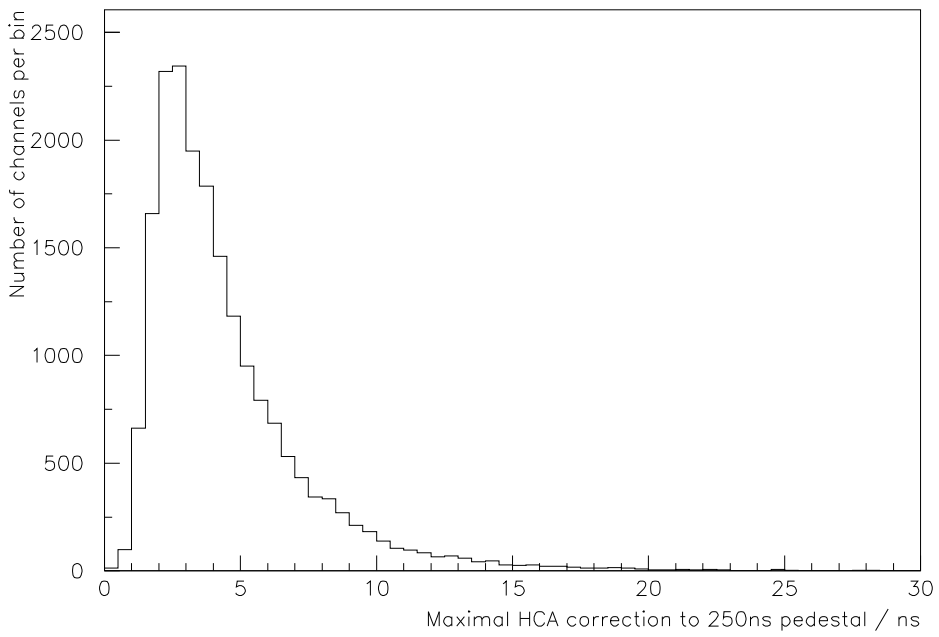

Figure 3.13: The difference between the ECA state and the zero readout state for a 250 ns pedestal.

3.5 Performance of the HCA

3.5.1 HCAG Pedestal Results

A HCAG run with a PED-GT delay of 250 ns was used to generate the HCA calibration constants. Two additional HCAG runs were also taken, with PED-GT delays of 150 ns and 50 ns. These runs can be used to check the performance of the HCA correction. This is shown in figure 3.14. The HCA performs very well, sharpening up the pedestals considerably.

The pedestal residuals are shown in figure 3.15. There is a small systematic shift in the pedestal central value after HCA has been applied. This implies that the 250 ns pedestal is not actually at 250 ns. This is visualised in figure 3.16.

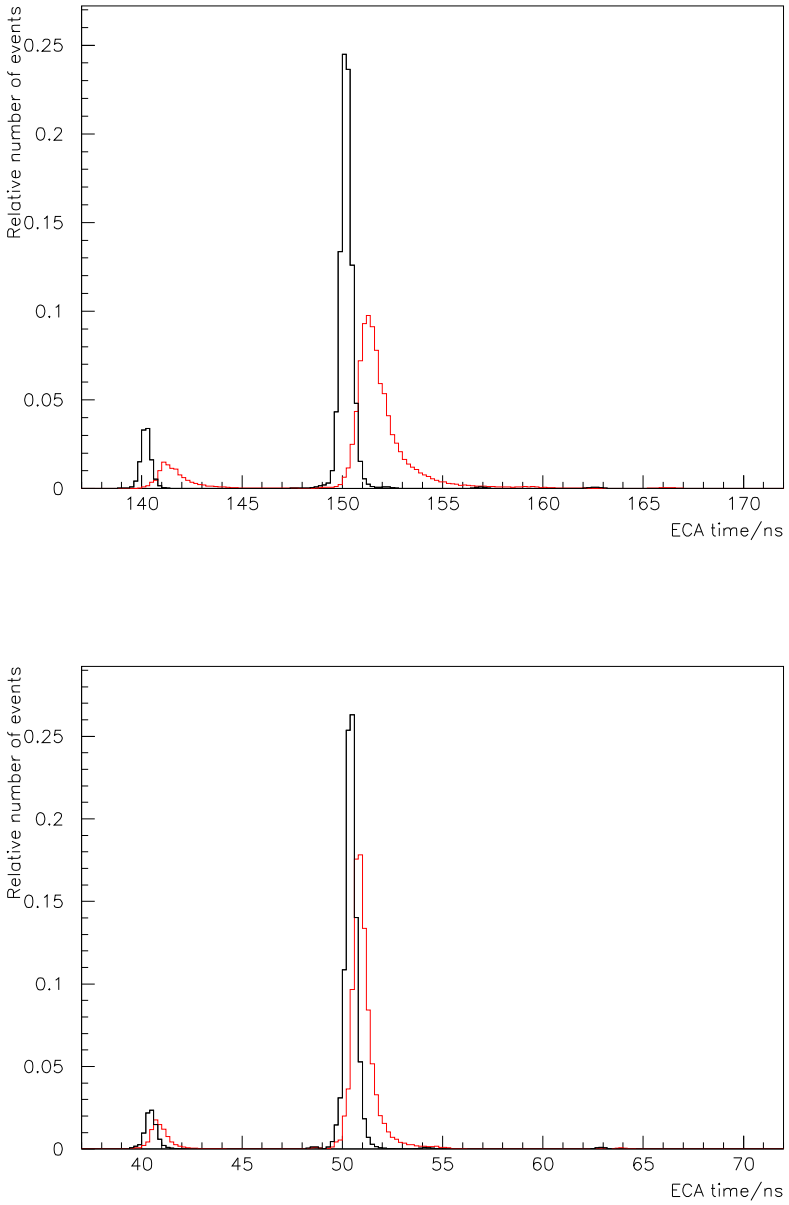

Figure 3.14: Neutrino rate pedestals at 150 ns (top) and 50 ns (bottom). The red line is before calibration and the black line is after calibration.

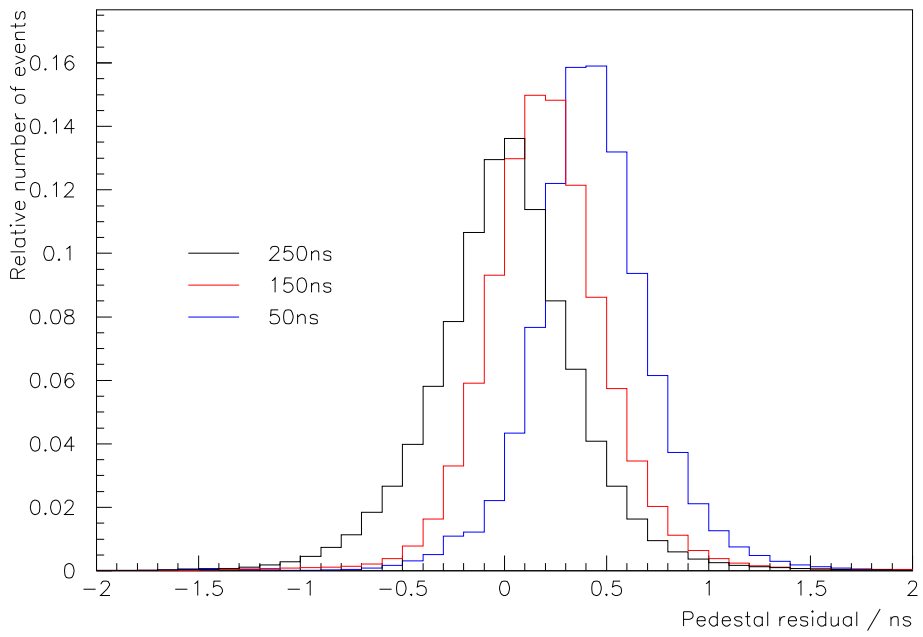

Figure 3.15: Pedestal residuals after HCA has been applied. A small systematic shift is seen indicating a small timing offset is present in the pedestals.

The pedestal offset, δ, can be determined by minimising all the pedestal residuals. It is found to be $\sim$0.5 ns, and the effect of this addition correction on the pedestal residuals is shown in figure 3.17. These pedestal residuals are about two times wider than the corresponding high rate ECA pedestals.

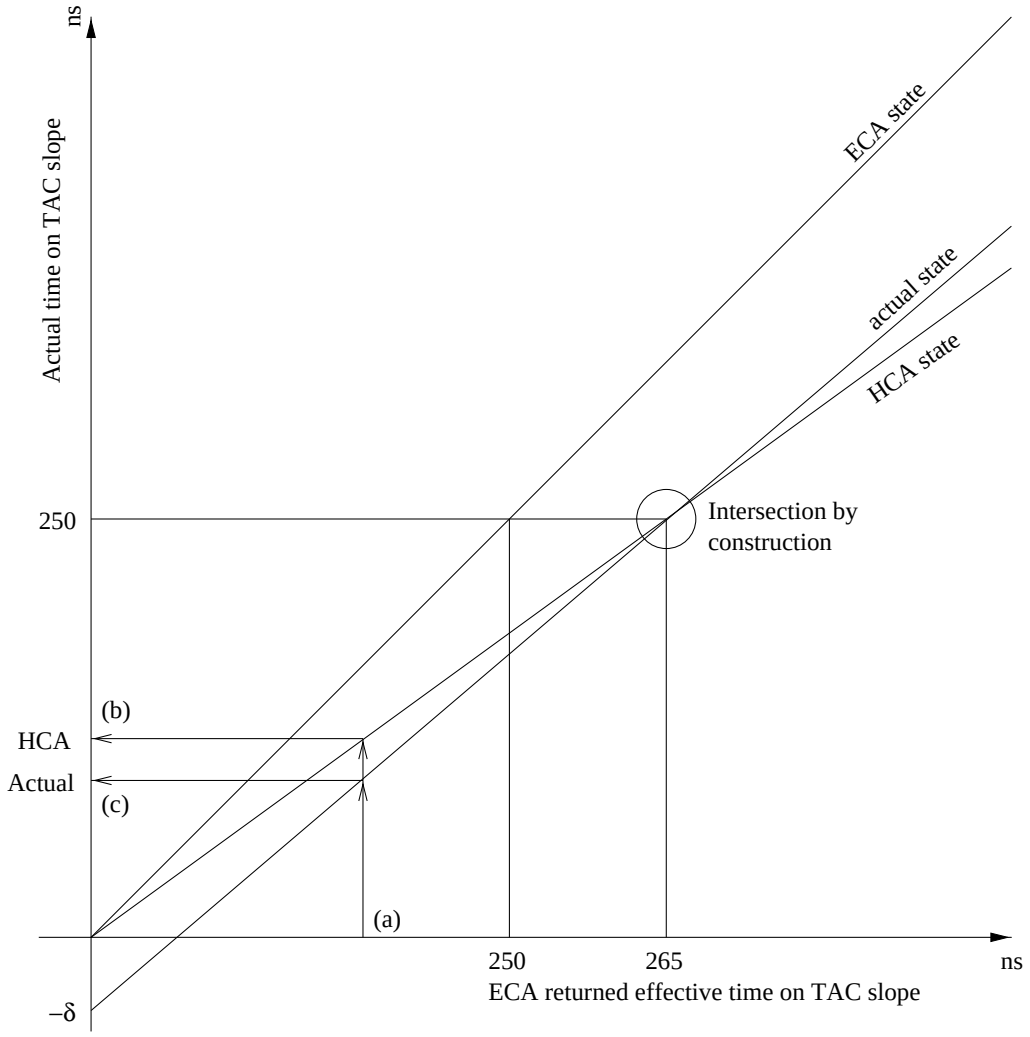

Figure 3.16: The effect of a small timing offset δ. By construction, the HCA state agrees for the 250 ns pedestal. The offset was found to be $\sim$0.5 ns, thus the 250 ns pedestal was actually nearer 250.5 ns. Therefore given an ECA returned time of (a) the HCA will return time of (b) when the actual time is (c). (The value of 265 ns for the 250 ns pedestal is purely illustrative).

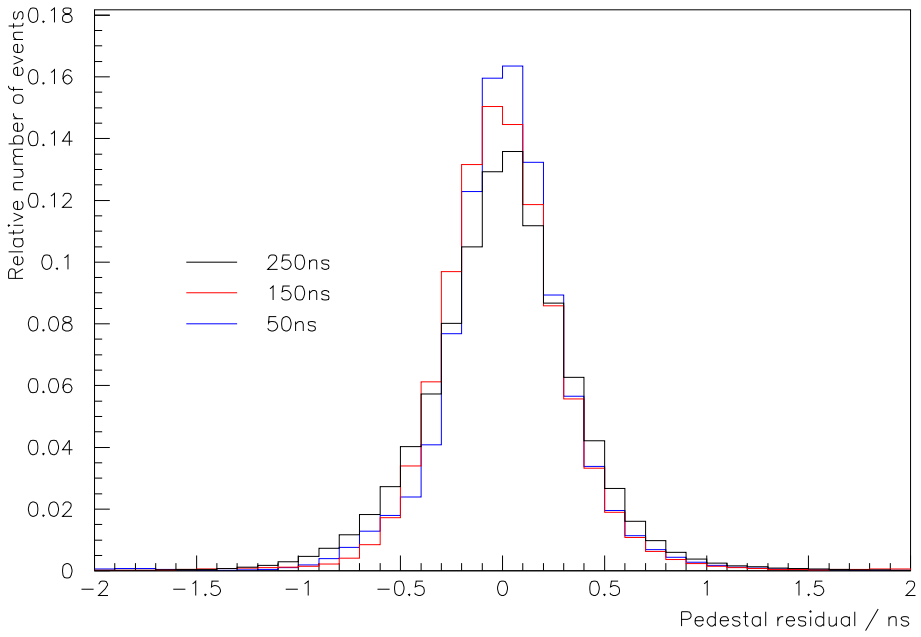

Figure 3.17: Pedestal residuals after HCA has been applied and the pedestal timing offset corrected.

3.5.2 New χ^2 Distributions

It was the χ^2 distributions which initially drew attention to the calibration problem. It is therefore natural to return to these distributions as a means of demonstrating the effect of the HCA. Figure 3.18 shows both the improvements to low rate ^{16}N data and neutrino data. Both have improved considerably, although a small residual effect remains. The size of this effect corresponds to an average timing error of $\sim$0.23 ns. This is a factor of $\sim$5 improvement over uncorrected data.

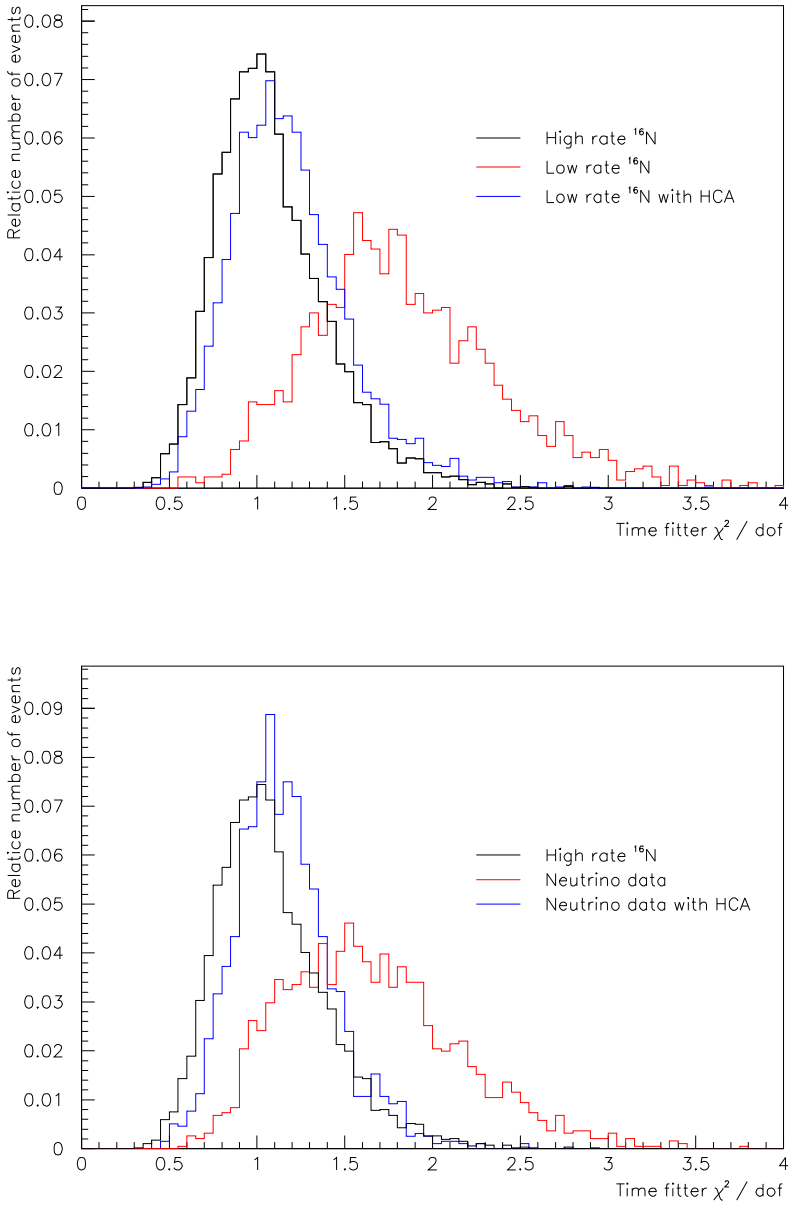

Figure 3.18: The time fitter χ^2 distributions of low rate ^{16}N data (top) and neutrino data (bottom) before and after HCA. Also shown is the χ^2 distribution for high rate ^{16}N data for comparison.

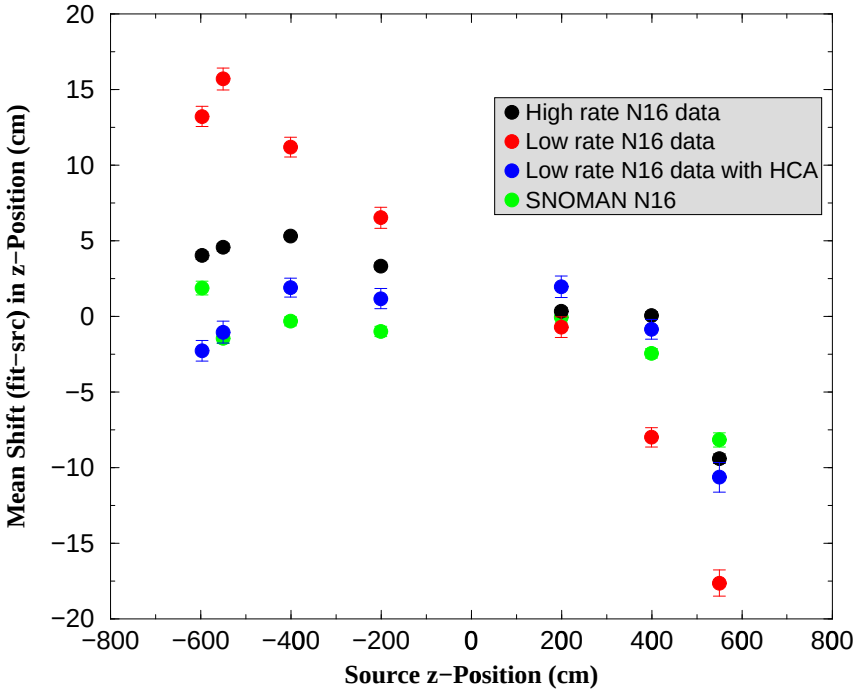

Figure 3.19: The shift in reconstructed position of the ^{16}N source as a function of source z position. The HCA corrects the inward shift seen in the low rate ^{16}N data. Based on plots taken from [53].

3.5.3 Fitter Performance

The ^{16}N Vertical Scan

The vertical scan of low rate ^{16}N runs was reconstructed after applying the HCA. The results are shown in figure 3.19. The shift in reconstructed position, which represented a 10% error in the neutrino flux measurement, has been negated for the low rate data and agreement with high rate data and SNOMAN has improved. The remaining discrepancy between both high and corrected low rate data and SNOMAN is included in neutrino analyses as a 3% systematic error in the neutrino flux measurement.

Neutrino Data

With the improvement in the reconstruction of low rate ^{16}N data established, it was expected that after applying the HCA to neutrino data, fewer events would reconstruct within the fiducial volume.

The actual effect of applying the HCA to neutrino data is shown in figure 3.20. The application of HCA shifted neutrino events inward, not outward, with a significant shift occurring for events reconstructing about 100 cm above the equator of the D_2O.

To understand the difference of applying the HCA to the ^{16}N scan and to neutrino data, one must first consider if the low rate ^{16}N runs are actually representative of neutrino data. Although the source was run at low rate, resulting in a detector rate comparable to that experienced in neutrino running, the distribution of PMT hits is considerably different. When the source is deployed off centre, the PMT's nearest to the source are hit more frequently than those more distant. Thus, a PMT readout rate differential forms across the detector and this will become more pronounced the further the source is positioned off centre. No such rate differential exists for neutrino data, and so the expected outward shift caused by the HCA should not be seen.

The Improved Timespoiler

To confirm that this is indeed what is causing the effect in the ^{16}N data, the timespoiler [45] was upgraded to perform the reverse of the HCA calibration to SNOMAN generated data: perfect timing was spoiled to simulate low rate conditions and the effect on reconstruction examined.

The result of fitting the ^{16}N source positioned at z=-400 cm is shown in figure 3.21, along with the applied HCA un-correction as a function of PMT z po-

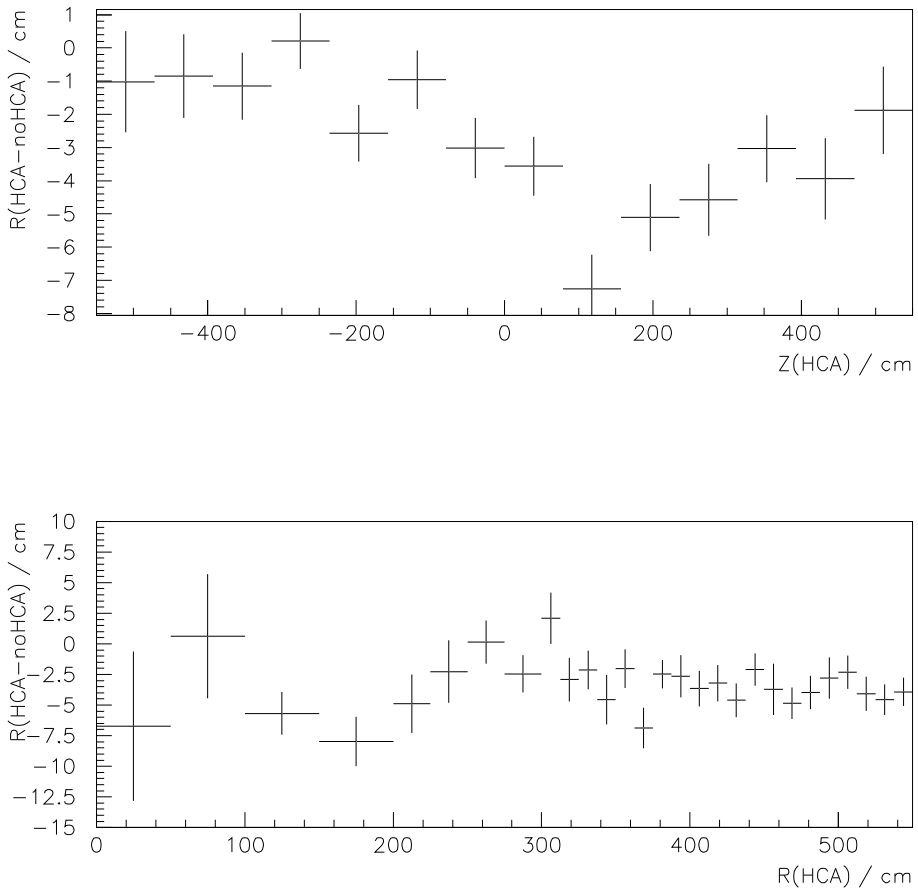

Figure 3.20: The effect of HCA on neutrino data. Events are shifted inward.

sition. Three things should be noted: firstly, the spoiled SNOMAN data exhibits the same reconstruction shift as the real low rate ^{16}N data; secondly, the applied HCA un-correction shows the overall readout rate differential as expected; and lastly, there is a large peak in the applied HCA un-correction for tubes around z=250 cm.

Returning to the HCAG runs, the origin of this peak can be determined. Figure 3.22 show the maximal HCA correction to the 250 ns pedestal as a function

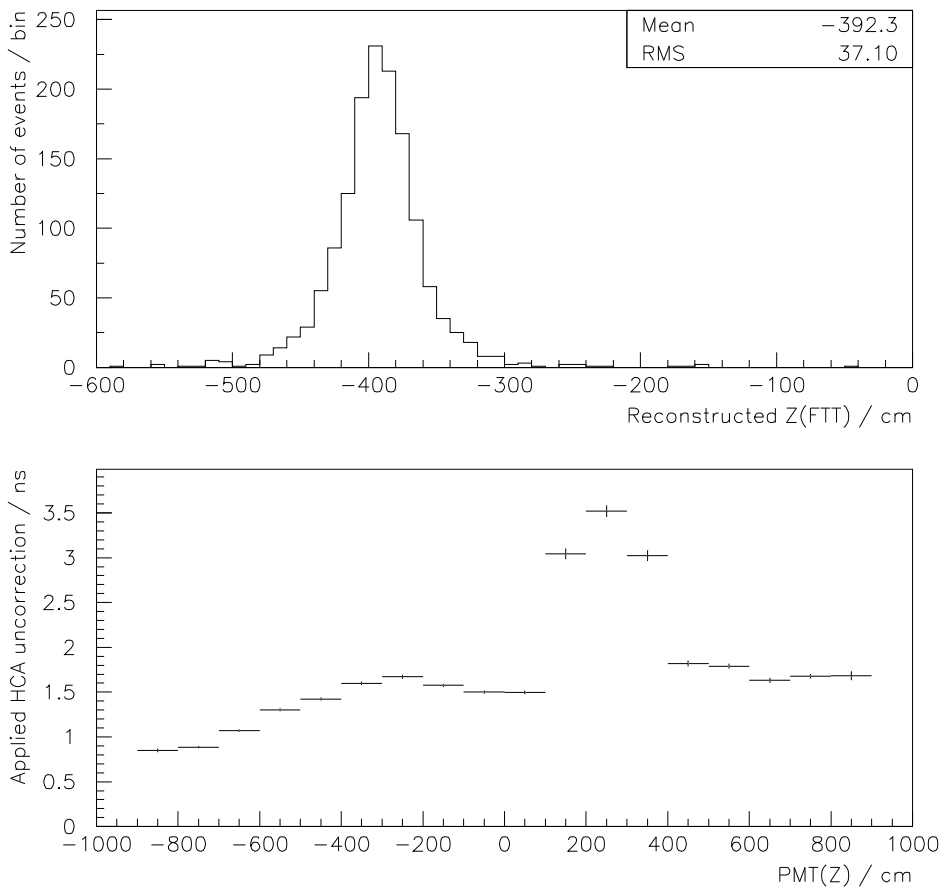

Figure 3.21: Reconstruction of Monte Carlo ^{16}N after the improved timespoiler has been applied. The reconstructed position has shifted inward as is seen in real low rate ^{16}N data. The applied spoiling (HCA un-correction) is shown as a function of PMT z position and shows the detector rate differential and a band of bad tubes.

of PMT z position. There is a band of very bad channels exactly at the location expected. This is purely accidental, but has important consequences for neutrino reconstruction. This band of bad PMTs, giving relatively early calibration times, pulls events towards it. When considering radial shifts this affects events at $z\sim$135 cm (assuming a volume weighted mean event position of about 450 cm).

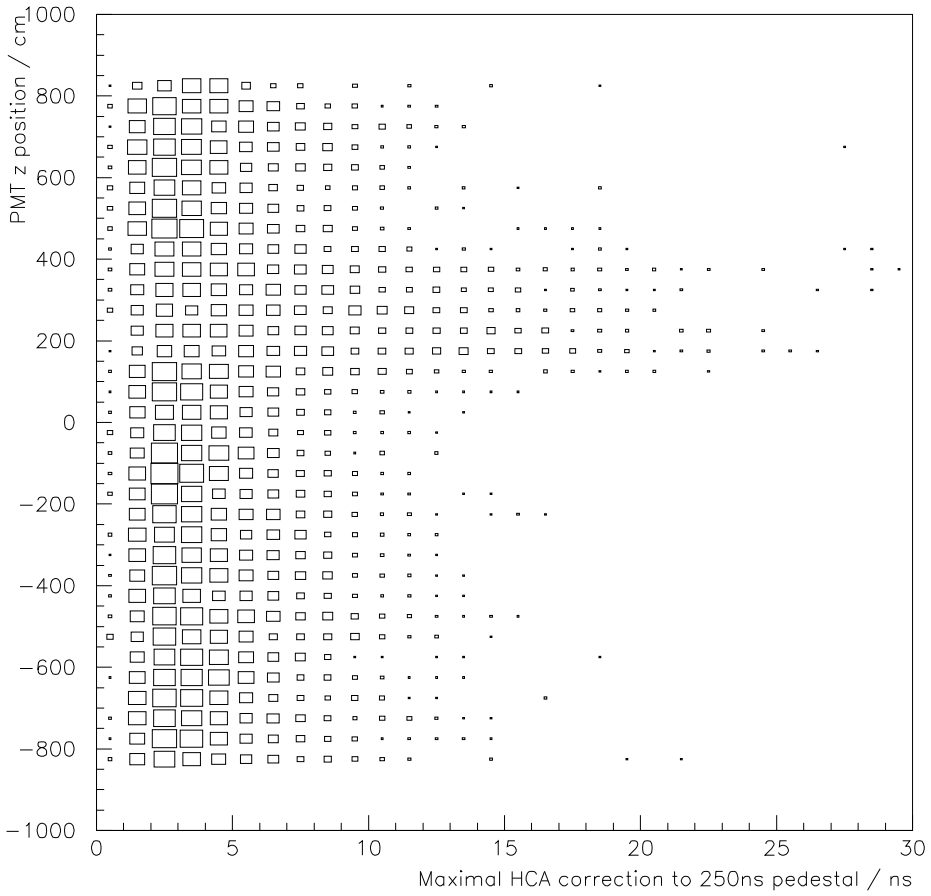

Figure 3.22: The maximal HCA correction to a 250 ns pedestal as a function of PMT z position. The band of bad tubes is clearly seen between 200 cm and 400 cm.

This is in good agreement with figure 3.20.

3.5.4 Long Term Stability and Validity

With the HCA calibration in place, one outstanding question remains: given that the HCAG runs were performed many months after the beginning of the data they were intended to calibrate, are they valid? For them to be valid, the hardware problem causing the effect must be stable.

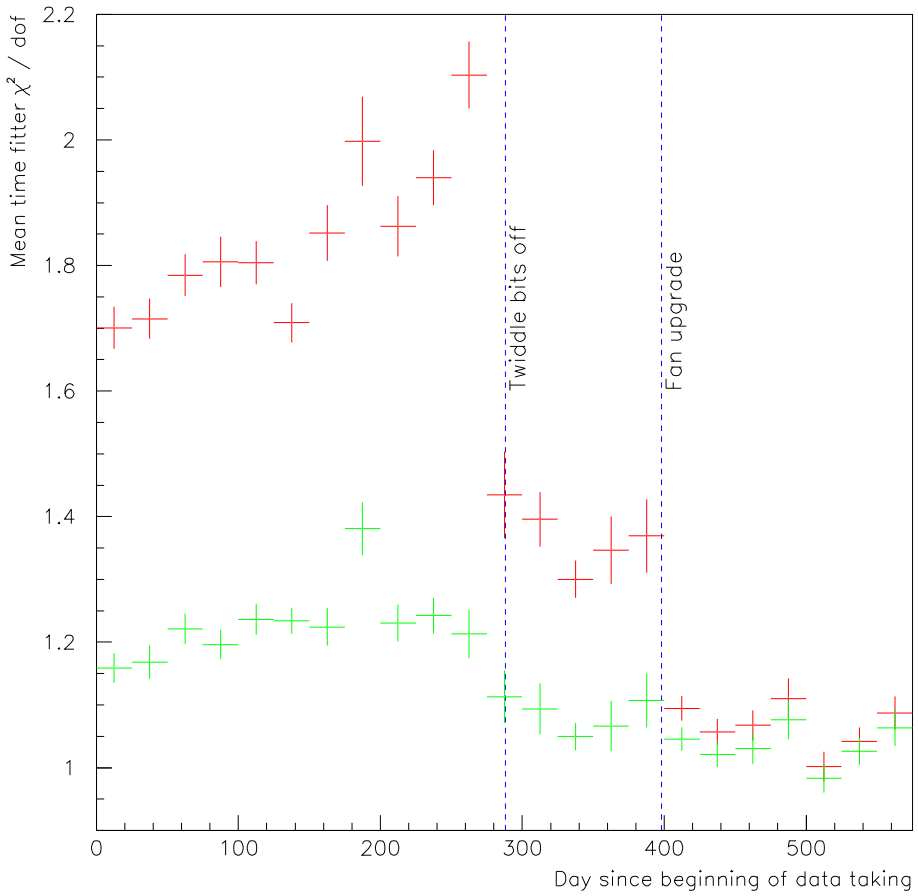

Figure 3.23: The mean χ^2 for neutrino data as a function of run day. The χ^2 after the HCA has been applied (shown in green) is consistently lower than before (shown in red). The two hardware upgrades are also shown.

Figure 3.23 shows the χ^2 for neutrino data since the beginning of official data taking, including data taken after the hardware upgrades had been implemented (see section 3.6). The overall performance is very good, with a slight increase in χ^2 occurring before the first hardware upgrade. This is attributed to a steady drop in the detector rate over this period: as the detector rate drops, the HCA correction becomes more important. This is another indication that the HCA is

not perfect. However, the hardware effect is stable enough for the HCA to be considered valid for all the data.

3.6 Hardware Solutions

While the HCA allows old neutrino data to be calibrated, it was undesirable to continue taking data with this hardware problem. This section discusses the results of the hardware upgrades considered and implemented.

3.6.1 Forced Readout

This first approach to solving the history effect was to force the detector to, or very close to, the stable state that was achieved in high rate calibrations. This can be achieved by running a detector wide pedestals (similar to those used in HCAG runs) during neutrino runs. The results from interlaced detector wide pedestals every 5 or 10 seconds during a central low rate ^{16}N run are shown in figure 3.24.

The interlaced pedestals improved the timing calibration, but were a mixed blessing. In addition to improving timing they could also, at least potentially, be used to provide a running ECA calibration and electronic health check of the detector. However the sustained increased data rate was problematic. With 5 second pedestals the data rate increased by an order of magnitude. While only inconvenient to write all this data to tape, or prescale it to a useful amount, the increased orphan production during event building could not be tolerated.

At a more aesthetic level it was felt that this solution (running the detector in a mode never envisaged) did not really solve the problem but merely sidestepped it. It was therefore unattractive as anything but an interim solution.

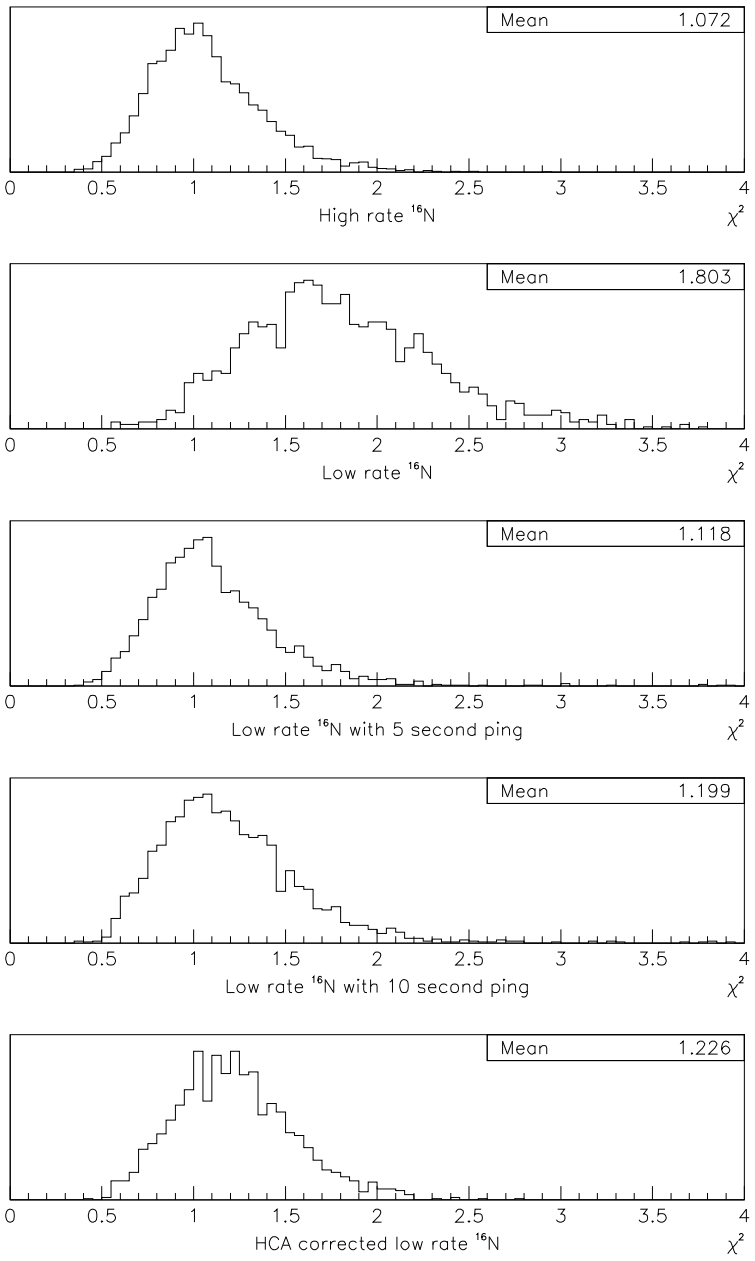

Figure 3.24: The effect of forced readout. Pinging with pedestals at 5 or 10 second intervals largely corrected the problem but this solution caused other problems and was deemed unsatisfactory.

3.6.2 Cooling

On closer examination of the electronics it was found that a strong correlation between the size of the effect and the temperature of the electronics existed. Crate cooling was inadequate, producing large temperature gradients across individual crates.

Two steps were taken to improve this situation. The first, implemented on 17th August 2000, was to reduce heat production in the electronics. This was achieved by switching off the secondary current sources that provided fine tuning of the TAC slopes (controlled by the twiddle bits). The second, implemented on 5th December 2000, was to install a fan upgrade capable of cooling the electronics adequately.

HCAG runs were taken for the new hardware configurations. The pedestals for theses runs are shown in figure 3.25. The upgrades have improved things considerably, however the HCA still improves timing. The effect of these upgrades on the neutrino data χ^2 can be seen in figure 3.23.

3.7 Conclusions

The HCA is able to largely correct the output of the ECA timing calibration for the data taken before the hardware upgrades were implemented. Low rate source reconstruction is now understood and the vertex shift of the path fitter is concluded to be less than 1% [54], resulting in a 3% uncertainty in the neutrino flux measurement.

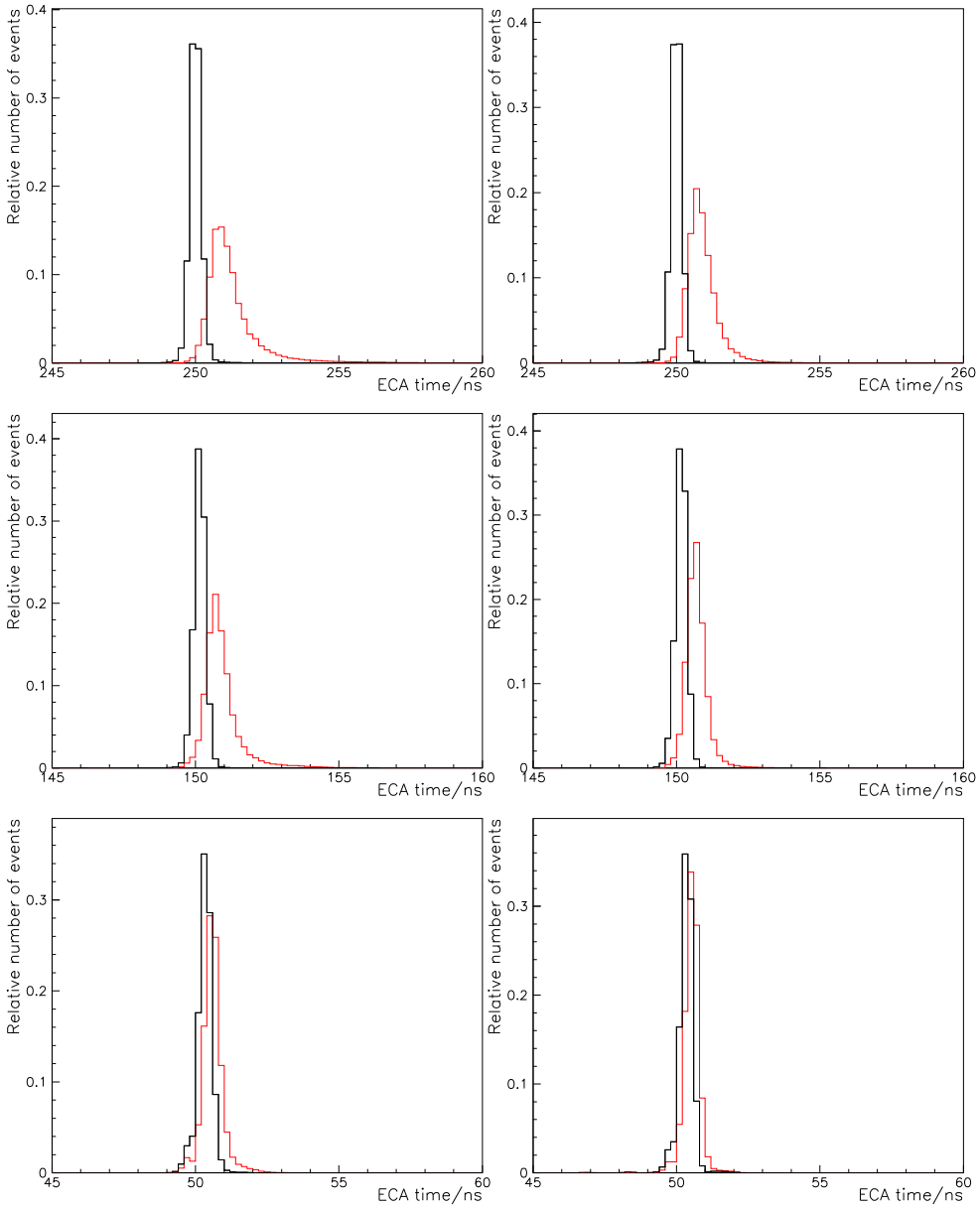

Figure 3.25: The HCAG pedestals taken after the hardware fixes. Pedestals after turning secondary current sources off are shown on the left and pedestals after the fan upgrade are shown on the right. The red lines are before HCA calibration and the black lines are after HCA calibration.

Chapter 4

Neutrons

In this chapter, neutron data taken with salt deployed in the D_2O is compared with the Monte Carlo predictions. The author was responsible for all upgrades to the neutron transport code within SNOMAN since its original implementation.

4.1 Introduction

The principal neutral current detection capability of SNO relies on the disintegration of the deuteron atom into a proton and neutron:

$$\nu_x + \mathrm{d} \quad \rightarrow \quad \nu_x + \mathrm{p} + \mathrm{n}$$

and the subsequent detection of the captured neutron, as was discussed in section 2.2.

In the pure D_2O and salt phases of the experiment, neutrons are detected by the light produced after they capture on deuteron or ^{35}Cl atoms respectively (see section 2.3). Identification of these neutrons is achieved with a statistical separation which relies on PDFs generated by SNOMAN. It is therefore important to demonstrate that SNOMAN is capable of accurately describing the transport of neutrons and simulating the light produced following a capture.

4.2 Neutrons in SNOMAN

The neutron code present in SNOMAN is taken from MCNP [55] and the original implementation of the inclusion of this code is described in [56]. Since that time, several upgrades have been made and these are detailed below.

4.2.1 Implementation of New ENDFs

New ENDFs[1] became available after the original implementation of MCNP in SNOMAN. The inclusion of these new files is desirable as they replace several natural data tables with isotope specific tables and add new tables that are required for the proper transport of neutrons through some elements of the detector.

Of particular importance is the addition of a table for ^{17}O. ^{17}O has a neutron capture interaction, ^{17}O(n,α)^{14}C, which has a large thermal cross section ($\sim$235 mb). Because no neutron transport table existed for ^{17}O, this interaction was added to the transport code in an ad hoc fashion. Inclusion of the ^{17}O table allows this code to be removed and ^{17}O to be treated in exactly the same way as all other isotopes.

The new tables required scattering laws that were not present in SNOMAN. These were installed into SNOMAN from the original code in MCNP.

4.2.2 (n,γ) Interactions

Previously, thermal (n,γ) captures on H, D, ^{35}Cl, ^{58}Ni, ^{60}Ni and ^{62}Ni were coded in SNOMAN. This has been extended considerably. SNOMAN now supports captures on: ^{23}Na, ^{24}Mg, ^{25}Mg, ^{26}Mg, ^{27}Al, ^{28}Si, ^{29}Si, ^{30}Si, ^{32}S, ^{34}S, ^{39}K, ^{40}K, ^{41}K, ^{40}Ca, ^{42}Ca, ^{44}Ca, ^{46}Ca, ^{48}Ca, ^{50}Cr, ^{52}Cr, ^{53}Cr, ^{54}Cr, ^{55}Mn, ^{54}Fe, ^{56}Fe, ^{57}Fe, ^{58}Fe and ^{207}Pb.

[1] Evaluated Nuclear Data File

This allows neutron source simulation to include (n,γ) captures in a variety of materials found in the detector. These include the cavity mine rock and, in particular, the materials used in neutron sources and in their deployment structure. This was intended to allow simulation of "hot rock" neutron induced γ-ray sources, although these were never constructed. Nevertheless, simulation of neutron sources benefit from the inclusion of these captures allowing comparisons between source data and Monte Carlo at the percent level.

4.2.3 The ^{36}Cl Cascade Response

With the presence of $\sim$0.2% NaCl in the D_2O, over 90% of neutrons capture on ^{35}Cl producing an excited state of ^{36}Cl at 8.6 MeV. This nucleus subsequently γ cascades down to the ground state. It is this cascade that will provide the ability to distinguish NC events from CC events in the salt phase. The cascade is very complicated, with over 380 routes more probable than 1×10^{-5} to the ground state. Angular correlations between emitted γ-rays are only known for 54% of the total intensity.

The ^{36}Cl cascade scheme currently in SNOMAN (version 4.0192) is from Nucl. Phys. A 386 (1982) 245, with the angular correlations from Nucl. Phys. A 77 (1966) 267. There has been some question whether this scheme is correct to the accuracy required. As there has been recent work on the ^{36}Cl cascade a new level and intensity scheme is available. This was incorporated into SNOMAN and, using the old angular correlation information, the NHITS and θ_{ij} response compared. For this comparison, the time fitter was used to provide the θ_{ij} distribution and the detector was modelled with all tubes operational. The results can been seen in figures 4.1 and 4.2. The NHITS distribution from the new cascade is only $\sim$0.35% lower than the old cascade (unfortunately it is not possible to determine

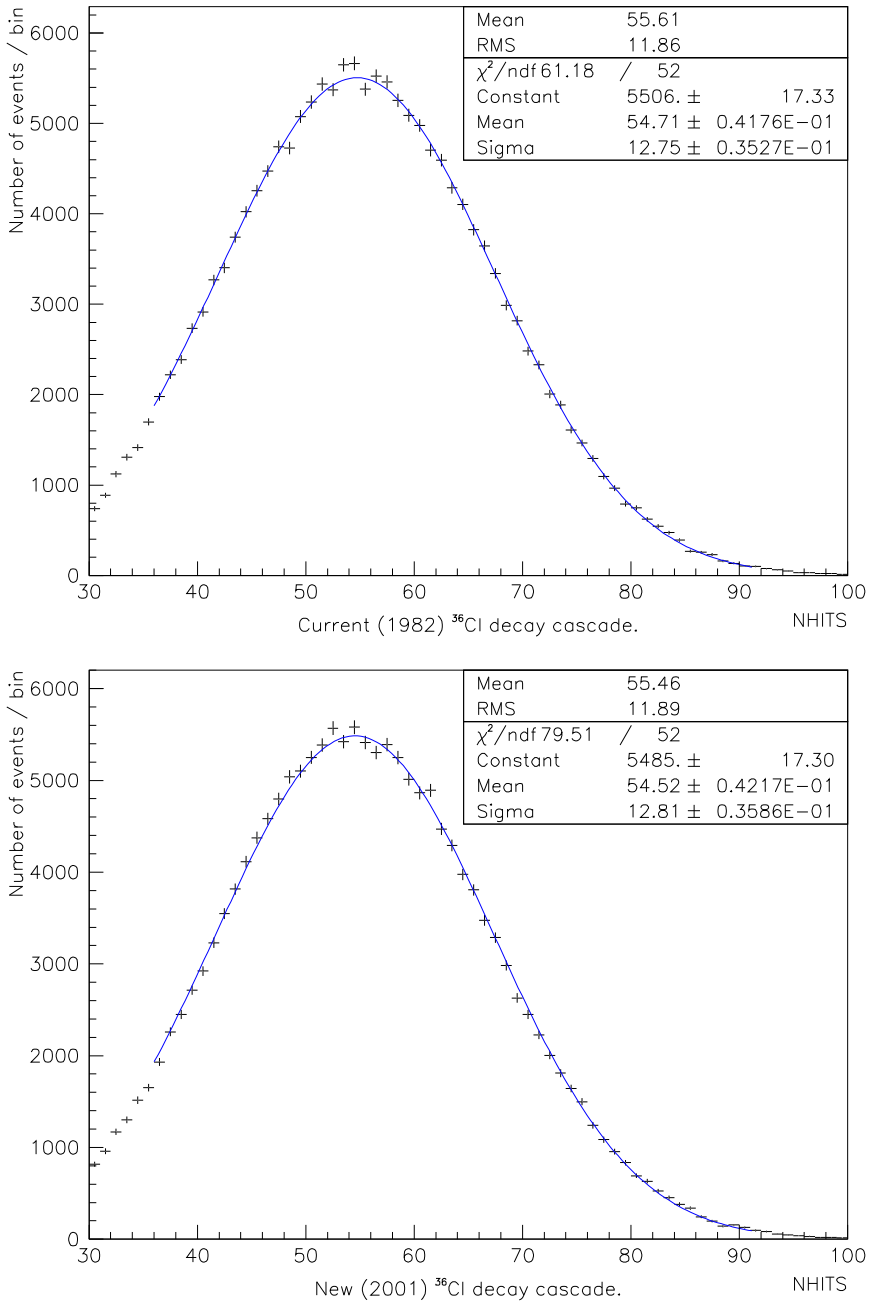

Figure 4.1: The NHITS distributions for the new and old ^{36}Cl decay cascades. The new cascade scheme gives a slightly lower NHITS distribution.

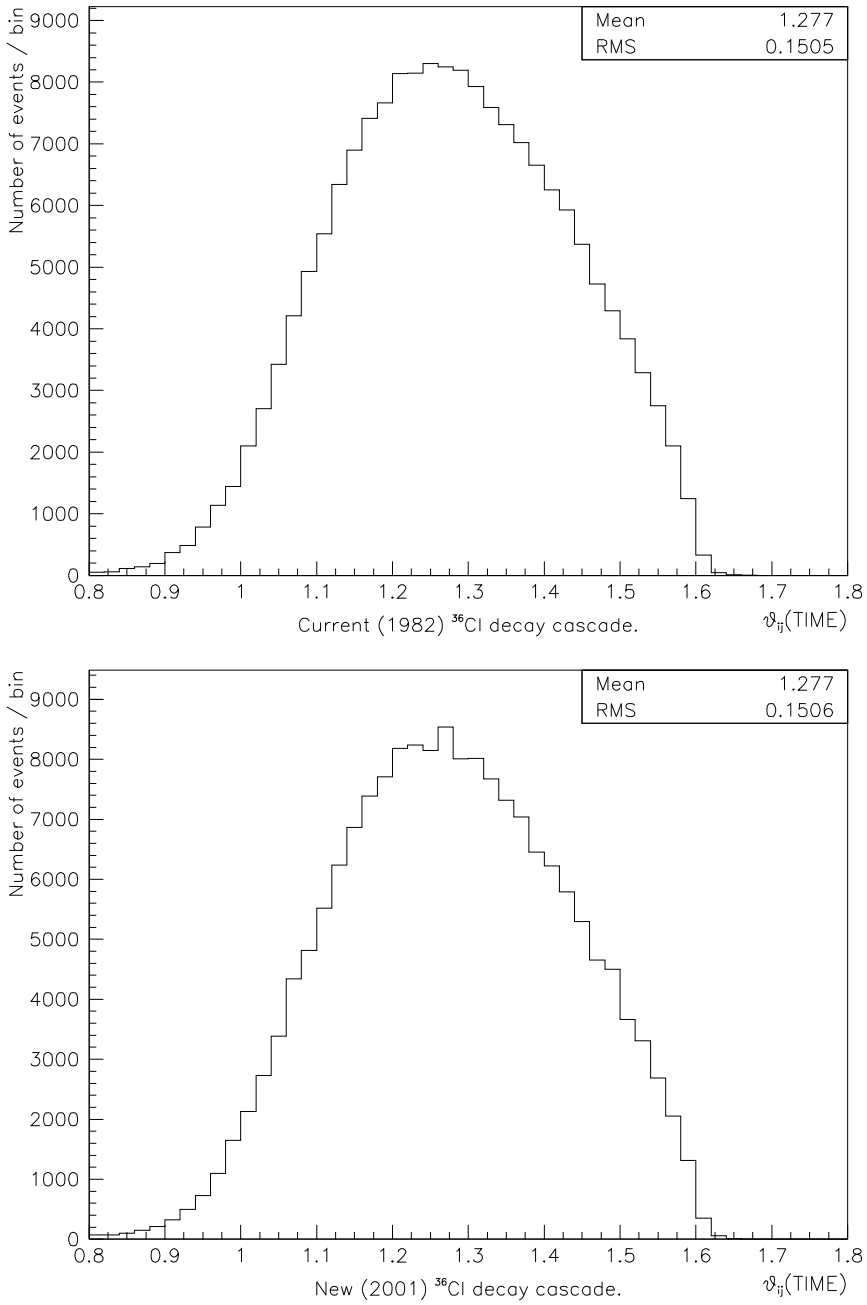

Figure 4.2: The θ_{ij} distributions for the new and old ^{36}Cl decay cascades. There is no significant difference between the cascade schemes.

which scheme describes the data better as other uncertainties dominate, see section 4.4.5). No significant difference in the θ_{ij} distributions of the two cascades is observed.

4.3 The ^{252}Cf Neutron Calibration Source

Neutron calibration sources containing ^{252}Cf have been made by encapsulating ^{252}Cf in small acrylic cylinders [57]. Neutrons are produced by this source when ^{252}Cf undergoes spontaneous fission. The neutron energy distribution is well described by a Maxwell-Boltzman distribution with a temperature of 1.42 MeV and the multiplicity is well known and detailed in table 4.1. The multiplicity distribution has been implemented in SNOMAN.

multiplicity	probability	multiplicity	probability
0	0.003±0.001	5	0.191±0.018
1	0.021±0.005	6	0.061±0.013
2	0.140±0.011	7	0.008±0.007
3	0.264±0.017	8	0.005±0.003
4	0.307±0.020		

Table 4.1: The ^{252}Cf neutron multiplicity distribution. Taken from [58].

Several sources have been made, but the one that will be discussed here is the high rate source. Its rate has been determined to be 17.45±0.3 neutrons sec^{-1} on June 12, 2001 using a ^{3}He proportional counter array [59].

4.3.1 ^{252}Cf Source Backgrounds

Unfortunately, several source induced backgrounds are present and must be taken into consideration when analysing data from this source. When a fission occurs, energy is released in the form of several (∼10) low energy (<1 MeV) γ-rays.

Run number	Source position			Length analysed
	x(cm)	y(cm)	z(cm)	
21019	1.1	-19.3	-517.1	28631 seconds
21023	-0.1	-21.3	2.5	39090 seconds

Table 4.2: Details of the two neutron source runs selected for analysis.

These γ-rays are coincident and can produce a low (<20) NHITS event that causes the detector to trigger. In addition, the fission fragments are unstable to β decay, and can have quite long half lives ($\sim$minutes). The resulting β particles and γ-rays can also trigger the detector, with the maximum β particle endpoint approximately 4 MeV. Lastly, neutrons from the source can capture in the source and deployment structure. The γ-rays from these (n,γ) captures should be simulated correctly (assuming that the captures are at thermal energies) but nevertheless these events represent another contaminant to the neutron signal. Little is known about the precise nature of the first two backgrounds, and no attempt is made to simulate them in SNOMAN.

For the runs used in the following analysis, the source was deployed with a 3.2 mm Dalrin (darkened polypropylene) light shield around it in an attempt to reduce the backgrounds.

4.4 Neutron Data Comparison

It is important that SNOMAN is able to simulate the transport of neutrons in the SNO detector and the response of the detector when a neutron capture occurs. It is also desirable to know how accurately SNOMAN can be used to predict the overall neutron capture efficiency.

4.4.1 ^{252}Cf Source Runs

Two neutron source runs were analysed, they are detailed in table 4.2. While by no means a complete survey of source positions in the D_2O, they do serve as a useful check that SNOMAN is able to simulate the transport of neutrons in the presence of salt. Indeed, as the neutrons random walk through the D_2O before they capture, these two runs can be used to study almost the full radius of the D_2O.

4.4.2 SNOMAN Configuration

Version 4.0191 of SNOMAN was used to generate the Monte Carlo data sets. For SNOMAN to accurately model the detector response, several parameters must be specified.

The optical parameters of the detector must be correct. While a detailed optical calibration of the detector has been made in the pure D_2O phase [60], the optical calibration for the salt phase is still underway. Because of this, the D_2O optical parameters were used.

The tube noise rate must be determined from pulse-GT events and then SNOMAN tuned to give agreement to the total light level detected. This is achieved by tuning the PMT collection efficiency. This is non-trivial as the total light response has been observed to drift downwards over time [61] and an accurate description of this drift has not yet be formulated for the period since salt was added to the D_2O. The cause of this drift is not known. Possible causes are optical variations in the AV (caused by exposure to water), PMT concentrator degradation, or biological growth in the detector.

The PMT collection efficiency was therefore set to 0.562, a value obtained by comparing the SNOMAN and data NHITS response of a previous central ^{16}N run.

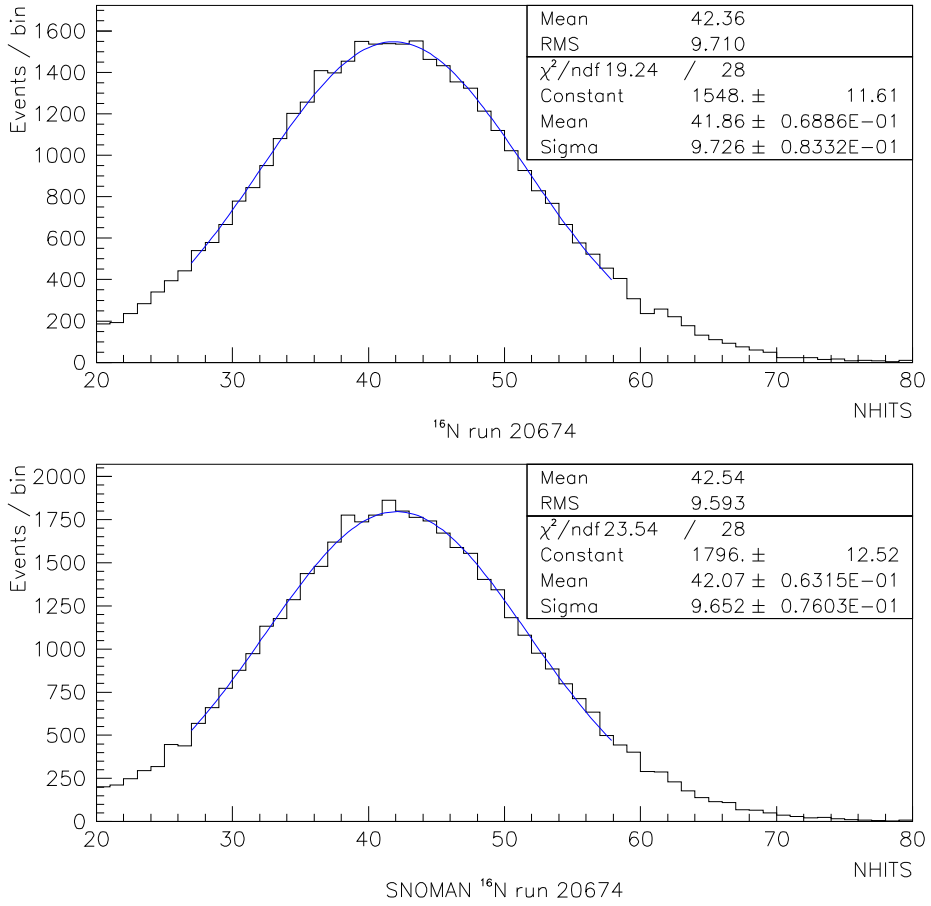

Figure 4.3: Agreement between SNOMAN and data for a central ^{16}N run taken 45 days prior to the neutron source deployment. The PMT collection efficiency used was 0.562.

The agreement is not exact, as shown in figure 4.3. This is because there was a small uncertainty in the number of functioning PMTs when the PMT collection efficiency was determined. When this uncertainty was removed, the SNOMAN NHITS distribution's fitted mean was found to be 0.5% higher than the data. As this is not a large difference, the SNOMAN mean NHITS can simply be scaled down by 0.5%.

This ^{16}N run was taken 45 days before the neutron source runs and so, accounting for the residual discrepancy in the ^{16}N NHITS distribution and estimating the drift at ∼2% per year [61], the NHITS distributions of the neutron Monte Carlos are estimated to be ∼0.75% higher.

The salt concentration used in SNOMAN was 0.2%. This was the target value, but during the salt injection practical considerations to ensure uniform density meant that the actual concentration achieved was lower than 0.2%. Measurements made with a salinity probe show the actual concentration to be ∼0.19% (a precision measurement, with error, is unavailable at this time to serve as an additional component in a blind analysis of the NC result from the salt data). As neutron transport within the D_2O is dominated by elastic scattering on deuterium and oxygen, the difference in salt concentration will have no observable effect on the radial profile of neutron captures. It will, however, have an affect on the number of neutrons that capture on chlorine, as shown in figure 4.4. The effect is small (∼0.5% less captures for 5% less salt). This is because the fraction of captures on salt is given by the ratio of the capture cross section on salt to the total capture cross section (all weighted by number of targets).

The effect on the capture time of the neutron is larger as this is determined by the total capture cross section (weighted by number of targets). As the chlorine cross section is dominant, a 5% decrease of the number of chlorine atoms corresponds to a ∼5% increase of the neutron capture time.

4.4.3 Data Selection

Candidate neutron events were selected using the following cuts:

- DAMN cuts: including muon follower long, excluding burst cuts (data only)
- Path fitter figure of merit cuts

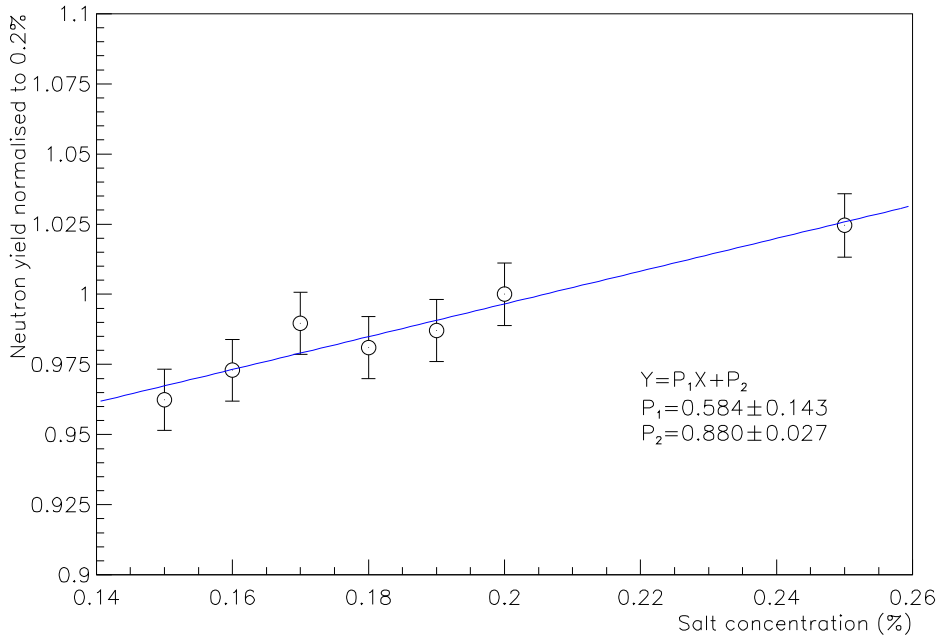

Figure 4.4: Neutron yield as a function of salt concentration, normalised to the yield with a salt concentration of 0.2%. The salt concentration in the D_2O is ~0.19% rather than 0.2%.

- $30 \leq \mathrm{NHITS} \leq 100$
- $\mathrm{R_{SOURCE}} \leq 200\,\mathrm{cm}$
- $\mathrm{ITR} \geq 0.55$
- $0.75 \leq \theta_{ij} \leq 1.65$

The DAMN cuts are chiefly responsible for removing instrumental backgrounds present during the operation of the neutron source, and a brief description of these cuts can be found in appendix C. The path fitter figure of merit cuts should be viewed as internal to the path fitter, though not applied by default. They reject bad fits, and have good rejection power for non-Čerenkov type events. See [36] for a complete discussion. The NHITS cut simply bounds the expected range of

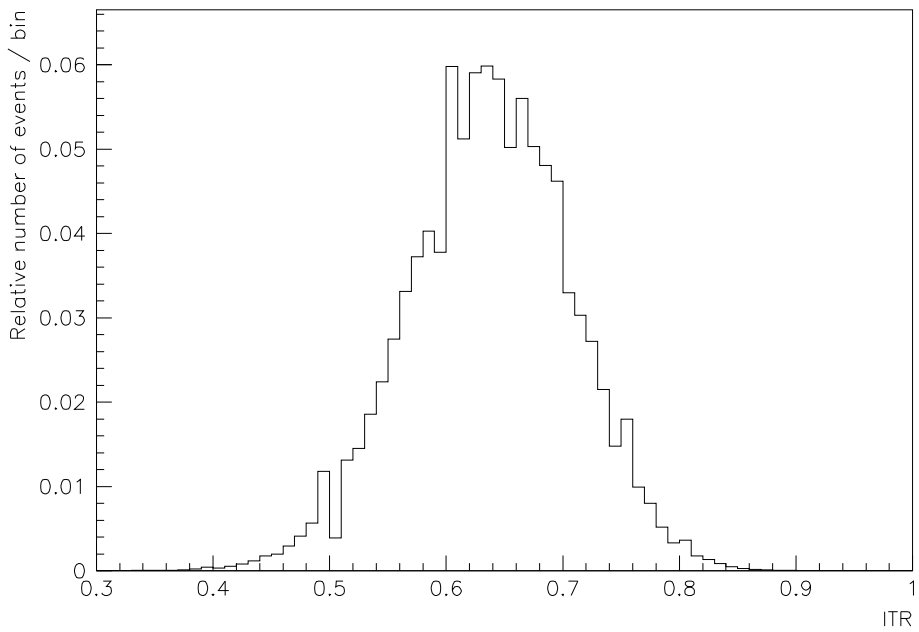

Figure 4.5: The ITR distribution of ^{36}Cl events. A cut is placed at ITR$\geq$0.55 to remove instrumental backgrounds and poorly reconstructed events in neutrino analysis and so is also used here.

NHITS given from neutron capture events, as can be seen from figure 4.1. The lower value ensures that data analysis is well away from the trigger threshold of the detector which is around 18 NHITS. The radial cut selects events from the expected location of the neutron captures, as can be seen in figures 4.6 and 4.7. The θ_{ij} cut bounds the θ_{ij} distribution from neutron capture events, as can be seen from figure 4.2. Finally, the ITR cut rejects instrumental events and poorly reconstructed Čerenkov events. The ITR distribution for neutron capture events in salt is shown in figure 4.5. The cut value of 0.55 is used as this is the value used in neutrino analysis.

However, these cuts will do little to reject the backgrounds produced by the source. To remove these backgrounds an additional cut of NHITS$\geq$60 or $R_{SOURCE}\geq$100 cm was used. These cuts were motivated by comparing the radial distributions of the data to those produced by the Monte Carlo. This was done by calculating the ratio of the number of Monte Carlo events to data events in 10 cm bins for different NHITS thresholds. The results are shown in the top plots of figures 4.6 and 4.7. The excess of events near the source is assumed to be the source background. Raising the NHITS cut to 60 allows most of the radial profile to be compared, whereas excluding the nearest 100 cm from the source allows the the full ($\geq$30) NHITS distribution to be examined.

4.4.4 Neutron Transport

The neutron transport capability of SNOMAN can be tested by comparing radial distributions and timing distributions.

Radial Distributions

The radial profile of events (distance from the source) is shown for run 21023 in figure 4.6 and for run 21019 in figure 4.7. A cut of NHITS$\geq$60 was applied and the Monte Carlo normalisation determined from a fit to the running normalisations between 50 cm and 200 cm from the source. The residuals are also shown, and for run 21019 (source positioned at the bottom of the D_2O) appear slightly worse than those for run 21023 (central). This is most likely due to a small error in the position of the source. Both residual distributions are consistent with a fit to a zero value straight line, the χ^2 per degree of freedom being 1.21 and 1.36 for runs 21023 and 21019 respectively. This demonstrates that the transport of neutrons, both in the centre of the D_2O and near the edge where capture on the AV is important, is well modelled by SNOMAN.

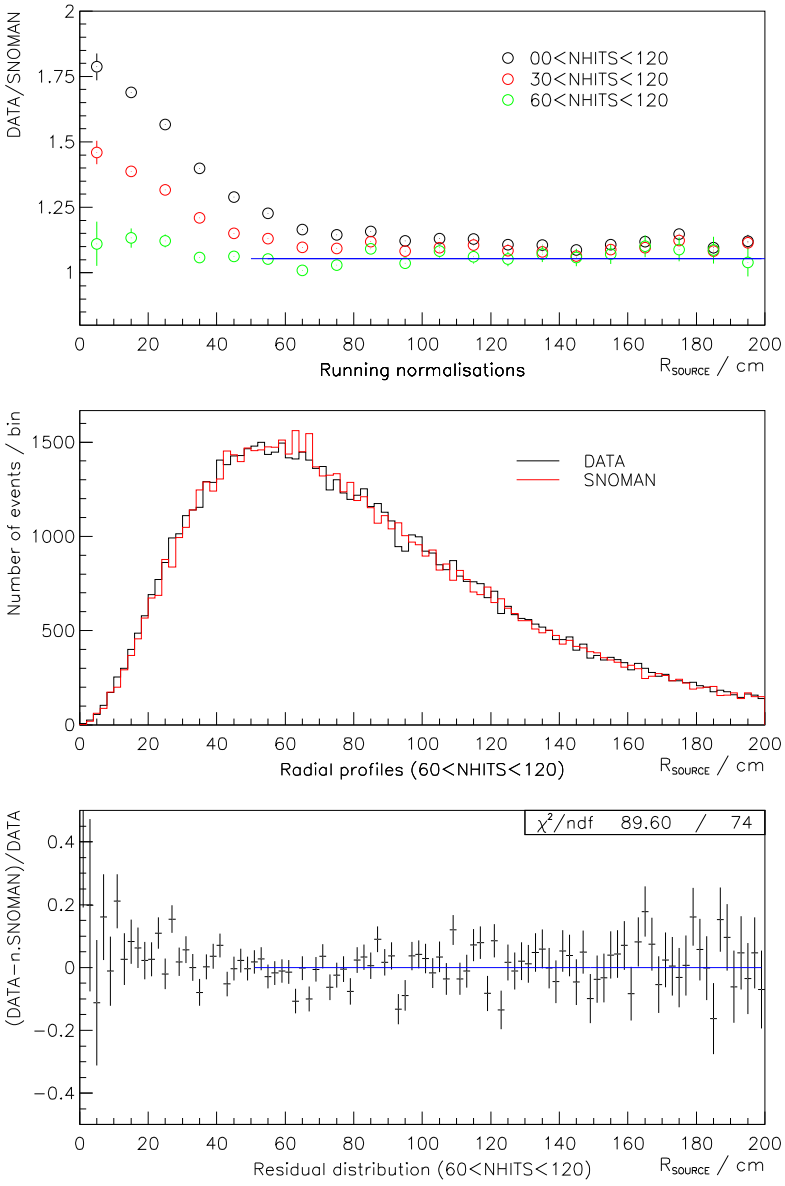

Figure 4.6: The radial distributions from run 21023 (central). Running normalisations [top] for 10 cm bins at different NHITS thresholds were used to determine the overall normalisation and where a radial cut should be applied to remove source related backgrounds when using a NHITS threshold of NHITS$\geq$30. Normalised radial distributions are shown [middle] as are the residual distributions [bottom]. The normalisation used is determined from the fit in the top plot. A fit to a zero value line is also shown.

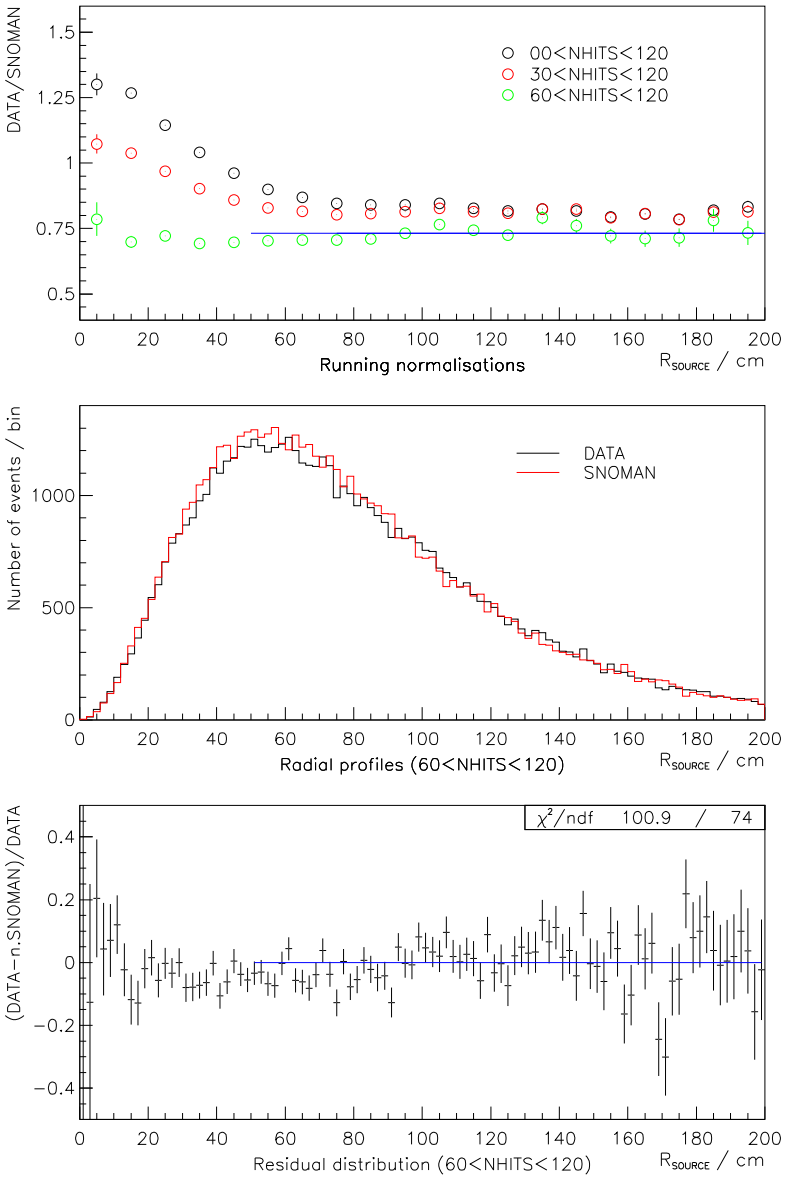

Figure 4.7: The radial distributions from run 21019 (bottom of D_2O). Running normalisations [top] for 10 cm bins at different NHITS thresholds were used to determine the overall normalisation and where a radial cut should be applied to remove source related backgrounds when using a NHITS threshold of NHITS$\geq$30. Normalised radial distributions are shown [middle] as are the residual distributions [bottom]. The normalisation used is determined from the fit in the top plot. A fit to a zero value line is also shown.

Neutron Capture Time

As the ^{252}Cf source emits neutrons in bursts, it is possible to extract the neutron capture time by considering the time between neutron captures. This was done by requiring 2 or more events (with NHITS$\geq$60) within 20 ms of each other. The time of the penultimate event in the burst was used to start a clock and the time of the final event in the burst used to stop it.

The resulting time distribution for run 21023 (data and Monte Carlo) is shown in figure 4.8. A fit was done to an exponential decay plus a flat component. This should correctly describe genuine neutrons captures and any backgrounds from the source which are not coincident with the fission (i.e. decays from long lived fission fragments). The fitted capture times are 5.35$\pm$0.16 ms for run 21023 and 5.32$\pm$0.15 ms for SNOMAN.

As mentioned earlier, the salt concentration used in SNOMAN was 0.2% rather than $\sim$0.19%. Thus the capture time from SNOMAN should be decreased by 5% for a fair comparison. This gives a capture time of 5.06$\pm$0.14 ms. This is in good agreement with the value obtained from the data.

4.4.5 Neutron Capture Response

The detector response to neutron capture on ^{35}Cl has two components: the total light produced and the hit pattern produced by that light. Each of these components is discussed below.

The NHITS Response

The NHITS response of the ^{36}Cl cascade is shown (for data and SNOMAN) for runs 21023 and 21019 in figures 4.9 and 4.10.

As mentioned above, the fitted mean of the SNOMAN NHITS distributions

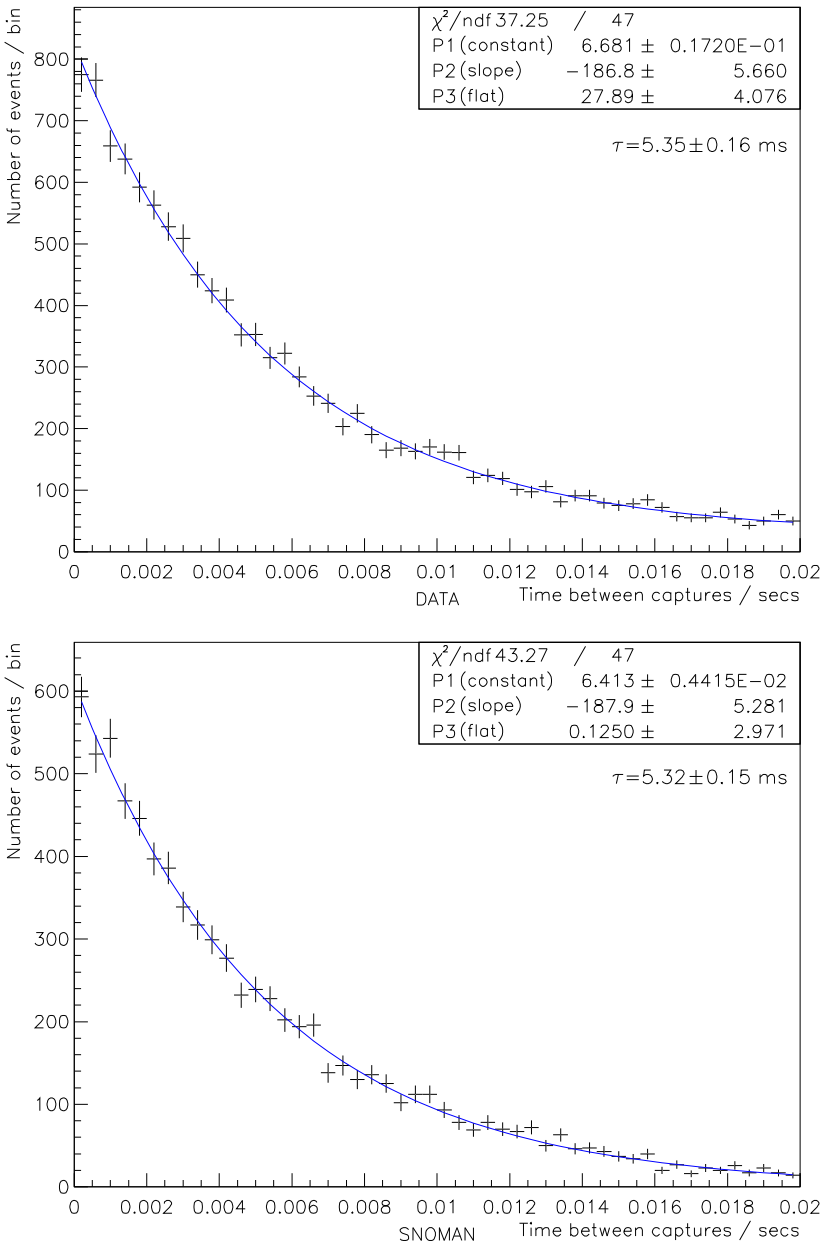

Figure 4.8: The distributions of the times between the penultimate and final events for bursts in run 21023. The data is fitted to an exponential decay plus a flat background. The decay constant gives the mean thermal neutron capture time. The flat background accounts for source related backgrounds from long lived fission fragments.

are expected to be ∼0.75% higher than those for the data. After applying this correction, the agreement for the central run (21023) is good, although slightly high. As was noted in section 4.2.3, the new ^{36}Cl decay scheme has a slightly lower NHITS distribution. However, without more detailed knowledge of the drift it is impossible to comment on which decay scheme is more accurate.

The agreement with run 21019, which is at high radius, is not as good. After applying the correction to SNOMAN, the NHITS mean is still ∼1 NHITS higher. Figure 4.11 shows how the mean of the NHITS distribution varies with the reconstructed radial position of the event. This disagreement is likely caused by using the optical parameters determined in pure D_2O. Preliminary analyses have shown that the overall light levels in the detector dropped sharply by ∼4% after salt was added, indicating that attenuation in the D_2O increased. This hypothesis is entirely consistent with the NHITS disagreement observed here, and when the optical parameters for salt are determined this disagreement should be resolved.

The θ_{ij} Response

θ_{ij} is a parameter used to describe the hit pattern of an event. It is described in detail in appendix A.1. The θ_{ij} distributions (for data and SNOMAN) for runs 21023 and 21019 are shown in figures 4.12 and 4.13 respectively. The mean of the SNOMAN θ_{ij} distribution is ∼0.7% lower than the data for both runs. This has been observed with other sources, see section 7.2.5.

The dependence of the mean of the θ_{ij} distribution with reconstructed radial position is shown in figure 4.14. The ∼0.7% offset is clear, but the structure seen is reproduced well by SNOMAN.

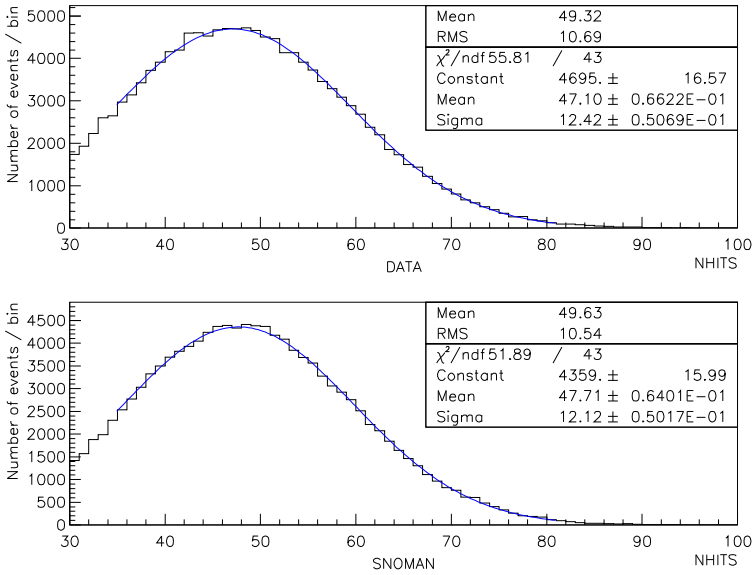

Figure 4.9: The NHITS distributions for events in run 21023 (central).

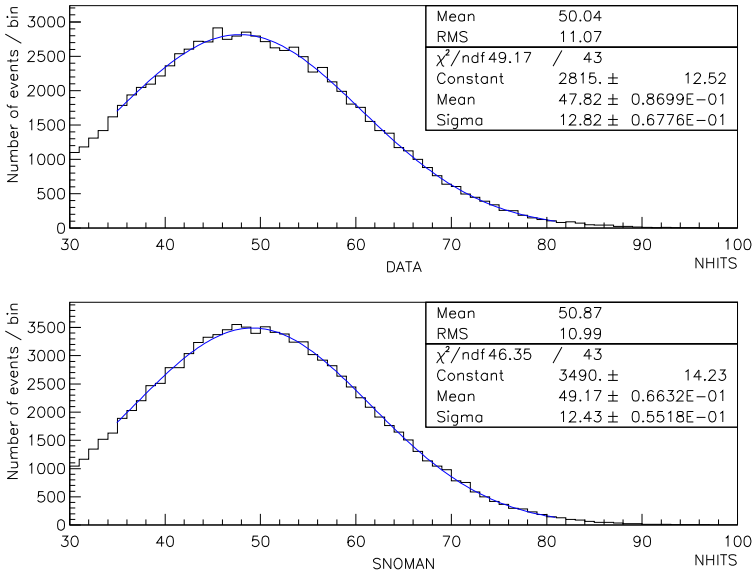

Figure 4.10: The NHITS distributions for events in run 21019 (bottom of D_2O).

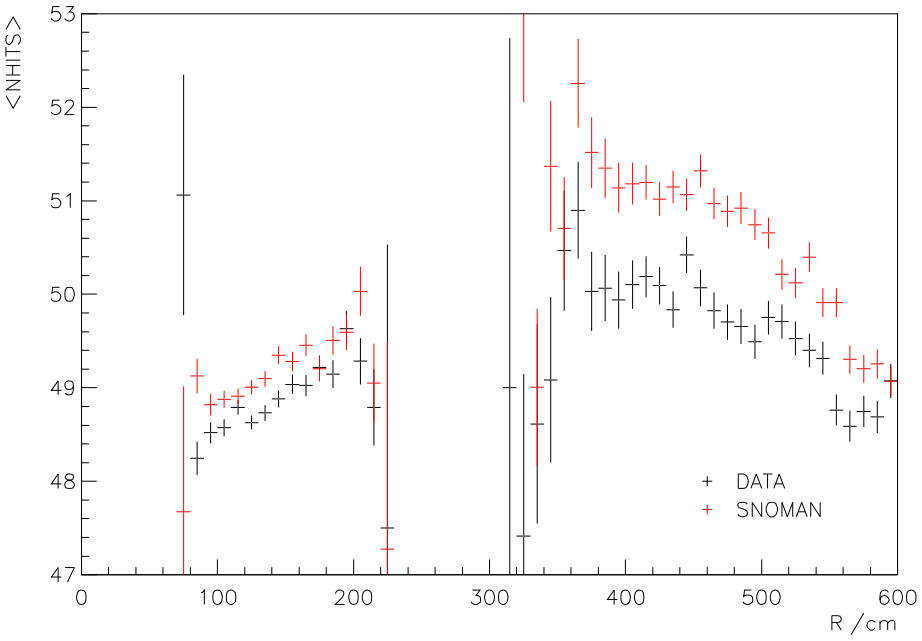

Figure 4.11: The dependence of the mean of the NHITS distribution with radial position. The SNOMAN values are expected to be about 0.75% high (see text). The differential radial dependence is almost certainly due to incorrect optical parameters in SNOMAN.

4.4.6 Neutron Detection Efficiency

The overall neutron detection efficiency can be determined for the data and for SNOMAN separately, and then compared. The efficiency was determined by counting the number of captures detected above a threshold of NHITS$\geq$60 and within 200 cm of the source, and dividing by the total number of neutrons produced. However, several corrections must be performed on the data and the Monte Carlo.

As the NHITS spectra are not matched exactly (and the widths differ) the gaussian fits were used to determine the fraction of events above a NHITS of 60 and the observed number of events corrected by this fraction. As the simulations

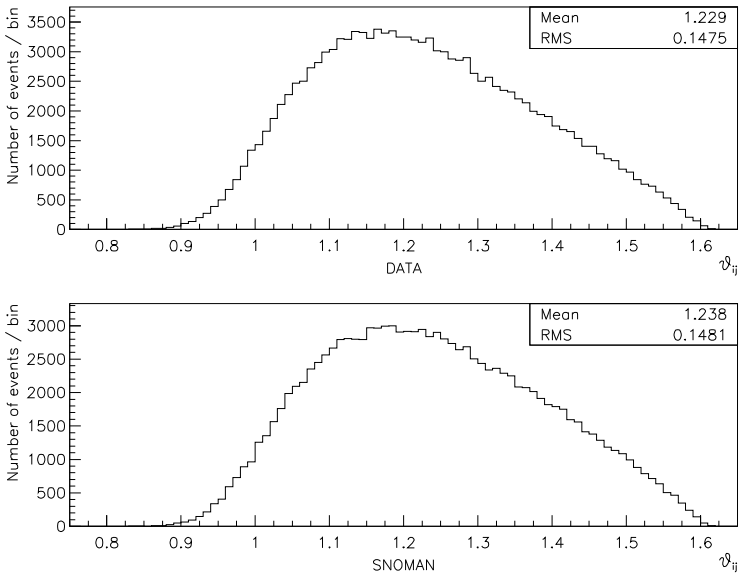

Figure 4.12: The θ_{ij} distributions for events in run 21023 (central).

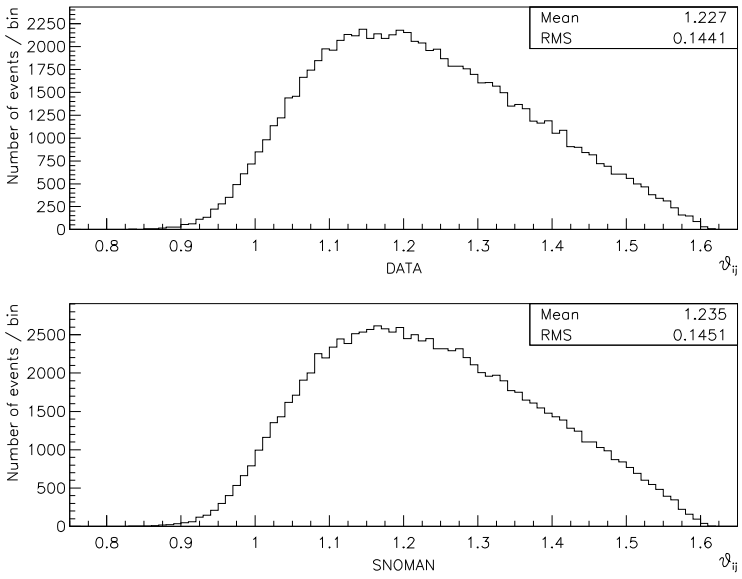

Figure 4.13: The θ_{ij} distributions for events in run 21019 (bottom of D_2O).

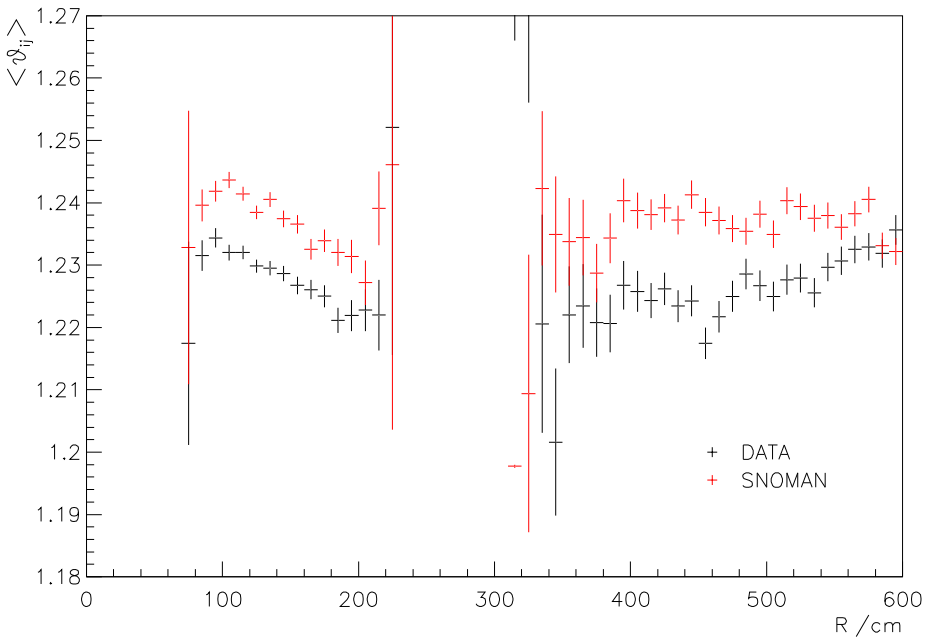

Figure 4.14: The dependence of the mean of the θ_{ij} distribution with radial position. The structure is reproduced well by SNOMAN, but there is a constant offset of ~0.7% (see text).

used a value of 0.2% salt, and the actual value is probably nearer 0.19%, the number of Monte Carlo events passing the cuts was decreased by 0.5% in accordance with figure 4.4.

The sacrifice of the DAMN cuts and the other high level cuts (fitter figure of merit cuts and ITR$\geq$0.55) should be accounted for, but precise measurements of these sacrifices have not yet been made. They will be omitted, except to note that the sacrifice for the real data is likely to be higher than that for Monte Carlo ($\approx$1% for data, $\approx$0.5% for Monte Carlo).

The neutron efficiency for captures with 200 cm of the source for each run is given in table 4.3, along with the SNOMAN predictions. Agreement is at the

Run	Efficiency (%)	
	Data	SNOMAN
21019	$78.6\pm0.3(stat.)\pm1.8(sys.)$	$78.8\pm0.3(stat.)\pm1.1(sys.)$
21023	$78.9\pm0.3(stat.)\pm1.6(sys.)$	$83.8\pm0.3(stat.)\pm1.0(sys.)$

Table 4.3: The estimated neutron efficiency for runs 21019 (bottom of the D_2O) and 21023 (central). The SNOMAN predictions are also shown.

5% level, introducing a 5% uncertainty on the neutron capture efficiency used in subsequent analyses.

4.5 Conclusions

Comparisons of the transport, response and overall capture efficiency for neutrons have been made between SNOMAN and the data during the salt phase. Although the absence of precision measurements of the optical constants, energy drift and sacrifice prohibits a very detailed study, this preliminary study shows that the agreement observed is still very encouraging, with no significant problems found. Neutron transport in particular, is in very good agreement.

SNOMAN has been shown to predict the neutron capture efficiency to $\approx$5%. This is likely to improve in future analyses, but for the moment a 5% uncertainty is assigned. This will be used in the analysis of ^{24}Na data in chapter 6.

Chapter 5

^{24}Na Production in the Recirculation Loop

In this chapter a Monte Carlo study to determine the rate of ^{24}Na production in the heavy water recirculation loop is presented. This study was largely responsible for the approval of the use of NaCl as the salt additive in the second phase of the SNO experiment.

5.1 Introduction

The use of NaCl salt, rather than $MgCl_2$ salt, to increase the NC signal in the second phase of the experiment was reconsidered when a source of NaCl with <5 ppm K[1] was found [62]. The important question is to determine at what rate ^{24}Na production occurs. If ^{24}Na production is not significant, NaCl is much preferred in terms of the cost of recovery, the manufacturing time required and the ease with which it can be assayed and purified.

The isotope ^{24}Na is produced by neutron capture on ^{23}Na and decays with a half life of 14.96 hours. This decay, which is detailed in figure 5.1, produces a 2.75 MeV γ-ray which can then photodisintegrate a deuteron atom in the detector,

[1]Required to prevent pileup of ^{40}K decays with other internal backgrounds.

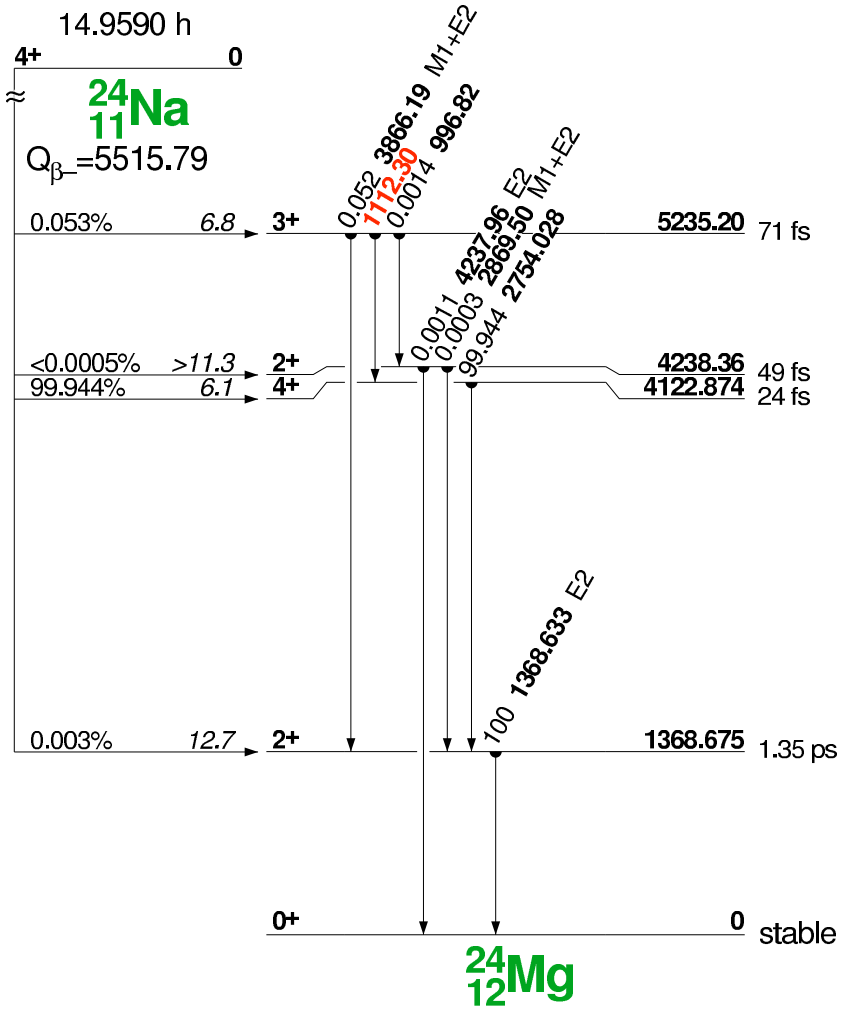

Figure 5.1: The ^{24}Na decay scheme. The 14.96 hour half lives gives ample time for ^{24}Na to be mobile in the water systems and the 2.75 MeV γ-ray can photodisintegrate deuteron atoms in the D_2O. A 2.75 MeV γ-ray is produced in almost 100% of decays. Courtesy of [63].

producing an irreducible NC background.

The detector cavity and underground laboratory were excavated from norite rock and lined with shotcrete. Both these materials contain trace quantities of uranium and thorium. These elements are unstable and produce γ-rays and neutrons (either directly, in the case of spontaneous fission of ^{238}U, or by emitting

α particles which then react via (α,n) reactions). Thus there is a flux of neutrons and γ-rays from the walls throughout the detector cavity and underground laboratory. The detector itself has adequate shielding from these fluxes but the recirculation system does not. ^{24}Na can therefore be produced in the recirculation loop by two mechanisms: direct neutron capture of a wall neutron, or capture of a neutron produced by a wall γ-ray photodisintegration of a deuteron atom in the recirculation system.

5.2 Monte Carlo Studies

Figure 5.2: Part of the SNO water systems. The feed/bleed tank can be seen (centre) and some of the recirculation pipes.

The recirculation system comprises, from the point of view of this study, of two elements: the pipes and the feed/bleed tank. These can be seen illustrated in

figure 5.2. There is approximately 140 m of pipe in the recirculation loop, most of which has an outer diameter of 8.94 cm and inner diameter of 7.32 cm. The majority of these pipes run parallel to the walls and the simulations performed modelled them as such. The feed/bleed tank, which is used to maintain the detector's heavy water level, is 192 cm high with an outer diameter of 122 cm. It is situated in the heavy water pit in the utility room. It is typically about half full (containing about 1 tonne of D_2O) and was modelled accordingly. Additionally, the tank was modelled to contain only half a tonne of D_2O. This is the minimum volume required for operation. Modelling was done by modifying the geometry information in SNOMAN.

5.2.1 γ-Ray Studies

The γ-ray spectrum from the wall has been modelled and measured [64]. It is dominated by the flux of 2.614 MeV γ-rays. To determine the effect of the 2.614 MeV γ-ray flux, three things are required: the magnitude of the flux, the photodisintegration fraction and the number of ^{24}Na per neutron generated. Each of these will be dealt with in turn.

The 2.614 MeV γ-ray flux has been measured to be $0.00746 \pm 0.0007\,\mathrm{cm^{-2}s^{-1}}$ [64]. These γ-rays are generated within the rock (from the decay of ^{208}Tl) and consequently the flux will be reasonably collimated perpendicular to the wall surface. The extent of this collimation was determined by generating 2.614 MeV γ-rays uniformly and isotropically within the rock. The angular distribution of 2.614 MeV γ-rays that exited the rock was recorded and used to determine the photodisintegration fraction in the pipe geometry. In addition to this, 2.614 MeV γ-rays were also started from within the pipe directed along the pipe axis. This was done to determine the maximum photodisintegration fraction and used in

estimating end effects (see section 5.3).

From these simulations the number of deuteron photodisintegrations per γ-ray was determined. The neutrons generated were then used to seed many more neutron events within the pipe. From this, the number of neutron captures on ^{23}Na per neutron generated was calculated. It should be noted that these neutrons are produced with an energy of $\sim$194 keV when a deuteron is photodisintegrated by a 2.614 MeV γ-ray.

A similar method was used for the feed/bleed tank. In the case of the tank, 2.614 MeV γ-rays were generated normal to all the walls surrounding the tank.

5.2.2 Neutron Studies

The energy spectrum of neutrons generated in norite from (α,n) reactions and spontaneous fission is coded in SNOMAN using information supplied by [65]. This spectrum was used to seed neutrons in the norite rock to determine the energy spectrum of the neutrons as they left the rock. Neutrons were then generated on the surface of the pipe and tank with this energy spectrum and isotropic inward direction. The thermal neutron flux measured by the NCDs is $4144.9\pm49.8\pm105.3\,\mathrm{m^{-2}d^{-1}}$ [66]. From this, the total neutron flux was estimated at $9000\,\mathrm{m^{-2}d^{-1}}$ [66] by modelling the amount of neutron thermalisation in the rock. The error on this number is expected to be comparable to the error on the measured thermal neutron flux. However, as this is merely speculation on the part of the author and this study must be conservative, the error is estimated at $\pm2000\,\mathrm{m^{-2}d^{-1}}$, roughly an order of magnitude larger than the thermal flux measurement.

Simulation	Photodisintegration fraction
Pipe (angular)	$7.3\pm1.4\times10^{-4}$
Pipe (axis)	$2.10\pm0.05\times10^{-3}$
Tank	$2.00\pm0.01\times10^{-3}$

Table 5.1: Photodisintegration fraction for 2.614 MeV γ-rays.

Simulation	^{24}Na per neutron
Pipe	$8.0\pm1.6\times10^{-6}$
Pipe (thermal)	$1.46\pm0.12\times10^{-4}$
Pipe (infinite)	$1.04\pm0.10\times10^{-4}$
Tank ($\frac{1}{2}$ tonne)	$1.342\pm0.037\times10^{-3}$
Tank (1 tonne)	$2.115\pm0.033\times10^{-3}$

Table 5.2: ^{24}Na production per neutron produced by photodisintegration.

5.3 Results

The photodisintegration fractions for 2.614 MeV γ-rays are shown in table 5.1. The ^{24}Na production per neutron generated by photodisintegration is shown in table 5.2 and the ^{24}Na production per neutron produced in the rock is shown in table 5.3.

Neutrons are produced in the wall with a range of energies, but almost 50% exit the wall with near thermal energies. These neutrons are more likely to capture on ^{23}Na in the pipe than neutrons produced at $\sim$194 keV by photodisintegration. This is the reason that the ^{24}Na production per neutron is higher for rock neutrons than photodisintegration neutrons in the pipe case.

For the feed/bleed tank the higher energy neutrons will thermalise so this effect is unimportant. However, the rock neutrons enter the tank on the surface whereas the neutrons produced by photodisintegration are distributed throughout the water. The rock neutrons are therefore more likely to escape the tank before capturing and the ^{24}Na production is correspondingly lower.

Simulation	^{24}Na per neutron
Pipe	$5.01 \pm 1.6 \times 10^{-5}$
Tank ($\frac{1}{2}$ tonne)	$4.41 \pm 0.66 \times 10^{-4}$
Tank (1 tonne)	$7.11 \pm 0.84 \times 10^{-4}$

Table 5.3: ^{24}Na production per neutron from the rock.

These results, together with the estimates of the fluxes involved, can be used to estimate the total ^{24}Na production rate. This is summarised in table 5.4. The rates shown for the two tanks simulations assume that the feed/bleed tank has an effective through flow of 1 litre/minute into the rapid flow of recirculating water (no additional piping or time delays). The raw rate for the pipes (in table 5.4)is the rate that the simulation estimates for 140 m of pipes running parallel to a wall, and the total rate is the anticipated rate after correcting for simplifications in the model. These are:

- End effects must be considered. The pipes run perpendicular to some walls and therefore the flux from these walls is directed along the pipe. The situation is not always this extreme, but if it is estimated that the effect is equivalent to 14 right angle bends in the pipe route, this gives a contribution to the γ-ray flux induced ^{24}Na/day rate of about 0.03 ^{24}Na/day. This is a rough estimate, but is very unlikely that the actual rate exceeds 0.3 ^{24}Na/day.

- The pipes run, for most of their route, in pairs closely parallel to one another and it is conceivable that neutrons escaping from one pipe may enter the other. If it is assumed that of the neutrons produced in the pipe, a quarter of them escape into the other pipe this produces an additional $\sim$0.4 ^{24}Na/day.

- Only the 2.614 MeV flux was considered. This is only a fraction of the

	^{24}Na/day			^{24}Na/day
	γ-ray flux	neutron flux	total	into detector
Pipe (raw)	1.54±0.55	18.0±7.0	20±8	20±8
Pipe (total)	4.5±2.0	18.0±7.0	22.5±9	22.5±9
Tank (1/2 tonne)	155±18	38±10	193±28	159±23
Tank (1 tonne)	366±34	62±16	428±50	294±35

Table 5.4: ^{24}Na production rates. The raw pipe rate is the value obtained from the simulations. The total rate is the anticipated rate after correcting for simplifications in the model.

total flux, albeit a large one. By considering the spectrum of the γ-rays emitted by the rock [64] and the energy dependence of the cross section for photodisintegration [56] a correction factor of $\times 2$ is estimated as a very conservative correction. This also affects the tank calculations.

Effects which decrease the rate have been ignored in the estimation of the rate as these should not be relied upon to reduce the rate. They are:

- Any effective shielding in the lab area. This is unlikely to be a big reduction except for the pipes that run above the detector.
- Smaller pipes are used in the utility room.
- The angular flux of γ-rays from the walls (for the pipe simulations) will have a cutoff due to the finite size of the walls. This will have two effects: it will reduce the total flux and it will decrease the effective path length of the γ-rays through the pipe.

The total ^{24}Na generated in the tank does not survive to the detector as the rate of flow through the tank is slow. To determine the fraction of ^{24}Na that survives, a litre packet of D_2O is considered flowing through the tank. The number of ^{24}Na atoms in this packet at a time t is given by:

$$\frac{dN}{dt} = R - \lambda N \tag{5.1}$$

which gives:

$$N = \frac{R(1 - e^{-\lambda t})}{\lambda} \tag{5.2}$$

Where R is the rate at which ^{24}Na production occurs for such a packet. It is assumed that the water entering the tank has no ^{24}Na and that each packet travels through the tank as though the tank were a pipe.

5.3.1 Reducing the Feed/Bleed Tank's Effect

The feed/bleed tank clearly contributes the most to the ^{24}Na production rate, even when running at minimum capacity. Rather than adopting a risky strategy of reducing the feed/bleed tank's operation, it may be more desirable to shield the tank with lead bricks: 5 cm of lead would reduce the effect of the γ-ray flux by an order of magnitude, thus 10 cm of lead shielding would reducing the γ-ray induced contribution to a comparable level to the pipes. To reduce the effect from wall neutrons, material with a high neutron capture cross section (such as boron) could be deployed surrounding the tank (outside the lead shielding).

Alternatively, the feed/bleed tank could be operated with pure D_2O [67]. The quality of this D_2O would degrade during operation, but modifications could be made to the water systems to minimise this effect.

5.4 Conclusions

The expected raw rate of neutron production, via the NC reaction, in the D_2O is ~4800 neutrons/year. One in ~380 2.75 MeV γ-rays photodisintegrates a deuteron. Therefore the addition of ^{24}Na would represent, in the most conservative case, an irreducible background of ~6% of the total signal. However, the effect of the feed/bleed tank can be largely eliminated by operating it with pure D_2O and constant recirculation of the D_2O is not required.

Chapter 6

Analysis of Activated ^{24}Na Data

This chapter discusses the use of ^{24}Na as a container-less source within the D_2O. The use of ^{24}Na as a container-less source was proposed by the author and others [68] and is the only container-less source that has been deployed in the detector to date. It has several key advantages over contained sources: there is no shadowing from deployment structures, no source induced backgrounds, and no source manufacturing defects which present simulation problems. It has been used to determine how accurately SNOMAN can model low energy events, crucial for the in-situ monitoring technique discussed in chapter 7.

6.1 Introduction

The addition of ~0.2% NaCl to the D_2O created the opportunity to generate ^{24}Na within the D_2O as a container-less source. ^{24}Na is a short lived isotope of Na ($T\frac{1}{2}$ = 14.96 hours) which decays via a $\beta\gamma$ decay ($Q_{\beta-}$=5.52 MeV, >99.9% by $E_{\beta-}$=1.39, E_γ=2.75+1.37 MeV) (see figure 5.1). This decay is similar to the $\beta\gamma$ decay of ^{208}Tl ($Q_{\beta-}$=4.99 MeV, 49% by $E_{\beta-}$=1.80, E_γ=2.61+0.58 MeV, 22% by $E_{\beta-}$=1.53, E_γ=2.61+0.86+0.58+0.28 MeV, and 25% by $E_{\beta-}$=1.29, E_γ=2.61+0.58+0.51 MeV). The $\beta\gamma$ decay of ^{214}Bi ($Q_{\beta-}$=3.27 MeV, 20% with $E_{\beta-}$=3.27 MeV, and ~50% with $E_{\beta-}$ >1.4 MeV) is less isotropic, but is in the

same NHITS regime. By establishing that SNOMAN can model ^{24}Na correctly, confidence can be gained in the ability to model ^{208}Tl and ^{214}Bi decays. Figure 6.1 shows a comparison of the ^{24}Na, ^{208}Tl and ^{214}Bi NHITS and θ_{ij} (see appendix A.1 for a description of θ_{ij}) distributions produced by SNOMAN.

6.2 Activation of ^{24}Na

^{24}Na is produced by neutron activation of ^{23}Na. The strongest source of neutrons that can be deployed in the D_2O, for an extended duration, is the superhot thorium source[1] which produces neutrons from deuteron photodisintegration. The superhot thorium source has an activity of $2.0\times10^7\pm5\%$ 2.614 MeV γ-rays per minute. Using SNOMAN it was determined that 1 in $456.28\pm4.8\%(stat.)\pm1\%(sys.)$ 2.614 MeV γ-rays photodisintegrates a deuteron. It was also determined that 1 in $72.96\pm2.7\%(stat.)\pm3\%(sys.)$ neutrons produced in this way would activate ^{23}Na. Both these estimates will slightly overestimate the actual production rates as the source geometry and manipulator were not taken into account. The superhot thorium source was deployed for 20.25 ± 0.5 hours at the centre of the detector. This gave $472514\pm8.4\%$ ^{24}Na atoms in the D_2O at the start of data taking.

6.3 Analysis of Activated ^{24}Na Data

Table 6.1 shows the runs following activation selected for analysis. SNOMAN was used to generate Monte Carlo data sets (full ^{24}Na; ^{24}Na with photodisintegration off; and a pure neutron sample) for each of these runs.

[1] The pT source [69] produces neutrons at a rate of approximately $2500\,s^{-1}$. However, this rate is not well known and long term deployment of the source (~24hours) is not possible.

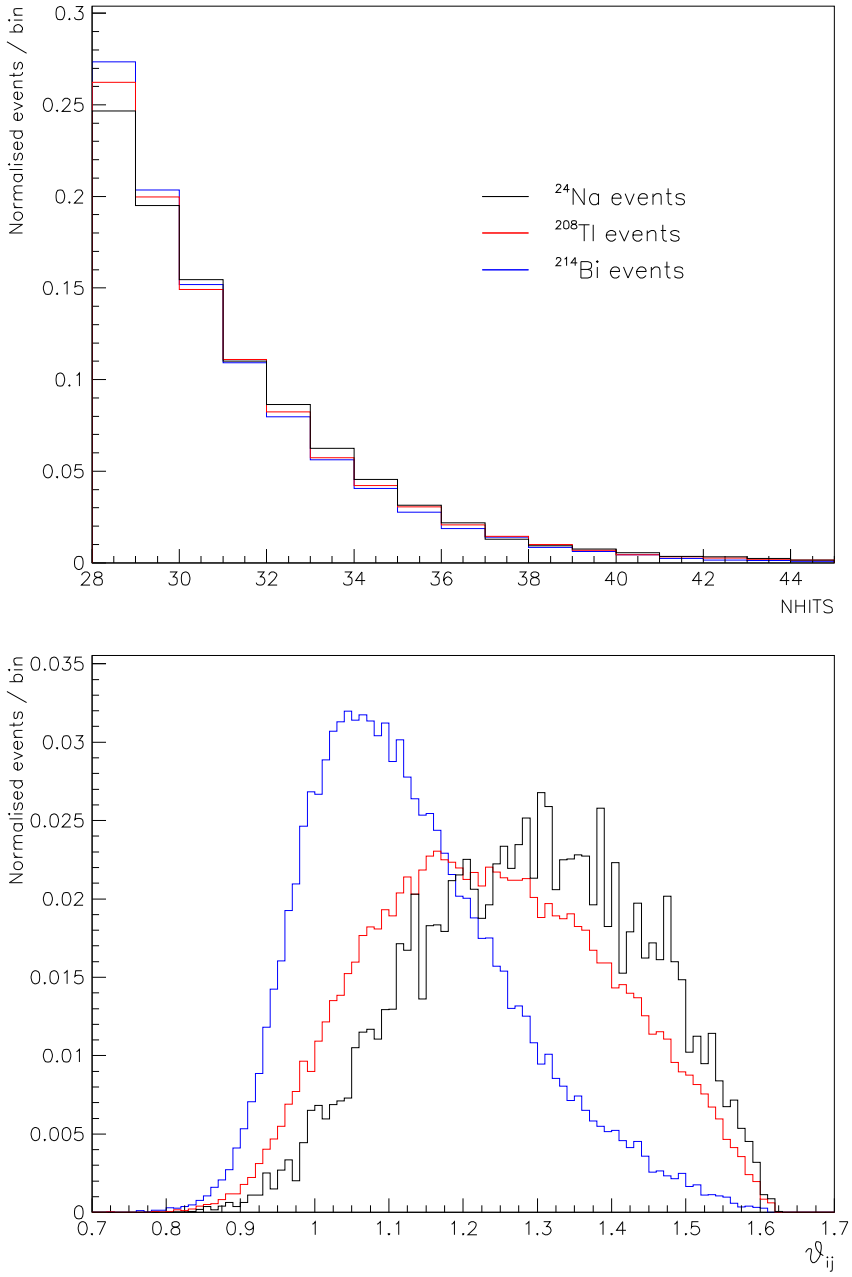

Figure 6.1: A comparison of ^{24}Na events and ^{208}Tl and ^{214}Bi events. The shape of the NHITS distribution is very similar. The isotropy of ^{24}Na events, characterised by θ_{ij}, is comparable with ^{208}Tl.

Run number	Duration (hh:mm)	^{24}Na MC events
20992	01:07	50420
20993	02:16	94670
20994	04:08	149000
20998	24:00	453680
20999	02:33	24780
21002	07:29	56130
21005	04:46	24790
TOTAL	46:19	853470

Table 6.1: Specification of the ^{24}Na runs used and the sizes of the Monte Carlo data sets generated.

6.3.1 Mixing in the D_2O

During the activation of the ^{24}Na and the subsequent data runs, the primary D_2O recirculation systems were inactive (but these systems are active for a few days every two weeks). Nevertheless, it is instructive to observe the amount of movement, if any, that the ^{24}Na underwent. Figures 6.2 and 6.3 show the spacial distributions in x, y, z and R for various time bins in the data taking. Each time bin is normalised to the same number of ^{24}Na decays, which increasingly overweights any background component. There is very little drift in the x and y directions, but some evidence for a drift in the z direction. This is possibly due to residual currents from the last time the recirculation systems were active, from the action of retracting the source or from convection currents within the vessel. No movement is modelled in the Monte Carlo.

6.3.2 Distribution Comparisons

A suite of cuts was used when performing comparisons between data and SNOMAN. These were:

- DAMN cuts

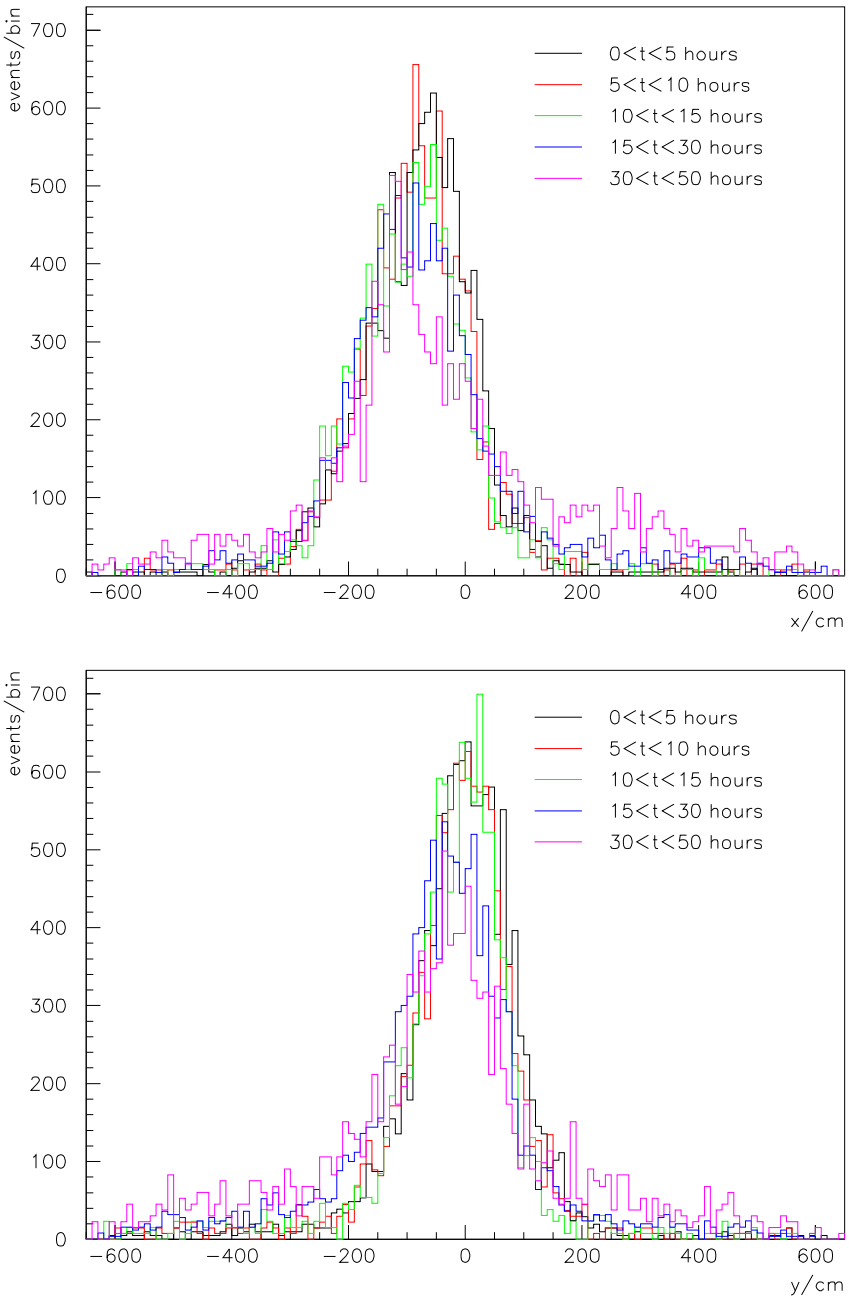

Figure 6.2: Fitted x and y distributions of ^{24}Na decays.

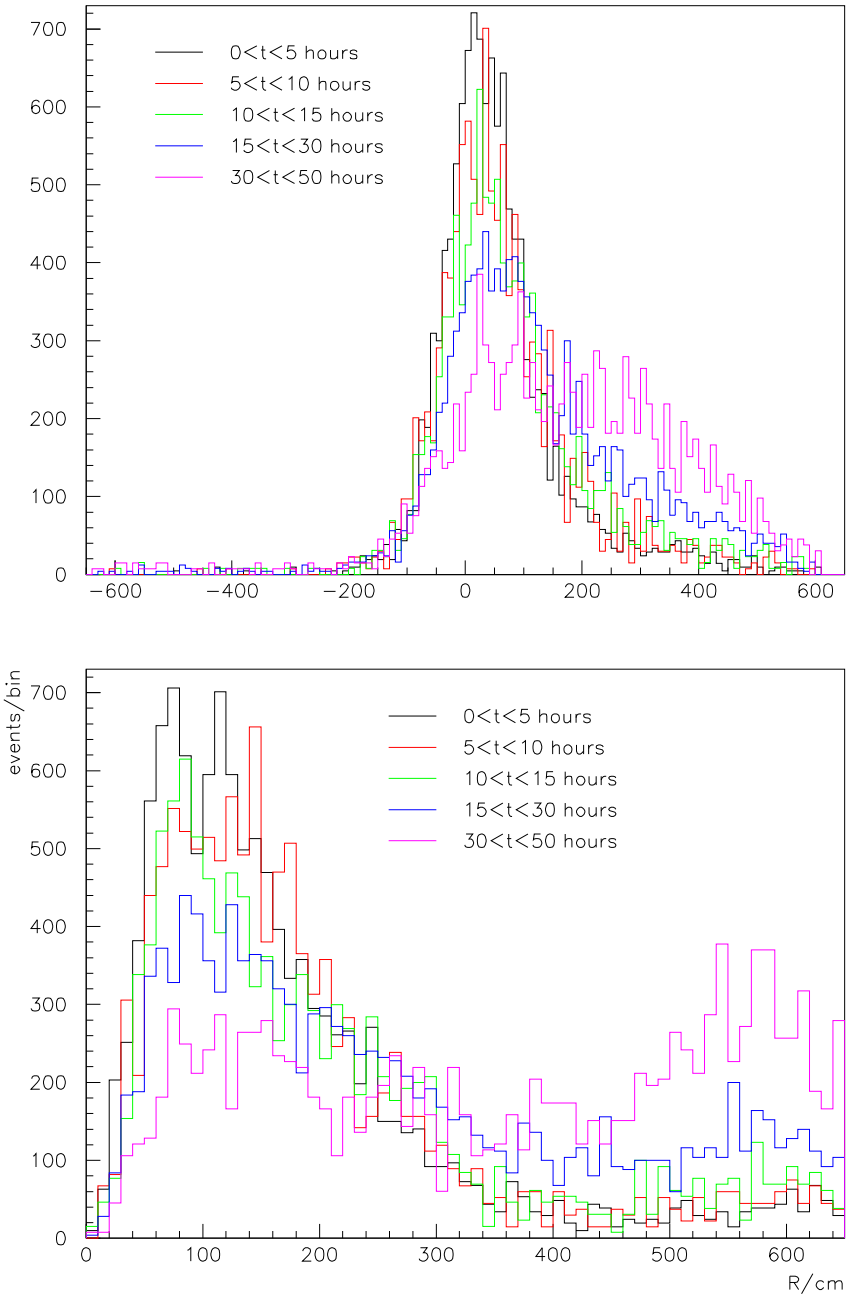

Figure 6.3: Fitted z and radial profiles of ^{24}Na decays. Background events (at high R) are increasingly overestimated due to the weighting.

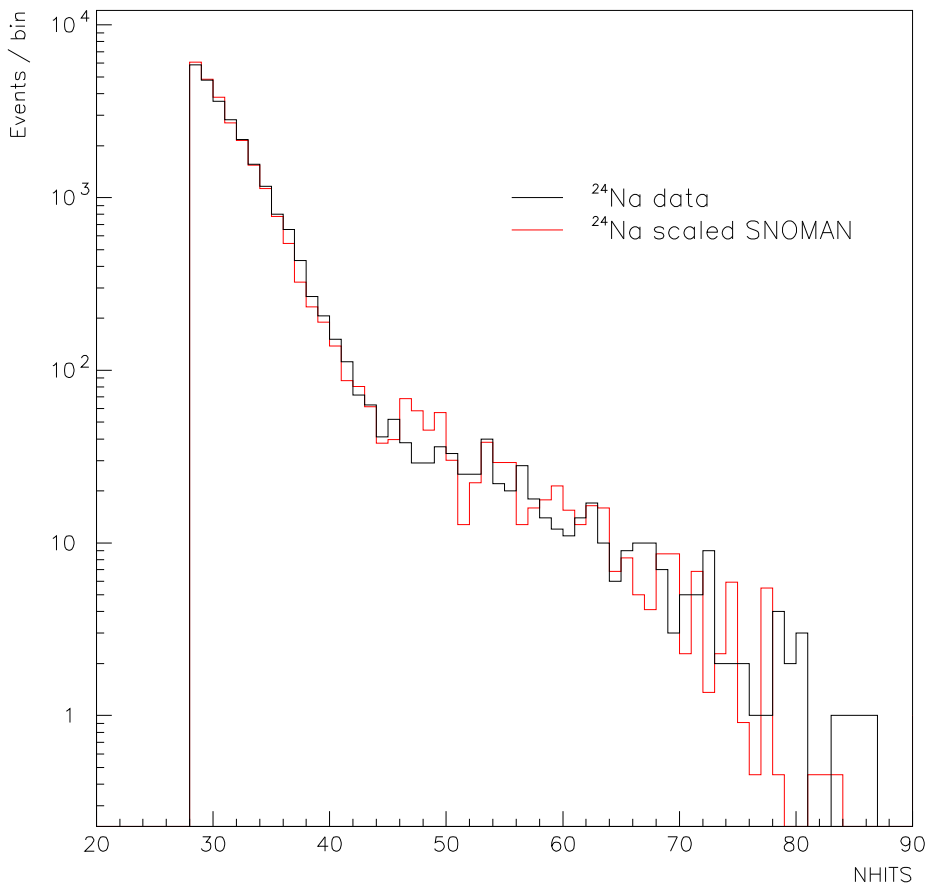

Figure 6.4: Comparison of data and SNOMAN NHITS distributions. (The NHITS cut was extended up to 90 NHITS).

- Path fitter figure of merit cuts
- 31≤NHITS≤40
- R_{PATH} ≤650cm
- ITR≥0.55
- $0.9 \leq \theta_{ij} \leq 1.65$

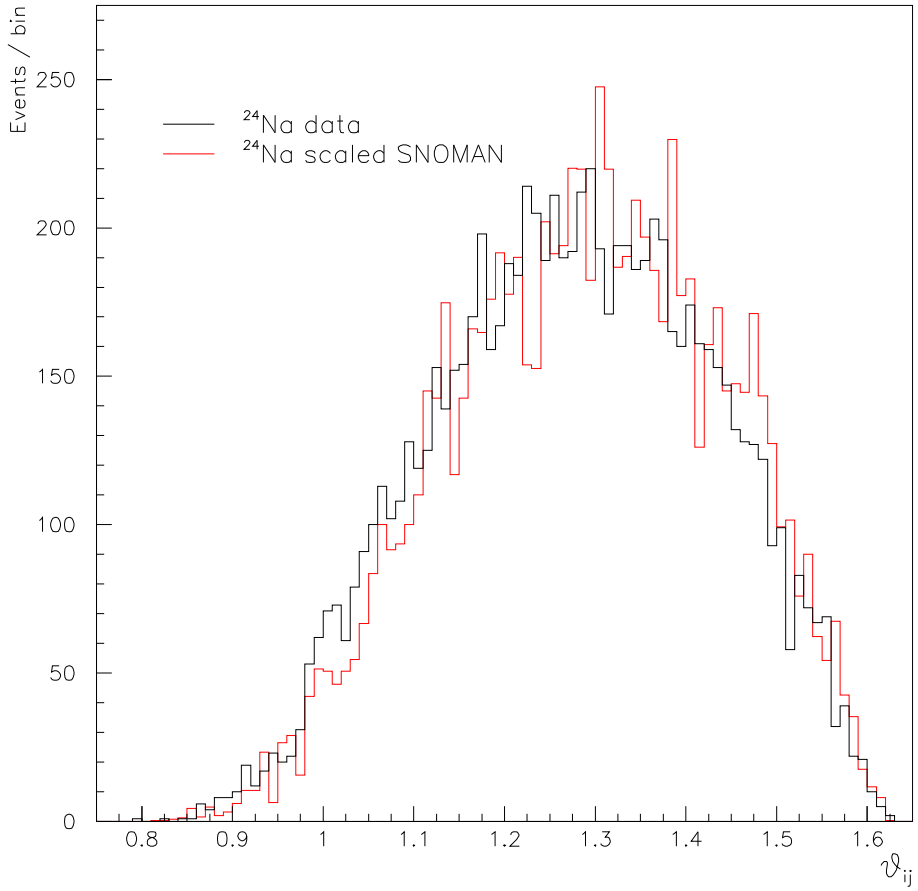

Figure 6.5: Comparison of data and SNOMAN θ_{ij} distributions. (An additional cut of $R \leq 450$cm was applied).

The NHITS distributions are shown in figure 6.4. There is reasonable agreement over the full range considered (which was extended to NHITS$\leq$90). In the low NHITS region, there is an indication that the SNOMAN distribution is falling slightly faster than the data.

The θ_{ij} distributions are shown in figure 6.5, for this plot a radial cut of $R \leq 450\,\mathrm{cm}$ was applied in addition to the above cuts. This cut focuses on the

regime of interest to the D_2O in-situ background technique and minimises any potential contamination from backgrounds or high R dependence of θ_{ij}. As was found with neutron (^{36}Cl) data, the SNOMAN mean of the θ_{ij} distribution is higher than the data. The shift is about $\sim$1.2%. This has been observed with other sources, see section 7.2.5.

6.3.3 DAMN Cut Sacrifice

The DAMN[2] cuts are used to remove the instrumental background (and tag muons) in the data [70]. The fraction of real events that are removed is known as the sacrifice and has been determined accurately with the ^{16}N source. However, as ^{24}Na events have a higher particle multiplicity than ^{16}N events, it is possible that their sacrifice could be different.

Despite being ill suited for an accurate sacrifice measurement, the ^{24}Na data can still be used to obtain an upper limit for the sacrifice. This is achieved by firstly preparing a reliable high purity sample of ^{24}Na events without using the DAMN cuts targeted at intrumental backgrounds. The DAMN cuts under investigation can then be applied and the number of events that are removed used to estimate their sacrifice.

A sample of ^{24}Na events is obtained by first applying a partial DAMN mask (to remove very well understood backgrounds and incidental events, e.g. muon spallation events) and reconstructing all remaining events. Reconstruction not only allows event selection based on reconstructed position (events that reconstruct inside 400 cm are selected here) but also the application of high level cuts. The ITR (In Time Ratio, see appendix A.2 for details) cut is used, in an increasingly aggressive way, to remove remaining backgrounds. The results are shown

[2]Data Analysis Mask Numbers

Cut	Used in reduced mask	Cut	Used in reduced mask
Retrigger	Yes	ESUM	Yes
Burst	Yes	QCLUSTER	No
QvT	No	Muon tag	Yes
Q/NHIT	No	Muon follower short	Yes
Crate isotropy	No	In time channel	Yes
AMB	No	Flasher geometry	No
FTS	No	NHITS burst	Yes
OWL	Yes	OWL ESUM	Yes
JUNK	Yes	Zero zero	Yes
NECK	No	Salt blindness[3]	Yes

Table 6.2: The DAMN cuts under invesigation for the ^{24}Na sacrifice. Cuts in the reduced mask were used in conjection with high level cuts to prepare a pure ^{24}Na data sample.

in figure 6.6. The sacrifice is correlated with the ITR cut because of the timing information used in the DAMN cuts (particularly the fitterless timespread (FTS) cut). An upper limit for the sacrifice is therefore placed at 0.5±0.06%.

In addition to the instrumental sacrifice, the sacrifice from the total suite of aplied DAMN cuts can easily be estimated in a similar manner. This is just the inclusion of the sacrifice from the reduced mask, which is dominated by timing (burst) cuts. For the ^{24}Na data this sacrifice is 1.89±0.12%. The total DAMN cut sacrifice is estimated to be 2.4±0.13%.

6.3.4 Calculating the Cut Efficiency for ^{24}Na Events

The 2.75 MeV γ-ray emitted in a ^{24}Na $\beta\gamma$ decay can photodisintegrate deuterons in the D_2O. These neutrons capture predominantly on ^{35}Cl, and from the number of these events observed an estimate of the amount of ^{24}Na in the D_2O can be made. Neutron events, produced by SNOMAN, were used to determine the

[3]The salt blindness cut allows an unknown quantatity of neutrons from muon spallation through and is not applicable to the analysis of calibration data.

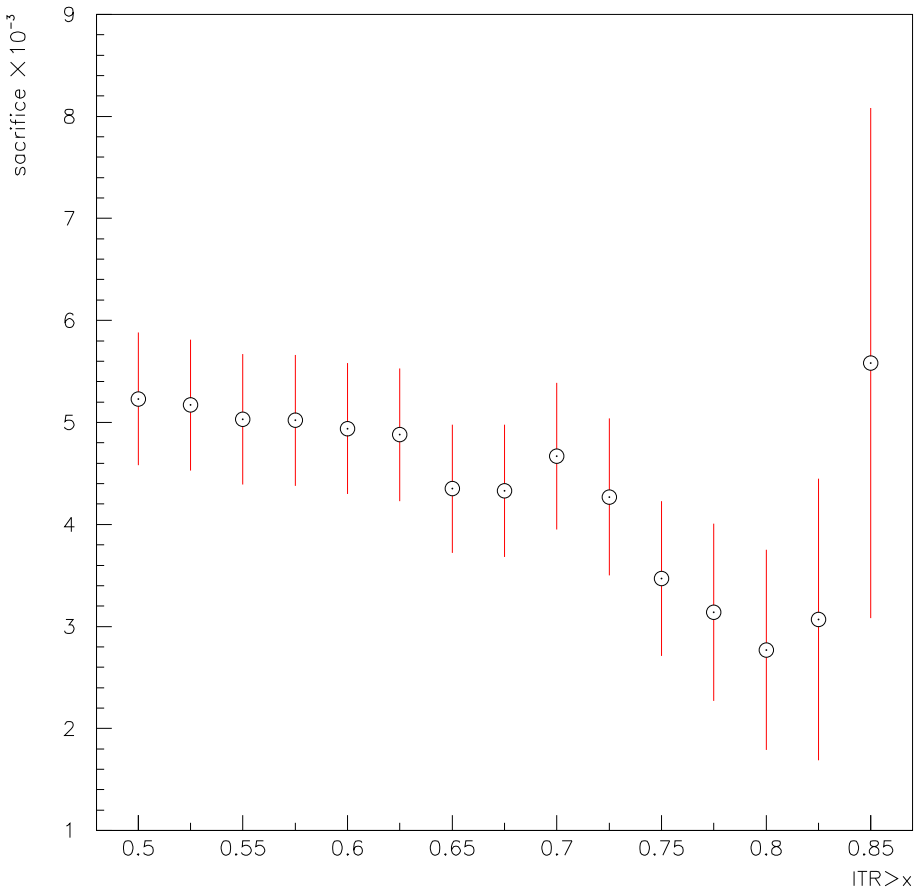

Figure 6.6: The ^{24}Na sacrifice as a function of the ITR cut used to prepare the data sample. Correlations between the sacrifice and applied ITR cut exist because some of the DAMN cuts use timing information.

relative amount of neutrons surviving any given NHITS cut. The ^{24}Na data set generated without photodisintegration were used to determine the relative amount of ^{24}Na decays surviving any given NHITS cut. The results are shown in table 6.3. Cutting at NHITS$\geq$50 should produce a pure neutron signal from which to estimate the amount of ^{24}Na.

By fitting the time dependence of the data to an exponential decay with a

NHITS range	Neutron fraction (%)	^{24}Na fraction (%)
30≤NHITS≤40	19.38±0.16	2.46±0.02
NHITS≥40	70.87±0.38	0.06±0.01
NHITS≥50	40.25±0.26	∼0

Table 6.3: ^{24}Na Monte Carlo breakdown. Photodisintegration was turned off in the data set used to determine the ^{24}Na fraction.

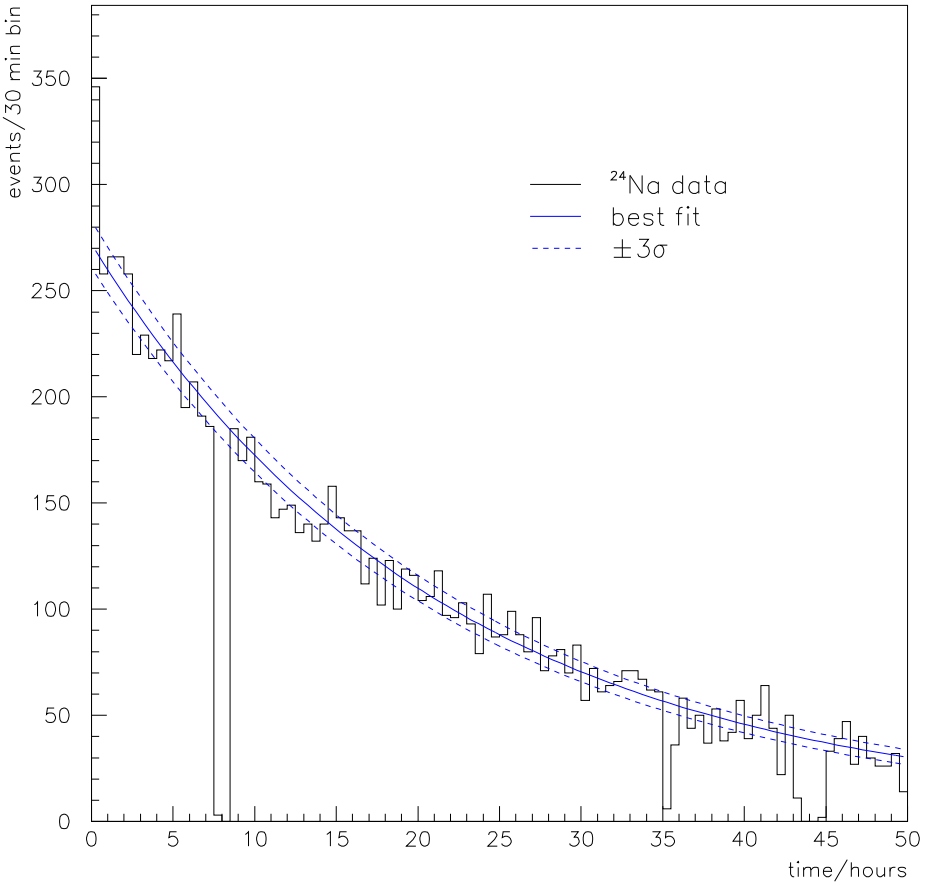

Figure 6.7: Likelihood fit to the ^{24}Na data. A half life of 14.96 hours was assumed in the fit. The bins with zero occupancy are due to detector deadtime (e.g. for maintance) and were not included in the fit.

Estimate method	Possible ^{24}Na	Observed ^{24}Na	Percentage observed
Source strength	403277±8.4%	10118±1.6%	2.51±0.21
Neutron yield	363511±8.6%	10118±1.6%	2.78±0.24
SNOMAN	853470	21348±0.7%	2.50±0.02

Table 6.4: ^{24}Na results. The errors shown are the statistical and systematic errors added in quadrature.

half life 14.96 hours and a flat background, it is possible to identify the amount ^{24}Na in the data. The results of such a fit can be seen in figure 6.7. This gave 9880.8±101.5 ^{24}Na decays and 346.2±84.4 background events in the data runs analysed. A similar fit with a NHITS threshold of NHITS≥50 gives the numbers of neutrons to be 329.4±19.7 with 46.6±17.1 background events.

The above results can be combined to give different estimates of the amount of ^{24}Na that was produced in the detector. From section 6.2, 472514±8.4% ^{24}Na atoms were estimated to have been produced. Because of the finite duration over which these decays were observed, the total number of events that could potentially be observed is 403277±8.4%. The number of neutrons, when corrected for the threshold acceptance and then multiplied by the number of 2.75 MeV γ-rays required to photodisintegrate a deuteron atom, gives 363511±8.6% of ^{24}Na decays that could be observed.

Given the number of observed events, the ratio of ^{24}Na events that pass the standard suite of cuts can be calculated. The results are shown in table 6.4.

6.4 Conclusions

SNOMAN reproduces the ^{24}Na $\beta\gamma$ decay well. The θ_{ij} distribution shows a slight discrepancy, with SNOMAN showing a ∼1.2% shift to higher θ_{ij}.

The ratio of observed events to total events, crucial to the D_2O in-situ analyses,

agrees to better than 10%. When the source strength is used to estimate the ^{24}Na produced in the detector, the agreement is better than 1%. The value of 10% is used in chapter 7 as the systematic uncertainty in the overall normalisation predicted by SNOMAN.

Chapter 7

D_2O In-Situ Measurement of ^{208}Tl and ^{214}Bi

The in-situ technique presented in this chapter was originally proposed by Martin Moorhead and pioneered with Monte Carlo studies by Xin Chen [71]. Work presented here refines the technique and applies it to the full pure D_2O data set from the first phase of the SNO experiment.

7.1 Introduction

As has been mentioned, the SNO experiment is sensitive to all active neutrino flavours. This is achieved by the NC interaction (see section 2.2.2) where the neutrino induces the breakup of a deuteron atom. The free neutron quickly thermalises in the D_2O and is subsequently detected by a (n,γ) capture or capture within a ^{3}He proportional counter (see section 2.3). Because the neutron is detected after thermalisation, very little information about the production of the neutron can be determined.[1] This loss of information means that any neutron produced within the SNO detector, irrespective of how, which captures in the

[1]The spatial distribution of the produced neutrons will determine the capture distribution and so, in principle, one should be able to differentiate different production distributions, e.g. neutrons produced by radioactivity in the AV.

Detector component	Thorium target	Uranium target
D_2O	3.7×10^{-15}g/g	4.5×10^{-14}g/g
H_2O	3.7×10^{-14}g/g	4.5×10^{-13}g/g
AV	2.5×10^{-13}g/g	3.0×10^{-12}g/g

Table 7.1: The target purity levels required for the SNO detector. The levels for the D_2O and AV correspond to $\sim$1 neutron produced per day for each chain for each isotope. The H_2O levels are set to reduce the high NHITS tail from $\beta\gamma$ events in the H_2O.

D_2O will contribute to the NC signal (obtained by signal extraction).

The SNO detector is very well shielded from neutrons from the rock by the H_2O volume. The only potentially significant source of neutrons is therefore the photodisintegration of deuteron atoms. Any γ-ray with an energy of more than 2.22 MeV can photodisintegrate a deuteron atom. γ-rays above this energy are present in the decay chains of both ^{232}Th and ^{238}U, as shown in figures 7.1 and 7.2.

Very low levels[2] of ^{232}Th and ^{238}U are found naturally in virtually everything. These low levels cannot be tolerated in SNO as the neutrons produced would overwhelm the NC signal. To reduce the potential background from photodisintegration, the SNO detector was designed with very stringent radio-purity targets; the key components are shown in table 7.1.

In the ^{232}Th chain, it is ^{208}Tl (which is produced 36% of the time) that decays with a γ-ray of sufficient energy. Every ^{208}Tl decay emits a 2.614 MeV γ-ray, making ^{208}Tl a very potent source of deuteron photodisintegrations. In the ^{238}U chain, it is predominately (>99%) decays of ^{214}Bi which produce high energy γ-rays. However, only $\sim$2% of all ^{214}Bi decays emit a γ-ray of sufficient energy. Thus considerably more ^{214}Bi can be tolerated in the D_2O than ^{208}Tl.

[2]Typically $\sim10^{-6}$g/g for solids, $\sim10^{-9}$g/g for water.

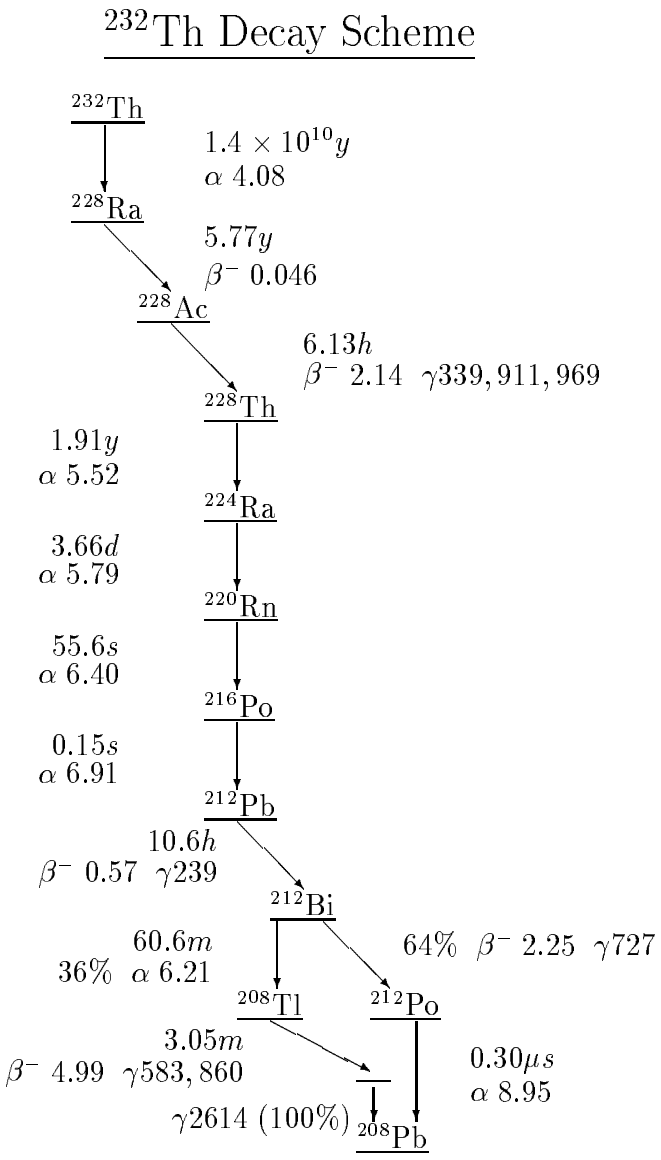

Figure 7.1: The ^{232}Th decay scheme. All half lives are shown, the the Q values of beta and alpha decays in MeV, and γ-rays in keV.

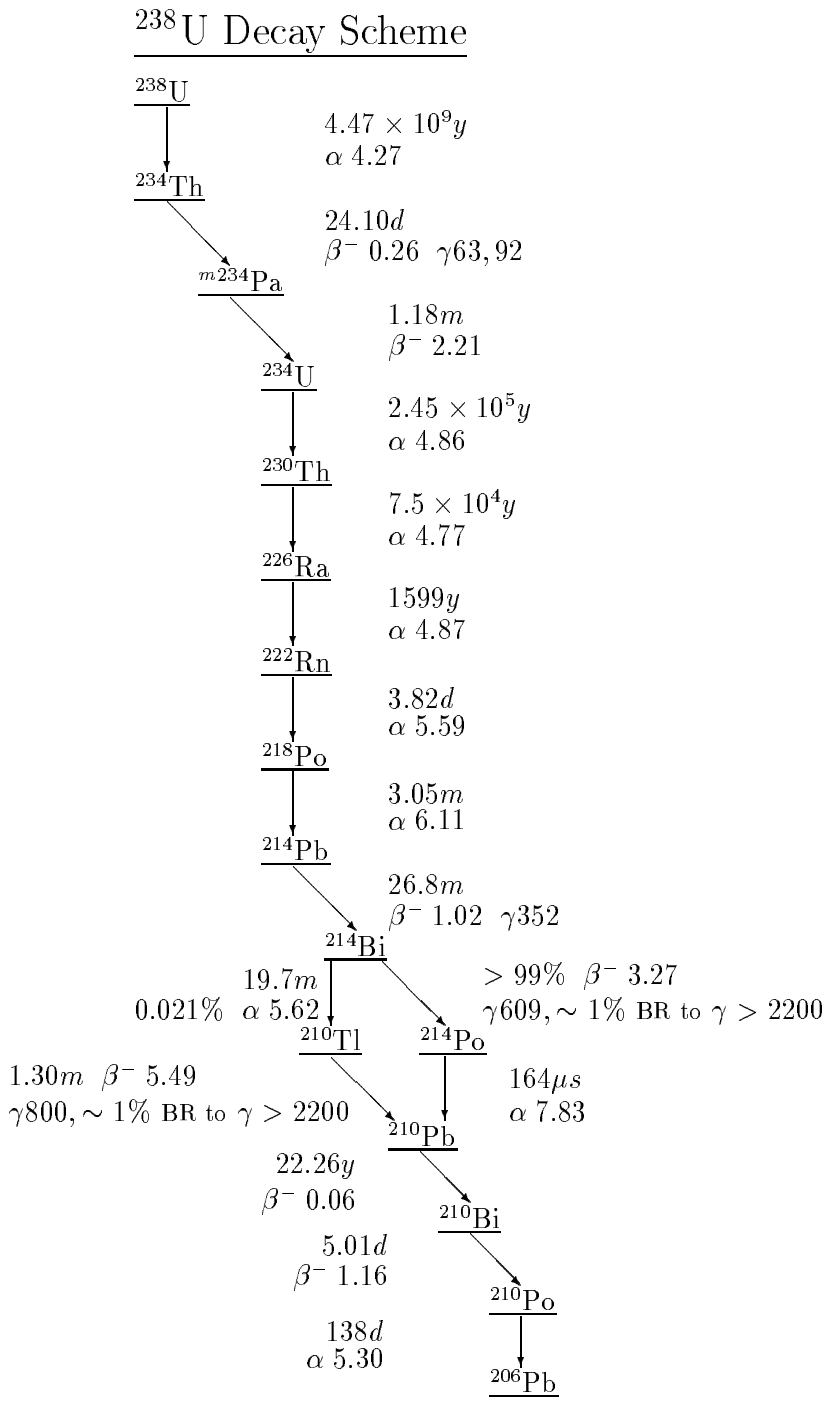

Figure 7.2: The ^{238}U decay scheme. All half lives are shown, the the Q values of beta and alpha decays in MeV, and γ-rays in keV.

The target purity levels for the D_2O and AV were set to limit neutron production in the D_2O to approximately 1 neutron per day per chain for the D_2O or AV (4 neutrons per day total, although a high fraction of the neutrons produced by the AV would escape the D_2O before capture). The H_2O target was not set to limit neutron production, which is expected to be negligible, but to limit the rate of $\beta\gamma$ decays and thus the background from the high NHITS tail of these events.

The expected neutron production rate (not detection rate, which depends on the analysis energy threshold) from the NC interaction is approximately 12 neutrons per day. It is therefore crucial to determine the levels of ^{232}Th and ^{238}U within the detector, particularly within the D_2O. If this cannot be achieved, the ability to measure the NC neutrino flux will be severely compromised.

There are two approaches which allow the determination of the levels of ^{232}Th and ^{238}U in the D_2O. The first is to assay the D_2O and count the radio-isotopes extracted ex-situ. Such techniques exist and were discussed in section 2.1.2. An entirely independent method is to use the SNO detector to observe the $\beta\gamma$ decays of ^{208}Tl and ^{214}Bi in-situ and from them infer the number of neutrons produced. This has several advantages over ex-situ techniques: it provides a continuous and non-invasive means to measure the background neutron production and makes no assumption that ^{232}Th and ^{238}U chains are in secular equilibrium.

That such an idea is possible is somewhat counter intuitive. Naively, the very low levels of ^{232}Th and ^{238}U and low rates usually discussed ($\sim$1 neutron per day) would seem to prohibit any realistic attempt. However, this neglects the very small photodisintegration cross sections involved and, for ^{214}Bi decays, the very small branching ratio to decays with γ-rays of sufficient energy. The actual numbers of ^{208}Tl and ^{214}Bi decays are much higher. The numbers of decays

required to produce a neutron has been calculated using SNOMAN:

$$\begin{aligned} 482.84 \pm 4.9(stat.) \pm 1\%(sys.)\ ^{208}\text{Tl decays/neutron} \\ 32051 \pm 907(stat.) \pm 1\%(sys.)\ ^{214}\text{Bi decays/neutron} \end{aligned} \tag{7.1}$$

where the 1% systematic error is from the fit to the photodisintegration cross section data.

Detection and identification of these decays is nevertheless difficult. This is because of very high levels of background from ^{208}Tl and ^{214}Bi decays in the AV, H_2O and PMTs. Overcoming this problem is achieved with a set of cuts which are discussed below.

7.2 The D_2O In-Situ Method

7.2.1 Overview

In principle the method is straight forward. Selected neutrino runs[3] are reconstructed and cuts are applied to reject backgrounds. The remaining data set contains both ^{208}Tl and ^{214}Bi events. As these have different neutron yields (see equation 7.1) the relative amounts of each are determined. Alternatively, the cuts can be tuned so that the cut efficiencies equalise the neutron yield. SNOMAN is used to generate Monte Carlo data sets of ^{208}Tl and ^{214}Bi events for determination of the cut efficiencies.

7.2.2 Cut Motivation and Specification

Before any cuts specific to the in-situ analysis are made, the standard suite of DAMN[4] cuts [70] are applied to the data to remove instrumental backgrounds and muons (including any muon spallation products).

[3]Neutrino runs are selected for official analysis by the run selection committee [70].
[4]Data Analysis Mask Numbers

The in-situ analysis cuts are designed to select D_2O $\beta\gamma$ events and remove external AV, H_2O and PMT $\beta\gamma$ events that misreconstruct inside the D_2O. Although the probability of misreconstruction is small, the PMT $\beta\gamma$ rate is approximately 20,000 times the D_2O $\beta\gamma$ rate. Unfortunately this is one of the few cases where SNOMAN cannot be used to generate event data sets because the light water optics and precise nature of the angular acceptance of the PMT concentrators are not known to sufficiently high accuracy. Even if they were, however, the point is largely academic as the CPU time required to generate a statistically significant sample of these events is prohibitively high.

Because of the lack of background Monte Carlo data sets, the cuts were tuned by comparing the resulting radial and directional distributions of the data with that of D_2O Monte Carlo data sets. A discussion of each cut is given below.

$31 \leq N_{eff} \leq 40$

The energy estimator used for the in-situ analysis is N_{eff}, which is a NHITS based estimator corrected for the detector noise rate and detector response drift. Details on this estimator can be found in appendix A.3. The cut on N_{eff} is two sided: the lower threshold discriminates against PMT $\beta\gamma$ events and the upper threshold against neutrinos.

PMT $\beta\gamma$ events have a lower N_{eff} distribution because the PMT concentrators used in SNO [72] have an angular cutoff at 56.4°. This effectively blinkers the tubes from light produced by nearby tubes.

Neutrinos are present in the data and although the neutrino rate is much lower than the D_2O $\beta\gamma$ rate, neutrinos represent a significant fraction of events after all the cuts have been applied. The N_{eff} spectrum for $\beta\gamma$ events is exponentially falling in this N_{eff} regime and above $N_{\mathit{eff}} \approx 40$, neutrinos dominate to the extent that there is little to be gained by raising the threshold further.

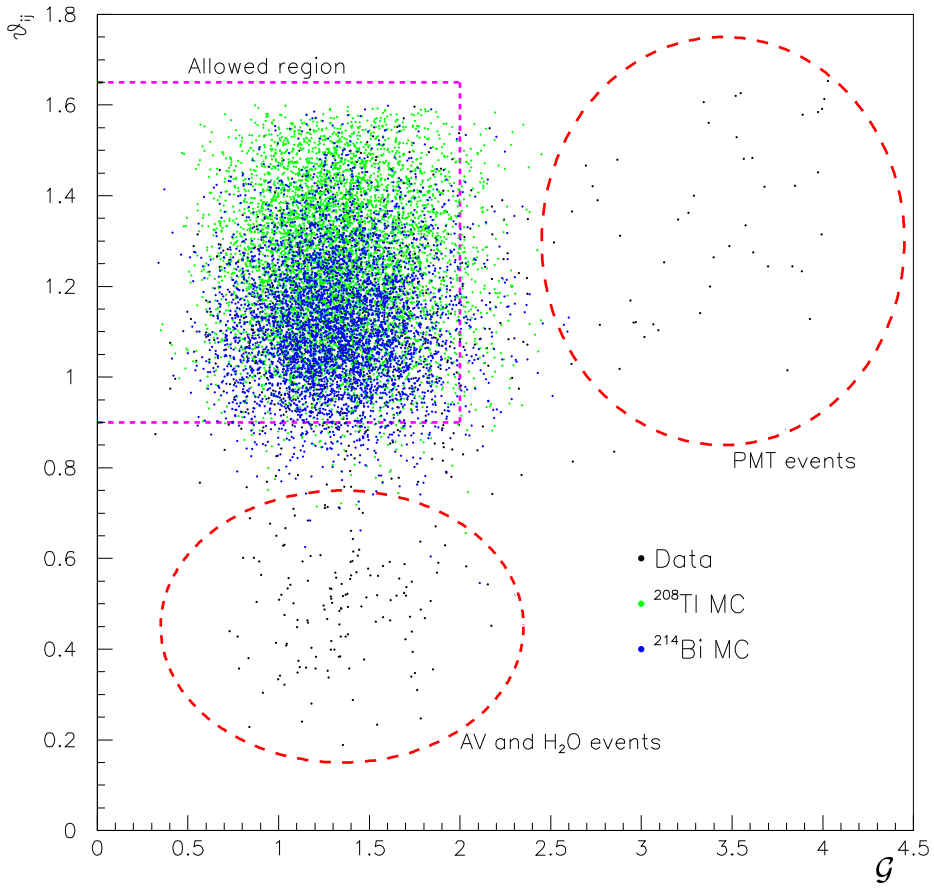

Figure 7.3: The θ_{ij} and $\mathcal{G}$ distributions for the data and ^{208}Tl and ^{214}Bi Monte Carlo data sets. A reconstruction cut of $R_{fit} \leq 450$ cm has been applied. PMT $\beta\gamma$ events have high $\mathcal{G}$ values and H_2O and AV $\beta\gamma$ events have low θ_{ij} values. Conservative cut values are used to ensure the remaining contamination is small.

$R_{fit} \leq 450$ cm

External $\beta\gamma$ events should be reconstructed outside the D_2O. Unfortunately, the reconstruction tails of these events extend into the D_2O. By restricting the analysis to a central D_2O volume, real D_2O $\beta\gamma$ events will be selected preferentially. By placing the cut at 450 cm, 42% of the D_2O is considered.

ITR$\geq$0.55 and $\mathcal{G}\leq$2.0

Two quality of fit measures are used to remove badly reconstructed events. The first, ITR (in time ratio), is simply the number of tubes which are in a prompt time coincidence window (further details can be found in appendix A.2). The second is a parameter returned by the fitter used (the grid fitter [47]):

$$\mathcal{G} = -2\ln(\mathcal{L})/nfit$$

where $\mathcal{L}$ is the likelihood of the fit and *nfit* is the number of PMTs used in the fit. It is a powerful discriminant of misreconstructed PMT $\beta\gamma$ events, as can be seen in figure 7.3.

0.9$\leq\theta_{ij}\leq$1.65

The θ_{ij} parameter is a measure of the isotropy of an event and is described in appendix A.1. The lower threshold of this cut is of most importance as it discriminates against AV and H_2O events which misreconstruct within the D_2O. These misreconstructed events (which tend to be physically outward in direction, presumably because this accentuates the problem of fitter degeneracy [73]) have a lower θ_{ij} because they have a fitted vertex further from the majority of PMT hits. The discrimination power of the θ_{ij} cut is shown in figures 7.3 and 7.4.

The upper threshold excludes any events with very high θ_{ij}. In practice this cut has very little effect as the only events with $\theta_{ij}>1.65$ are instrumental backgrounds and these should have been removed by the DAMN cuts.

7.2.3 Separation of ^{208}Tl and ^{214}Bi

The θ_{ij} parameter is used to separate ^{208}Tl events from ^{214}Bi events. ^{208}Tl $\beta\gamma$ events are more isotropic than ^{214}Bi $\beta\gamma$ events as they typically have a higher

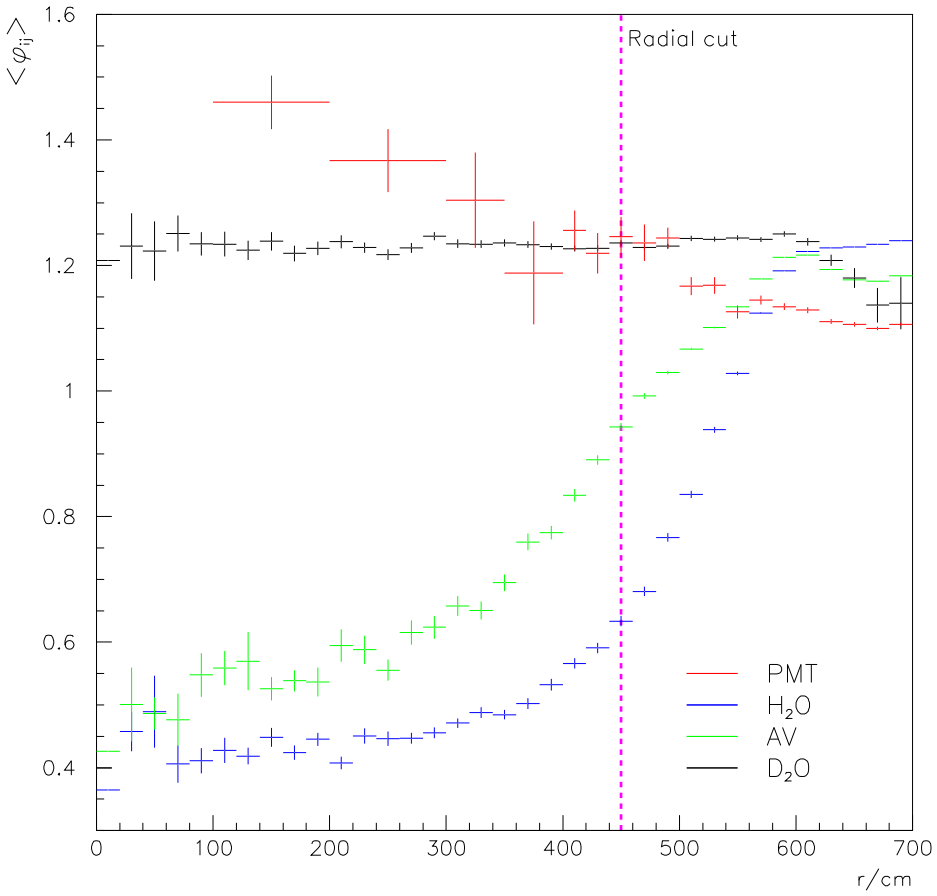

Figure 7.4: Mean θ_{ij} as a function of radius for Monte Carlo data sets of ^{208}Tl $\beta\gamma$ events from different detector regions. AV and H_2O events that misreconstruct far within the D_2O have a lower θ_{ij}.

number of low energy γ-rays in addition to the electron. The θ_{ij} distributions for these events are shown in figure 6.1.

Using SNOMAN, a ^{232}Th level of 1×10^{-15} g/g in the D_2O results in ~171 ^{208}Tl events in the in-situ monitoring window (~404 events in the whole D_2O). A ^{238}U level of 1×10^{-14} g/g in the D_2O results in ~933 ^{214}Bi events in the in-situ monitoring window (~2212 events in the whole D_2O). Therefore, the separation

Events generated		Events fitted	
^{208}Tl	^{214}Bi	^{208}Tl	^{214}Bi
0	1000	23±24	978±32
10	990	13±23	987±29
20	980	106±27	895±33
30	970	59±25	941±32
40	960	70±25	931±32
50	950	103±27	897±33
60	940	95±27	906±33
70	930	79±25	921±30
80	920	77±27	924±33
90	910	118±28	883±33
100	900	127±28	873±33
200	800	190±30	810±34
400	600	428±34	573±35
600	400	645±36	356±34

Table 7.2: Performance of θ_{ij} as a separation parameter of ^{208}Tl and ^{214}Bi events.

technique must be able to distinguish ^{208}Tl and ^{214}Bi events at this level.

Separation is performed using the extended likelihood method (see chapter 8) using PDFs generated by SNOMAN. The separation performance on Monte Carlo data sets has been studied and found to be adequate, as shown in table 7.2.

7.2.4 Equalising the Neutron Yield

The separation of ^{208}Tl and ^{214}Bi $\beta\gamma$ events can be avoided by tuning the cuts to give results for both ^{208}Tl and ^{214}Bi which are equal in terms of neutron production, rather than reflecting the number of decays. From equation 7.1 it can be seen that this requires a cut which accepts ~66 times as many ^{208}Tl events as ^{214}Bi events. Figure 7.5 shows how the neutron production ratio varies with the choice of the lower θ_{ij} cut threshold. As can be seen, a value of around $\theta_{ij}\approx1.395$ equalises the neutron yield. The uncertainty associated with this choice is addressed as a systematic error in section 7.4.

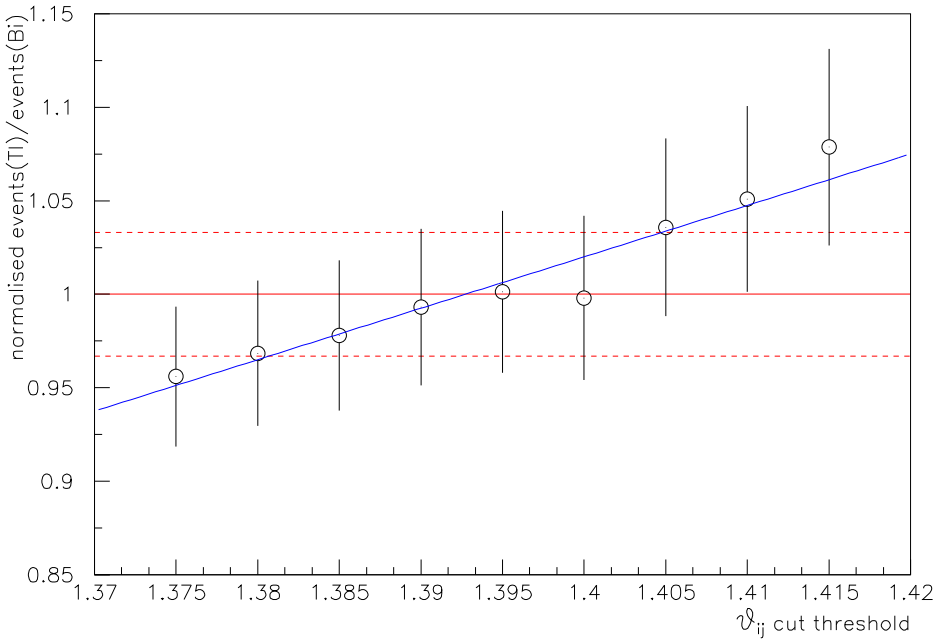

Figure 7.5: The ratio of ^{208}Tl and ^{214}Bi events, normalised to their neutron yields, as a function of the lower θ_{ij} cut value.

Unfortunately applying a cut of $\theta_{ij} \geq 1.395$ reduces the remaining statistics. However, this method provides a good check of the results obtained from the separation method.

7.2.5 Correction of the Monte Carlo θ_{ij} Distributions

As has been reported in chapters 4 and 6, there is a shift of about 1% in the mean value of the θ_{ij} distribution between data and SNOMAN. SNOMAN consistently predicts a higher θ_{ij} mean value than is observed in the data. The cause of this shift is unknown. Possible explanations are inadequate modelling of crosstalk in SNOMAN; differential fitter pull between SNOMAN and data; or incorrect scattering, probably on the AV.

The following correction, obtained using ^{16}N, neutron (^{36}Cl) and ^{24}Na data, is applied to the SNOMAN θ_{ij} distributions to artificially correct the shift:

$$\theta_{ij}{}' = \theta_{ij} \times 0.984 + 0.0085 \tag{7.2}$$

The remaining difference is addressed as a possible source of systematic error in section 7.4.

7.2.6 Neutrino Background Subtraction

As mentioned above, neutrinos are still present in the data after all the cuts have been applied (they account for ~18% of the events. Assuming no distortions in the ^{8}B energy spectrum and fluxes of 0.347, 1 and 0.459 SSM for the CC, NC and ES interactions respectively, the total number of neutrino events that fall within the monitoring window can be estimated using neutrino data sets generated by SNOMAN.

For the method in which the high θ_{ij} cut is used to equalise the cut yields in terms of produced neutrons, the total number of neutrino events can simply be subtracted. This is not the case when θ_{ij} is used to separate ^{208}Tl events from ^{214}Bi events: the relative contributions to ^{208}Tl and ^{214}Bi must be determined. This was done by passing the neutrino data sets, weighted accordingly, through the separation algorithm and subtracting the results.

One remaining concern is that the presence of the neutrinos will bias the fit. This can be investigated by comparing the results from the separation method with the results from the high θ_{ij} method.

7.3 In-Situ Results

Assuming that the ^{208}Tl and ^{214}Bi are uniformly distributed throughout the entire D_2O and that the decay chains are in secular equilibrium, the deduced background

levels are:

$$\begin{aligned} \text{Th} &: 1.75 \pm 0.40(stat.) \times 10^{-15}\,\text{g/g} \\ \text{U} &: 1.65 \pm 0.09(stat.) \times 10^{-14}\,\text{g/g} \end{aligned} \tag{7.3}$$

using θ_{ij} to separate ^{208}Tl and ^{214}Bi events. This gives a neutron production of:

$$\begin{aligned} \text{Th} &: 143.4 \pm 33.0(stat.)\,\text{neutrons} \\ \text{U} &: 173.5 \pm 10.9(stat.)\,\text{neutrons} \\ \text{Total} &: 317.0 \pm 34.8(stat.)\,\text{neutrons} \end{aligned} \tag{7.4}$$

in the D_2O, in the full D_2O data set. The statistical errors for the neutron production have been added in quadrature. This neglects the anti-correlation between these numbers. This is a small effect because of the different numbers of ^{208}Tl and ^{214}Bi decays required to produce a neutron (see equation 7.1). The method that employs a high θ_{ij} cut to equalise the neutron yield gives a neutron production of:

$$\text{Total} : 303.9 \pm 30.9(stat.)\,\text{neutrons} \tag{7.5}$$

This is in good agreement with the results obtained from the separation method and suggests that the separation is not being biased by the neutrino contamination.

7.3.1 N_{eff} Dependence

A breakdown of these results in N_{eff} is shown in table 7.3. The result obtained using a cut of $29 \leq N_{eff} \leq 31$ is also shown. All the results are statistically consistent, indicating that no significant background from external $\beta\gamma$ is present. The value of 31 as the lower N_{eff} threshold will therefore avoid any possible PMT $\beta\gamma$ events.

Table 7.3 also shows the inward and outward component for each N_{eff} bin. There is a slight indication that the lower N_{eff} bins have an excess of inward going events, which could be due to PMT $\beta\gamma$ events. This excess is not statistically

N_{eff} bin	Extracted ^{232}Th $\times 10^{-15}$g/g		Extracted ^{238}U $\times 10^{-14}$g/g	
$29 \leq N_{eff} \leq 31$	1.10±0.41		1.72±0.09	
$31 \leq N_{eff} \leq 33$	1.53±0.51		1.55±0.11	
$33 \leq N_{eff} \leq 36$	1.34±0.62		1.78±0.14	
$36 \leq N_{eff} \leq 40$	3.73±1.36		1.76±0.30	
$31 \leq N_{eff} \leq 40$	1.75±0.40		1.65±0.09	
	Inward	Outward	Inward	Outward
$29 \leq N_{eff} \leq 31$	1.44±0.59	0.87±0.53	1.82±0.12	1.59±0.11
$31 \leq N_{eff} \leq 33$	2.20±0.80	0.98±0.65	1.63±0.16	1.41±0.14
$33 \leq N_{eff} \leq 36$	1.40±0.84	1.47±0.86	1.72±0.20	1.80±0.20
$36 \leq N_{eff} \leq 40$	4.03±2.07	3.65±1.74	1.69±0.44	1.79±0.39
$31 \leq N_{eff} \leq 40$	2.05±0.60	1.58±0.52	1.70±0.13	1.60±0.12

Table 7.3: Equivalent ^{232}Th and ^{238}U levels assuming secular equilibrium for different energy bins. Inward and outward events have been considered separately. There is no indication that there is significant contamination from external $\beta\gamma$ backgrounds.

Radial bin	Extracted ^{232}Th $\times 10^{-15}$g/g	Extracted ^{238}U $\times 10^{-14}$g/g
$0 \leq R_{fit} \leq 250$	0.42±1.08	2.00±0.26
$250 \leq R_{fit} \leq 315$	1.75±0.92	1.53±0.21
$315 \leq R_{fit} \leq 361$	1.56±0.93	1.74±0.20
$361 \leq R_{fit} \leq 397$	2.05±0.90	1.50±0.20
$397 \leq R_{fit} \leq 427$	1.81±0.88	1.63±0.21
$427 \leq R_{fit} \leq 454$	2.48±0.86	1.69±0.20
$454 \leq R_{fit} \leq 478$	3.36±0.96	1.81±0.22
$478 \leq R_{fit} \leq 500$	1.65±0.97	2.48±0.24
$0 \leq R_{fit} \leq 450$	1.75±0.40	1.65±0.09

Table 7.4: Equivalent ^{232}Th and ^{238}U levels assuming secular equilibrium for different radial bins. Each radial bin contains an equal amount of D_2O.

significant and again the value of 31 as the lower N_{eff} threshold is justified as a conservative choice.

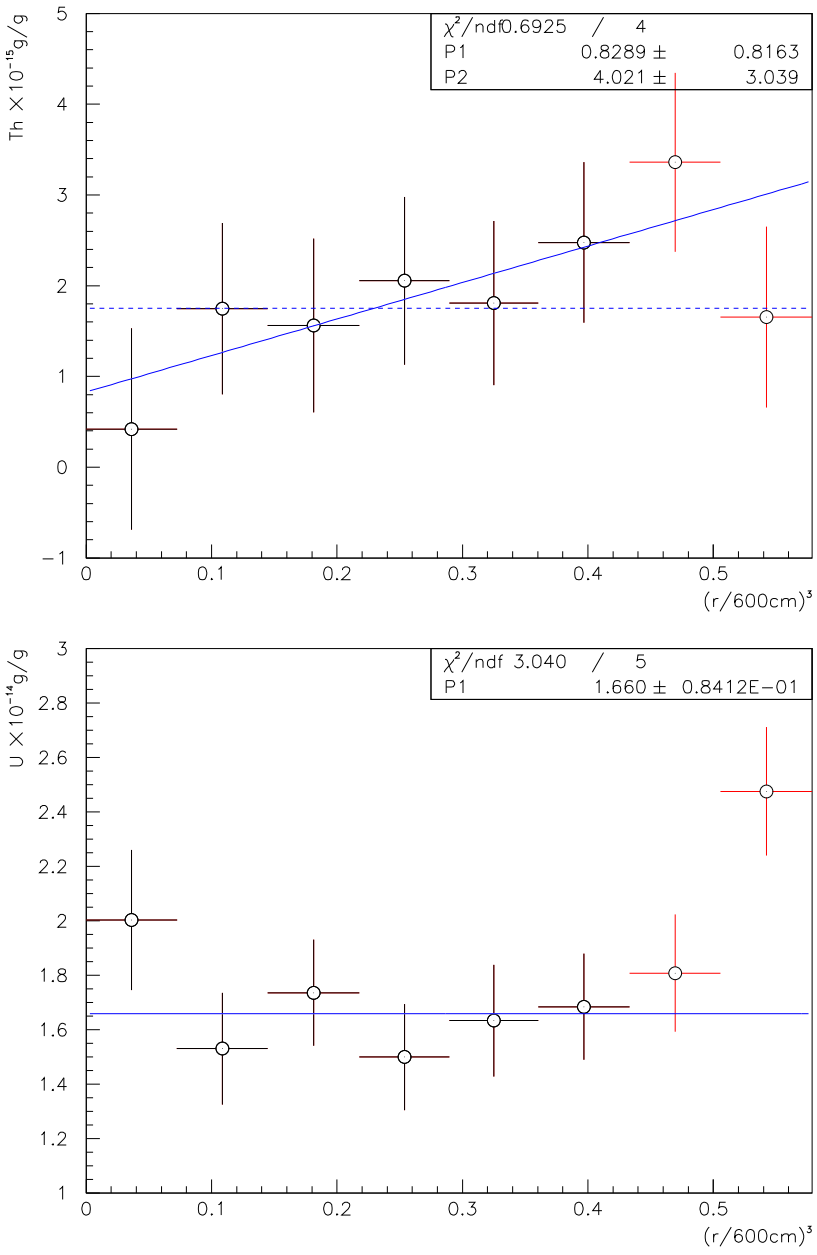

Figure 7.6: The radial profiles of ^{232}Th [top] and ^{238}U [bottom]. For the ^{232}Th a linear fit and a flat fit are shown. Both are entirely consistent. The ^{238}U is consistent with a flat fit, which is shown. The two outermost bins (in red) are not used in the fit to ensure no background $\beta\gamma$ events are included.

7.3.2 Radial Profile

Table 7.4 gives a breakdown of the results for different radial bins (of equal volume), and the results are shown graphically in figure 7.6. The outermost bin extends from 478 cm to 500 cm and a shows a clear excess of ^{238}U. This is attributed to external $\beta\gamma$ events. The other ^{238}U radial bins are consistent with a uniform distribution of ^{214}Bi and demonstrate that a radial cut of $R{\leq}450$ cm ensures that no significant background from external $\beta\gamma$ is present in the volume analysed.

The ^{232}Th results are consistent with a uniform distribution of ^{208}Tl. However, they are also consistent with a distribution of ^{208}Tl which increases with radius. As ^{228}Th is suspected to be plated out on the inside of the acrylic vessel, there is a clear mechanism that would produce a radial profile: the ^{224}Ra produced when ^{228}Th decays would be mobile and mix inwards into the D_2O.

As there is no way to deduce the true radial profile a linear model is assumed and fitted to the data. The outermost two bins are excluded from the fit to ensure that no background $\beta\gamma$ events are included. The result of the fit for the average D_2O ^{232}Th value becomes:

$$\text{Th} \quad : \quad 2.84 \pm 0.70(stat.) \times 10^{-15}\,\text{g/g} \tag{7.6}$$

It is important to stress however, that from the in-situ data alone it is impossible to choose between the value obtained from a linear fit and that obtained from assuming a uniform distribution of ^{208}Tl and ^{214}Bi in the D_2O.

7.3.3 Temporal Variations

As is shown in figure 7.7, the rate of low energy events is not constant. This is almost certainly due to ^{222}Rn which can enter the D_2O through the neck cover gas system and from air trapped in the recirculation loop when an assay is performed.

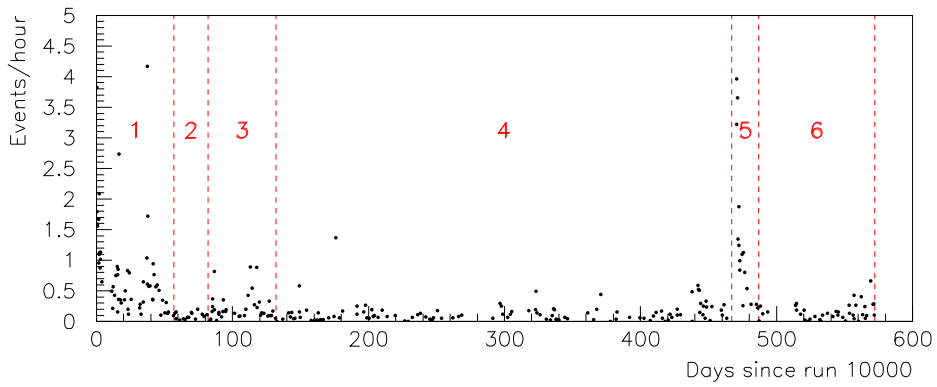

Figure 7.7: The division of the data. Note that the cuts used to produce this plot were not the cuts detailed above, and so the hourly rate presented cannot be compared directly.

Time bin	Begin		End		Livetime (days)
	Day	Run	Day	Run	
1	0	10000	57	10749	39.77
2	57	10756	82	10887	19.02
3	82	10891	132	11431	37.86
4	132	11433	467	15034	163.28
5	467	15065	487	15270	8.47
6	487	15271	572	16013	44.53
Total	0	10000	572	16013	312.94

Table 7.5: Specification of the data division.

The data was divided into the time bins shown in figure 7.7 and detailed in table 7.5. The results obtained for each time bin are shown in table 7.6. The large spikes seen in figure 7.7 are identified as ^{214}Bi by the separation algorithm and this confirms the suspicion that they are caused by ^{222}Rn. The ^{232}Th results are statistically consistent with a constant level of ^{232}Th in the D_2O.

Time bin	Extracted ^{232}Th $\times 10^{-15}$g/g	Extracted ^{238}U $\times 10^{-14}$g/g
1	0.21±1.56	5.55±0.40
2	1.97±1.38	0.74±0.28
3	3.42±1.37	1.52±0.27
4	2.37±0.47	0.38±0.08
5	-0.34±4.05	16.32±1.30
6	0.81±0.72	0.74±0.15
All	1.75±0.40	1.65±0.09

Table 7.6: Equivalent ^{232}Th and ^{238}U levels assuming secular equilibrium for the different time bins.

7.4 Systematic Errors

The systematic errors for the in-situ technique are presented in table 7.7. Each systematic error is discussed below.

The Mean of the θ_{ij} Distribution

The systematic uncertainty was estimated by looking at the difference between the mean θ_{ij} values of ^{16}N high voltage stability run data and the corrected SNOMAN prediction. The largest discrepancy is around 0.3%. This was propagated through the separation algorithm by varying the correction:

$$\theta_{ij} = \theta_{ij}(MC) \times 0.984 + 0.0085 \pm \mathcal{S} \tag{7.7}$$

where $\mathcal{S}$ is the systematic offset ($\mathcal{S} = 0.004$). The systematic error due to the uncertainty in the mean of the θ_{ij} distribution was found to be 17% for ^{232}Th and 3% for ^{238}U. This has been verified independently with a Monte Carlo study [74].

The high θ_{ij} cut method is sensitive only to the number of events above a given θ_{ij} cut. This changed by 3% when the θ_{ij} correction was varied.

Error Source	θ_{ij} separation method		High θ_{ij} method
	^{232}Th error	^{238}U error	neutron error
Mean of θ_{ij} distribution	17%	3%	3%
Energy scale drift	14%	14%	14%
Overall normalisation	10%	10%	10%
Fitter accuracy	3%	3%	3%
High θ_{ij} cut determination	(n/a)	(n/a)	+4.6% −1.4%
Photodisintegration cross section	1%	1%	1%
Total systematic error	24.4%	17.8%	+18.4% −17.8%

Table 7.7: Systematic errors of the in-situ background monitoring technique. The errors were added in quadrature to give the totals.

The Energy Scale Drift

The detector has an energy scale drift of about 2% per year [61]. SNOMAN can be tuned to attempt to eliminate this drift by setting the PMT collection efficiency (P_{eff}) to be time-varying using the following expression:

$$P_{eff} = [1 + P_0 + P_1 \times Jdy(i)] \times 0.5834 \tag{7.8}$$

where P_0 and P_1 are determined by central ^{16}N high voltage stability runs:

$$\begin{aligned} P_0 &= 0.4226 \pm 0.0384 \\ P_1 &= -5.523 \times 10^{-5} \pm 4.080 \times 10^{-6} \end{aligned} \tag{7.9}$$

The uncertainty from the energy scale was estimated by making the assertion that there is, in reality, no drift in the detector and considering the effect of still using the energy estimator N_{eff}. To simulate this, Monte Carlo data sets were generated with the PMT collection efficiency set to either the highest or lowest value in the drift model. After applying N_{eff}, the Monte Carlo normalisation factors changed by 14%.

Overall Normalisation

The overall normalisation systematic error is the discrepancy between the number of events passing the in-situ cuts for data and SNOMAN when SNOMAN has been

tuned to reproduce the ^{16}N source to high precision. This has been quantified with ^{24}Na data (see chapter 6) and is estimated to be $\sim$10% .

Fitter Accuracy

The vertex shift uncertainty of the grid fitter has been estimated to be $\sim$1% [54], which gives a volume uncertainty of $\sim$3%.

High θ_{ij} Cut Determination

The error associated with the choice of the high θ_{ij} cut was estimated by performing the method with cuts of $\theta_{ij} \geq 1.38$ and $\theta_{ij} \geq 1.405$. This yielded an asymmetric error of $^{+4.6}_{-1.4}$%.

Photodisintegration Cross Section

Modelling of the photodisintegration cross section in SNOMAN has an uncertainty of 1% [56]. This small error must be taken into account when determining the number of neutrons that are produced in the D_2O.

7.5 Ex-Situ Measurements

As mentioned briefly in chapter 2, the D_2O purification systems can also be used to assay the D_2O. It is worth considering the results from these assays to check whether they are in agreement with results from the in-situ technique. Estimates of the levels of thorium and uranium in the D_2O from the assays are:

$$\begin{aligned} \text{Th} &: 2.7^{+0.8}_{-0.5}(total) \times 10^{-15}\,\text{g/g} \\ \text{U} &: < 1 \times 10^{-16}\,\text{g/g} \end{aligned} \tag{7.10}$$

This proves conclusively that the uranium chain activity observed by the in-situ method is from ^{222}Rn.

The ex-situ thorium result is higher than the in-situ result by 1.3σ. This is not a significant difference, and if one wished to combine these numbers then simply averaging would be entirely adequate. However, recalling figure 7.6 and the subsequent result of $2.84 \pm 0.70(stat.) \times 10^{-15}$ g/g (equation 7.6) when a linear fit was made suggests that perhaps the radial profile is genuine. Unfortunately, with the information available this cannot be proven.

7.6 Conclusions

The results of the in-situ analysis with full systematic errors are:

$$\begin{aligned} \text{Th} &: 1.75 \pm 0.40(stat.) \pm 0.40(sys.) \times 10^{-15}\,\text{g/g} \\ \text{U} &: 1.65 \pm 0.09(stat.) \pm 0.26(sys.) \times 10^{-14}\,\text{g/g} \end{aligned} \tag{7.11}$$

assuming that the ^{208}Tl and ^{214}Bi are uniformly distributed throughout the entire D_2O and that the decay chains are in secular equilibrium. These levels correspond to neutron production within the D_2O of:

$$\begin{aligned} \text{Th} &: 143.4 \pm 33.0(stat.) \pm 35.0(sys.)\,\text{neutrons} \\ \text{U} &: 173.5 \pm 10.9(stat.) \pm 30.9(sys.)\,\text{neutrons} \\ \text{Total} &: 317.0 \pm 34.8(stat.) \pm 60.8(sys.)\,\text{neutrons} \end{aligned} \tag{7.12}$$

for the full D_2O data set. The systematic error on the total number of neutrons has been calculated assuming that all the systematic errors (excluding the θ_{ij} mean) are completely correlated between ^{232}Th and ^{238}U (and therefore added linearly before being combined in quadrature).

The method that employs a high θ_{ij} cut to equalise the neutron yield gives a neutron production of:

$$\text{Total} : 303.9 \pm 30.9(stat.)\ ^{+49.2}_{-47.4}(sys.)\,\text{neutrons} \tag{7.13}$$

There is no definitive evidence that ^{208}Tl in the D_2O has a non-uniform radial profile. Nevertheless, it is instructive to examine the affect a radial profile would

have on the number of neutrons produced within the D_2O. Assuming that the volume weighted photodisintegration fraction for ^{208}Tl events (equation 7.1) is still valid (which will overestimate the number of neutrons produced as γ-ray losses to the H_2O will be higher) the total number of neutrons produced increases by 28%.

Of these neutrons, about 60% will have the same radial profile as neutrons from neutrino neutral current interactions, and should be identified as such (allowing a simple subtraction). The remaining 40% of neutrons will be produced in the outer volume of the D_2O, closer to the AV. It is likely that a higher fraction of these neutrons will escape the D_2O before capture than those produced uniformly in the D_2O. The remaining neutrons will have a radial profile that is different from neutrons produced from neutrino neutral current interactions and it is not clear how they will be identified. However, this is likely to be a small effect, as the neutrons random walk a considerable distance in the D_2O before they capture. In conclusion, the presence of a radial profile is unlikely to significantly affect the number of neutrons detected and identified as neutrino neutral current interactions.

SSM Subtraction Values

In terms of the BP2000 SSM, the neutrons produced from natural radioactivity in the D_2O (based solely on in-situ measurements) contribute:

$$0.077 \pm 0.008(stat.) \pm 0.015(sys.)\,\mathrm{SSM} \tag{7.14}$$

This should be subtracted from the neutral current interaction measurement.

Chapter 8

The Neutral Current Measurement

As mentioned in chapter 2, the SNO collaboration has published the charged current and elastic scattering interaction rates [49]. The neutral current rate was never stated; only the number of events identified as neutrons.

In this chapter the number of neutrons from the entire D_2O data set is calculated and, armed with the knowledge gained from the in-situ technique discussed in chapter 7, a preliminary neutral current rate is presented. This analysis uses the same event selection, kinetic energy threshold and fiducial volume as SNO's first publication but is not final and is meant only to give a taste of the exciting results promised in the next SNO publication.

8.1 Analysis Overview

A detailed description of the neutrino analysis for the first publication can be found elsewhere [49][54].

The data set analysed here is from data taken between 2nd November, 1999 and 27th May, 2001 which corresponds to a live time of 307.1 days. Backgrounds were removed from the data using the standard data-cleaning tools [70] and the

remaining events reconstructed. A fiducial volume cut of $R \leq 550\,\mathrm{cm}$ and an effective electron kinetic energy threshold of $\mathrm{E} \geq 6.75\,\mathrm{MeV}$ are applied.

The remaining events are separated into the different neutrino interaction types CC, "NC," and ES using an extended maximum likelihood method. (General purpose code for performing extended maximum likelihood was written by the author and installed in SNOMAN). Strictly, the NC component is just the number of neutrons until non-neutrino produced neutrons are subtracted. Signal separation uses PDFs in total energy, radial position and the direction of the event with respect to the Sun. These PDFs are generated using SNOMAN and are shown in figure 8.1.

The PDFs in energy, radial position and direction are combined to give an overall PDF for a neutrino interaction type i=CC, NC or ES in this case:

$$\mathcal{F}_i(\mathrm{NHITS}, R^3, \cos\theta_\odot) = \mathcal{A}_i(\mathrm{NHITS})\mathcal{B}_i(R^3)\mathcal{C}_i(\cos\theta_\odot) \tag{8.1}$$

This factoring ignores correlations between distributions, but this has been demonstrated to be a small effect.

The probability distribution describing a mixture of events (w_i of each type) is given by a linear superposition of the individual probability distributions:

$$\mathcal{G}(\mathrm{NHITS}, R^3, \cos\theta_\odot) = \sum_i w_i \mathcal{F}_i(\mathrm{NHITS}, R^3, \cos\theta_\odot) \tag{8.2}$$

The extended log likelihood function is then given by:

$$\ln\mathcal{L} = \sum_j^{\mathrm{events}} \ln\mathcal{G}(\mathrm{NHITS}, R^3, \cos\theta_\odot) - \sum_i w_i \tag{8.3}$$

This is called the extended likelihood as the w_i's are unconstrained (other than being positive) which allows their fit errors to reflect correlations between the event types. The set of w_i which maximises equation 8.3 is the most likely

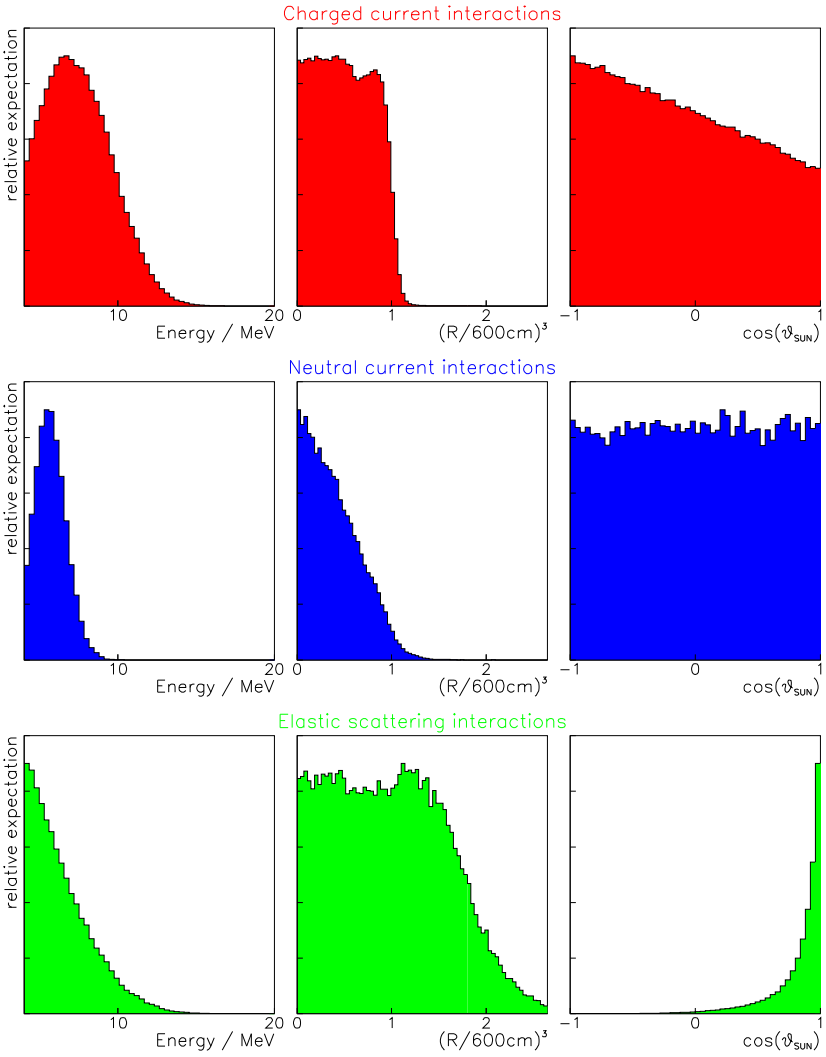

Figure 8.1: The PDFs used in the signal extraction. The charged current events have the ^{8}B energy spectra, are uniform in the D_2O and have the 1-0.340cos$\theta_\odot$ angular distribution. The neutral current events are mono-energetic (from the 6.25 MeV γ-ray from capture on deuterium). They are not uniform in the D_2O as neutrons random walk a significant distance in the D_2O and can escape completely to the H_2O. This random walk also removes any angular correlation with the detected neutrino. The elastic scattering interaction has much poorer energy resolution. It is uniform throughout the D_2O and H_2O volumes, and falls only when the angular acceptance of the PMTs is reached. The electron direction is strongly peaked away from the Sun.

set of event numbers in the data sample. More information on the extended likelihood method can be found in [75].

Once the number of events of each type has been calculated, they are converted to the equivalent BP2000 SSM flux.

8.2 Results

The results from performing the signal extraction on the full D_2O data set are shown in figure 8.2. This yields the following number of neutrons:

$$1.67 \pm 0.42(stat.) \pm 0.12(sys.)\,\mathrm{SSM}$$

where the systematic error includes the theoretical uncertainty in the NC cross section and has been estimated from the CC systematic error assigned in SNO's first publication [49].

The number of neutrons produced by internal radioactivities in the D_2O, as given from the in-situ measurement is:

$$0.08 \pm 0.01(stat.) \pm 0.02(sys.)\ \mathrm{SSM}$$

giving a NC interaction flux of:

$$1.59 \pm 0.42(stat.) \pm 0.12(sys.)\ \mathrm{SSM}$$

to compare to the BP2000 SSM flux of:

$$1.00^{+0.20}_{-0.16}\ \mathrm{SSM}$$

or the charge current interaction rate, as extracted from the signal extraction, of:

$$0.35 \pm 0.03(total)\ \mathrm{SSM}$$

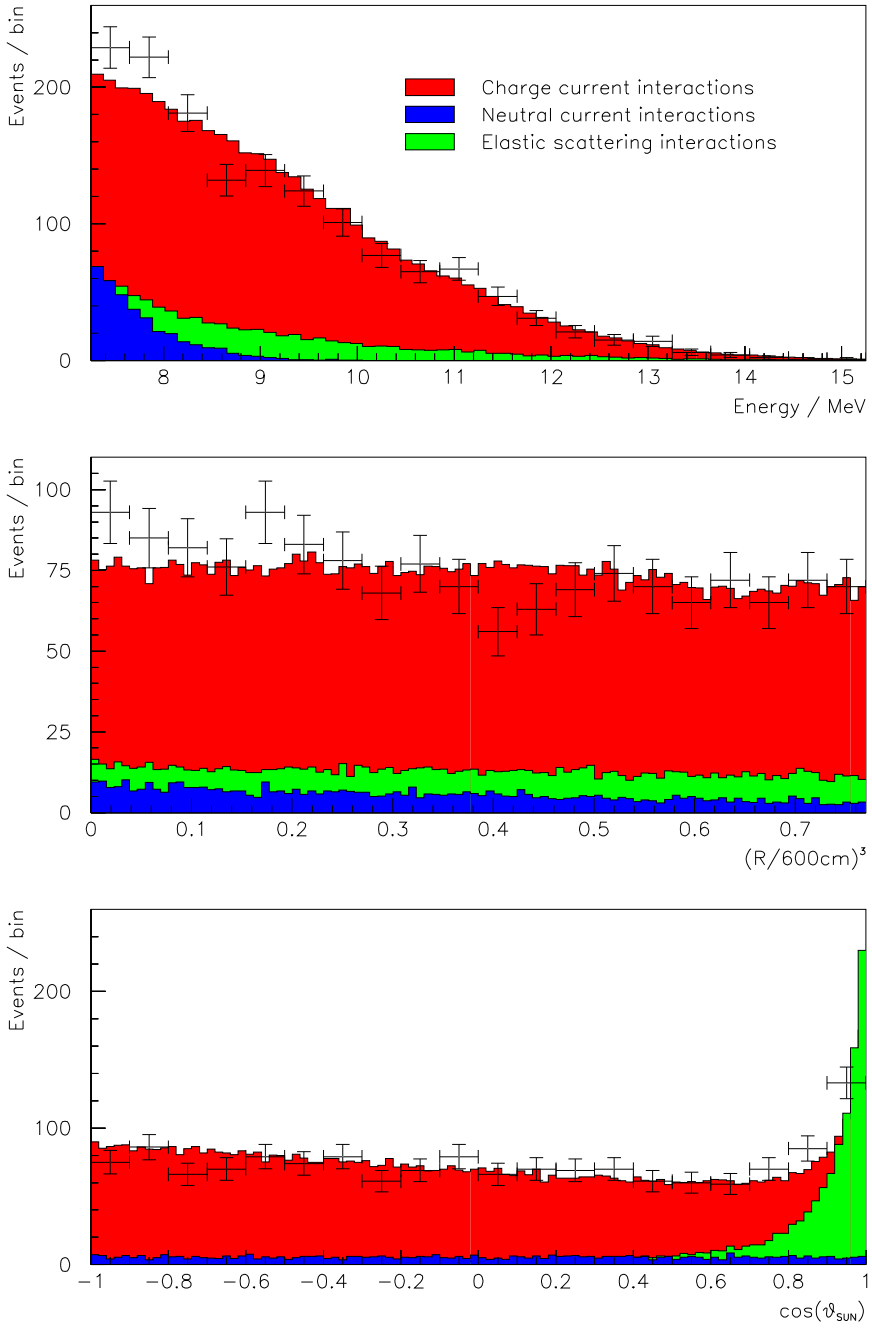

Figure 8.2: The resulting distributions from the likelihood fit, and the data. The total Monte Carlo distributions are colour coded to show the relative signal components.

8.3 Conclusions

As was mentioned before, this is not meant to be a final analysis. Neutron production from γ-rays from the AV and H_2O regions has been neglected (this is expected to contribute much less than D_2O production as these neutrons are produced close to the edge of the D_2O and most will escape before capture on deuterium). It is also possible that other small neutron backgrounds are present.

Nevertheless, the result is interesting. There is a $\sim 2.8\sigma$ difference between the NC and CC rates, suggesting that solar neutrinos have oscillated to other active neutrinos during their journey to the Earth. This result is not as significant (nor as rigorous) as the result presented in chapter 2, but has advantage that both measurements are from the same experiment. When comparing the NC rate to the BP2000 SSM prediction, the NC rate is just over 1σ higher. These numbers are therefore in good agreement, indicating that the BP2000 SSM prediction is correct.

Work is currently being done by the SNO collaboration, and results from the full data set with a lowered energy threshold will soon be presented. These results should have statistical uncertainties comparable to the systematic uncertainties, and be much more robust and significant.

Chapter 9

Thesis Conclusions

This thesis covers a number of topics which all contribute to the measurement of the neutral current charge interaction. Chapter 3 introduces the History Calibration which successfully corrects a fault in the PMT timing calibration. Applying the HCA to the neutrino data did not, contrary to expectations, result in a dramatic reduction of events reconstructing within the fiducial volume. This puzzling result, which appeared to directly contradict the predictions made by the low rate ^{16}N source, is explained. Confidence in fitter performance is restored which allows fitter accuracy to be estimated, crucial for all neutrino analyses.

Chapter 4 presents the upgrades to the neutron transport code in SNOMAN made by the author. The upgrades allow the code to fulfil all the requirements of the SNO experiment. A comparison of the current and a new ^{36}Cl decay cascade is made, and it is concluded that the differences are negligible. A comparison of salt data with SNOMAN predictions gives excellent agreement, with the overall neutron capture efficiency accurate to $\sim$5%.

Chapters 5 and 6 discuss the choice and benefits of using NaCl salt as the salt additive in the D_2O. The ^{24}Na production rate in the D_2O recirculation loop is estimated in chapter 5 and found to be acceptably low. This led to the approval and deployment of NaCl in the D_2O on 28th May, 2001.

NaCl in the D_2O gave the unanticipated benefit of activating ^{24}Na in the D_2O for use as a calibration source. The analysis of this source is presented in chapter 6. Comparisons between data and SNOMAN show good agreement. The total ^{24}Na produced by deploying the superhot thorium source is estimated from the source strength and from the number of neutrons produced by 2.75 MeV γ-rays from ^{24}Na decays. The latter of these two methods makes use of the neutron validation of chapter 4. The ratio of observed events to the total number of decays, as estimated from these two methods, is calculated and compared with SNOMAN. It is concluded that SNOMAN can be used to estimate this ratio to better than 10%, with the agreement using the source strength estimate better than 1%.

Chapter 7 presents a method of determining the number of ^{208}Tl and ^{214}Bi decays within the D_2O using Čerenkov light produced in the $\beta\gamma$ decays of these particles. This is of critical importance to any measurement of the neutral current interaction. The result obtained in chapter 6 is used to demonstrate that the overall normalisation predicted by SNOMAN is valid. Assuming that radioactivities are uniform in the D_2O, the equivalent thorium and uranium concentrations are:

$$\begin{aligned} ^{232}\mathrm{Th} &: 1.75 \pm 0.40(stat.) \pm 0.40(sys.) \times 10^{-15}\,\mathrm{g/g} \\ ^{238}\mathrm{U} &: 1.65 \pm 0.09(stat.) \pm 0.26(sys.) \times 10^{-14}\,\mathrm{g/g} \end{aligned} \tag{9.1}$$

corresponding to a total neutron production of:

$$\begin{aligned} 317.0 \pm 34.8(stat.) \pm 60.8(sys.) &\quad \text{neutrons} \\ 0.077 \pm 0.008(stat.) \pm 0.015(sys.) &\quad \text{BP2000 SSM} \end{aligned} \tag{9.2}$$

Finally, chapter 8 presents the first neutral current analysis of the full D_2O data set. The NC flux obtained is:

$$1.59 \pm 0.42(stat.) \pm 0.12(sys.) \quad \text{SSM} \tag{9.3}$$

When combined with the CC flux measurement from SNO, this result is evidence at the 2.8σ level that solar neutrinos oscillate to active flavours during their journey to the Earth and that the predicted BP2000 SSM ^{8}B neutrino flux is correct.

Appendix A

Derived Quantity Definitions

A.1 The Isotropy Parameter θ_{ij}

The isotropy of an event can be quantified by the θ_{ij} parameter. To form θ_{ij} the event must be reconstructed. Thus θ_{ij} is usually referred to as a high level parameter. Once event reconstruction information is available, the mean of the two point angular correlation function of PMT hits is formed. Only PMTs with time residuals of less than 9 ns contribute to the correlation function. This reduces the impact of scattering and noise. The definition of θ_{ij} is shown in figure A.1.

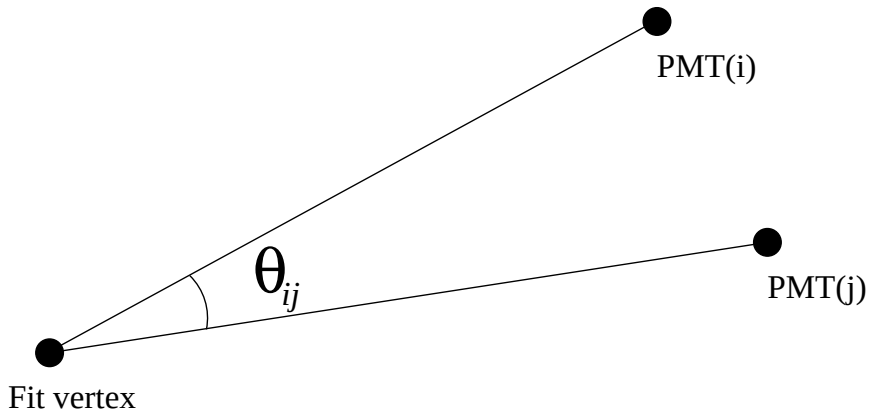

Figure A.1: The definition of θ_{ij}. The indices i and j run over hit PMTs.

A.2 The In Time Ratio (ITR)

The In Time Ratio (ITR) is a measure of the quality of a fit. It is a simple, yet effective, way of rejecting instrumental backgrounds and poorly reconstructed Čerenkov events.

ITR is defined as the ratio of the number of PMT hits within an asymmetric time residual window to the total number of PMT hits passing the full timing calibration. The residual time window is defined as -2.5 ns $\rightarrow$ 5.0 ns. It is asymmetric because scattering produces a late tail on the PMT hit time distribution.

A.3 The Energy Estimator N_{eff}

N_{eff} is a NHITS (rather than N_{PROMPT}) based energy estimator [76]. It corrects an event's NHITS by subtracting the noise rate component, correcting for the number of PMTS operating and removing the energy drift of the detector [61]:

$$N_{eff} = \left[\frac{9453}{\lambda}\left(\mathrm{NHITS} + R - \delta\right)\right] / P_{eff}$$

where λ is the number of PMTS operating, δ is the noise rate, R is a random number between -0.5 and 0.5 (to convert N_{eff} to a continuous variable) and P_{eff} is the PMT collection efficiency.

Appendix B

Glossary

ADC	Analogue to digital converter.
AV	The acrylic vessel.
BP2000	The Bahcall Pinsonneault 2000 standard solar model [9].
Builder	A program that builds information from the DAQ into full detector events.
CC	Charged current interaction: $\nu_e + \mathrm{d} \rightarrow \mathrm{p} + \mathrm{p} + e^-$
DAMN	Data analysis mask number.
DAQ	Data acquisition system.
DB	Daughter board.
ECA	Electronics calibration.
ENDF	Evaluated nuclear data file.
ES	Elastic scattering interaction: $\nu_x + e^- \rightarrow \nu_x + e^-$
ESUM	The analogue sum of PMT signals, for use in triggering.
FEC	Front end card.
FPGA	Field programmable gate array.

GPS Global positioning system (10 MHz clock).

GT Global trigger.

GTID Global trigger ID. A unique number for an event in a run.

HCA History calibration.

HCAG HCA global calibration constants.

HCAS HCA status file.

ITR In time ratio.

Just So^2 A region of MSW parameter space that can explain the solar neutrino problem.

LMA Large mixing angle solution. A region of MSW parameter space that can explain the solar neutrino problem.

LOW The low Δm^2 solution. A region of MSW parameter space that can explain the solar neutrino problem.

MC Monte Carlo.

MSW Mikheyev, Smirnov and Wolfenstein effect.

NC Neutral current interaction: $\nu_x + \mathrm{d} \rightarrow \nu_x + \mathrm{p} + \mathrm{n}$

NCD Neutral current detector.

N_{eff} NHITS based energy estimator.

NHITS Th number of hit inward looking PMTs.

Orphan A PMT hit or hits which the builder has failed to build into the detector event in which they were generated.

OWL Outward looking PMT.

PCA PMT calibration.

PED-GT The delay between the pedestal and the GT signal.

PMT Photomultiplier tube.

PMTIC PMT interface card.

PSUP The PMT support structure.

Pulse GT A diagnostic trigger.

QHL High gain, long integration time charge measurement.

QHS High gain, short integration time charge measurement.

QLX Low gain, variable integration time charge measurement.

QUSN7 The CMOS member of the SNO chipset.

RAA Random access analyser. A SNOMAN processor.

RO Reverse osmosis system.

SHARC SNO hardware acquisition and readout control.

SMA Small mixing angle solution. A region of MSW parameter space that can explain the solar neutrino problem.

SNO The Sudbury Neutrino Observatory.

SNOD The discriminator member of the SNO chipset.

SNOINT The integrator member of the SNO chipset.

SNOMAN SNO Monte carlo and ANalysis. The Monte Carlo and analysis package for the SNO experiment.

SNU Solar neutrino unit. Equivalent to 10^{-36} captures per target atom per second.

SSM Standard solar model.

SUF Seeded ultrafiltration system.

TAC Time to amplitude converter. Also the name given to the uncalibrated time measurement for a PMT.

θ_{ij} A measure of the isotropy of the hit pattern of an event.

VAC Vacuum oscillation solution. A region of MSW parameter space that can explain the solar neutrino problem.

XZDAB An extended ZDAB bank such that it contains HCA calibration information.

ZDAB Zebra data acquisition/analysis bank.

Appendix C

The DAMN Cuts

This is a short summary of the DAMN (Data Analysis Mask Numbers) cuts used in SNO in general, and this thesis in particular. For a full discussion of these cuts, including their motivation, readers should consult [70] and the references therein.

AMB This cut uses information from the analogue measurement board to place cuts based on the value of the integral and the peak of the ESUM trigger signal normalised to the number of channels hit.

Burst This cut removes all events in a time window during which the event rate is greater than 3 kHz, with the burst threshold set at 3 events.

Crate isotropy This cut is aimed at electronic pickup and removes events in which more than 70% of hits occur on one crate and more than 80% of those hits occur on two adjacent cards, including a wrap around to count cards 0 and 15 as adjacent.

ESUM This cut removes events with only ESUM triggers.

Flasher The flasher geometry cut. This cut removes "flasher" events.

	These are events in which a PMT has emitted light. The hit patterns of these events are considerably different from Čerenkov events and this is exploited by the cut.
FTS	The fitterless timespread cut. This removes events where the median time difference of hit PMT pairs within 3 m of each other is greater than 6.8 ns.
ITC	In time channel. This cut removes events which have less than 60% of the hits within a 93 ns coincidence. The number of in time hits is determined by sliding the 93 ns window over the timing distribution.
JUNK	This cut removes orphans, ECA data and events which contain the same PMT more than once (due to builder problems).
Muon tag	This tags an event as a muon if 5 or more OWL tubes have fired, more than 150 inner PMTs have fired, and the event does not fail the neck cut.
Muon short	This cut removes all events within 20 seconds of a muon tag.
Muon long	This cut removes all events within 60 seconds of a muon tag.
NECK	This cut is removes "neck" events. These are events suspected to be due to light generated at the air water interface in the neck of the AV. The cut requires that the neck tubes, dedicated veto tubes above the neck, have fired.
NHITS burst	This cut removes all events in a time window during which the rate of $\geq$40 NHITS events is greater than 1.5 Hz, with the burst threshold set at 6 events.
OWL	This tags events in which 3 or more OWL tubes have fired.

OWL ESUM This cut removes with only OWL ESUM triggers.

Q/NHIT This cut removes events with anomalously low average charge per PMT hit.

QCLUSTER This cut removes events that have more than 6 hits in a paddle card or more than 200 hits in a single crate.

QvT This cut removes events with a single high charge, very early PMT hit is present.

Retrigger This cut removes any event that occurs within 5 μs of a previous event.

Salt blindness This 'cut' will remove the muon follower events purposefully left in the salt neutrino data set to remove the blindness of the salt neutrino analysis.

Zero zero This cut removes all events which have GTIDs that have their last eight bits set to zero (which can indicate builder problems).

Bibliography

[1] B. Lundberg for the DONUT collaboration. *Status of DONUT.* In *Neutrinos 2000, Proceedings of the XIXth International Conference on Neutrino Physics and Astrophysics*, editors J. Law, R. W. Ollerhead and J. J. Simpson, Nuclear Physics B (Proc. Suppl.) **91**, 233 (January 2001).

[2] The LEP collabortaion. *Results from LEP concerning the width of the Z° from L3, ALEPH, OPAL and DELPHI.* Physics Letters B 509,519,530,539 (1989).

[3] J. Bonn *et al. The Mainz Neutrino Mass Experiment.* In *Neutrinos 2000, Proceedings of the XIXth International Conference on Neutrino Physics and Astrophysics*, editors J. Law, R. W. Ollerhead and J. J. Simpson, Nuclear Physics B (Proc. Suppl.) **91**, 273 (January 2001).

[4] V. M. Lobashev *et al. Direct Search for Neutrino Mass and Anomaly in the Tritium Beta-Spectrum: Status of the "Troitsk Neutrino Mass" Experiment.* In *Neutrinos 2000, Proceedings of the XIXth International Conference on Neutrino Physics and Astrophysics*, editors J. Law, R. W. Ollerhead and J. J. Simpson, Nuclear Physics B (Proc. Suppl.) **91**, 280 (January 2001).

[5] D. E. Groom *et al. Review of particle physics.* The European Physics Journal C **15**, 1 (2000).

[6] J. M. Roney. *Review of the Tau Neutrino Mass.* In *Neutrinos 2000, Proceedings of the XIXth International Conference on Neutrino Physics and*

Astrophysics, editors J. Law, R. W. Ollerhead and J. J. Simpson, Nuclear Physics B (Proc. Suppl.) **91**, 287 (January 2001).

[7] H. Ejiri. *Double Beta Decays and Neutrinos.* In *Neutrinos 2000, Proceedings of the XIXth International Conference on Neutrino Physics and Astrophysics*, editors J. Law, R. W. Ollerhead and J. J. Simpson, Nuclear Physics B (Proc. Suppl.) **91**, 255 (January 2001).

[8] J. N. Bahcall. *Neutrino Astrophysics* (Cambridge University Press, 1989).

[9] J. N. Bahcall, M. Pinsonneault and S. Basu. *Solar models: current epoch and time dependences, neutrinos, and helioseismological properties.* Astrophysics Journal **555**, 990 (2001). [astro-ph/0010346 v2]

[10] *The OPAL Opacity Code.* Details can be found at:
`http://www-phys.llnl.gov/Research/OPAL/index.html`

[11] J. N. Bahcall. Available at `http://www.sns.ias.edu/~jnb/`

[12] B. Cleveland *et al. Measurement of the solar electron neutrino flux with the Homestake chlorine detector.* Astrophysics Journal **496**, 505 (1998).

[13] J. Abdurashitov *et al. Measurement of the solar neutrino capture rate with gallium metal.* Physical Review C **60**, 055801 (1999).

[14] W. Hampel *et al. GALLEX solar neutrino observations: results from GALLEX IV.* Physics Letters B **447**, 127 (1999).

[15] M. Altmann *et al. GNO solar neurtino observations: results from GNO I.* Physics Letters B **490**, 16 (2000).

[16] V. Gavrin for the SAGE collaboration. *Solar neutrino results from SAGE.* In *Neutrinos 2000, Proceedings of the XIXth International Conference on Neutrino Physics and Astrophysics*, editors J. Law, R. W. Ollerhead and J. J. Simpson, Nuclear Physics B (Proc. Suppl.) **91**, 36 (January 2001).

[17] E. Bellotti for the GNO collaboration. *First results from GNO.* In *Neutrinos 2000, Proceedings of the XIXth International Conference on Neutrino Physics and Astrophysics*, editors J. Law, R. W. Ollerhead and J. J. Simpson, Nuclear Physics B (Proc. Suppl.) **91**, 44 (January 2001).

[18] J. V. Jelley. *Čerenkov radiation* (Pergamon Press, London, 1958).

[19] Y. Fukuda *et al. Solar Neutrino Data Covering Solar Cycle 22.* Physical Review Letters **77**, 1683 (1996).

[20] S. Fukuda *et al. Solar ^8B and hep Neutrino Measurements from 1258 Days of Super-Kamiokande Data.* Physical Review Letters **86**, 5651 (2001). [hep-ex/0103032]

[21] N. Hata and P. Langacker. *Solutions to the solar neutrino anomaly.* Physical Review D **56**, 6107 (1997). [hep-ph/9705339]

[22] B. Pontecorvo. *Neutrino experiments and the problem of conservation of leptonic charge.* Soviet Physics JETP **26**, 984 (1968).

[23] V. Gribov and B. Pontecorvo. *Neutrino Astronomy and Lepton Charge.* Physics Letters B **28**, 493 (1969).

[24] Z. Maki, M. Nakagawa and S. Sakata. Progress of Theoretical Physics **28**, 870 (1962).

[25] B. Kayser. *On the quantum mechanics of neutrino oscillation.* Physical Review D **24**, 110 (1981).

[26] L. Wolfenstein. *Neutrino oscillations in matter.* Physical Review D **17**, 2369 (1978).

[27] S. Mikheyev and A. Smirnov. *Resonance enhancements of oscillations in matter and solar neutrino spectroscopy.* Soviet Journal of Nuclear Physics **42**, 913 (1985).

[28] S. Mikheyev and A. Smirnov. *Resonant Amplifications of ν-Oscillations in Matter and Solar-Neutrino Spectroscopy.* II Nuovo Cimento **9C**, 17 (1986).

[29] J. N. Bahcall, P. I. Krastev and A. Y. Smirnov. *Solar neutrinos: global analysis and implications for SNO.* The Journal of High Energy Physics **0105**, 015 (2001). [hep-ph/0103179]

[30] G. Fogli *et al. Model-dependent and independent implications of the first Sudbury Neutrino Observatory results.* Physical Review D **64**, 093007 (2001). [hep-ph/0106247]

[31] M. Apollonio *et al. Limits on Neutrino Oscillations from the CHOOZ Experiment.* Physics Letters B **466**, 415 (1999). [hep-ex/9907037]

[32] H. H. Chen. *Direct Approach to Resolve the Solar-Neutrino Problem.* Physical Review Letters **55**, 1534 (1985).

[33] J. Boger *et al. The Sudbury Neutrino Observatory.* Nuclear Instruments and Methods in Physics Research A **449**, 172 (2000). [nucl-ex/9910016]

[34] E. Beier *et al. Performance of the Electronics for the Sudbury Neutrino Observatory.* Technical report SNO-STR-98-002, The Sudbury Neutrino Observatory (1998).

[35] D. Cowen *et al. The Sudbury Neutrino Observatory Electronics Chain.* Technical report, The Sudbury Neutrino Observatory (1994).

[36] M. Neubauer. *Evidence for $\nu_e \rightarrow \nu_{\mu,\tau}$ Oscillations through Measurement of the ^{8}B Solar Neutrino Flavor Content at the Sudbury Neutrino Observatory.* Ph.D. thesis, University of Pennsylvania (2001).

[37] J. Klein *et al. The SNO Trigger System.* Technical report SNO-STR-97-035, The Sudbury Neutrino Observatory (1997).

[38] K. Schaffer *et al. The Orphan Document.* Technical report, The Sudbury Neutrino Observatory (June 2001).

[39] The SNO Water Group. *Scientific Review of SNO Water Systems.* Technical report, The Sudbury Neutrino Observatory (April 1996). Edited by A. J. Noble.

[40] T. C. Andersen *et al. A radium assay technique for the Sudbury Neutrino Observatory.* To be submitted to Nuclear Instruments and Methods in Physics Research A (2001).

[41] R. A. Black *et al. Measurement of radium concentration in water with Mn-coated beads at the Sudbury Neutrino Observatory.* To be submitted to Nuclear Instruments and Methods in Physics Research A (2001).

[42] J. Cameron *et al. Study of High Voltage-Dependent Phenomena in the SNO Detector.* Technical report, The Sudbury Neutrino Observatory (1999).

[43] P. Vogel and J. Beacom. *The angular distribution of the reaction* $\bar{\nu}_e + p \rightarrow e^+ + n$. Physical Review D **60**, 053003 (1999). [hep-ph/9903554]

[44] Felix Boehm and Petr Vogel. *Physics of Massive Neutrinos* (Cambridge University Press, 1991), 2nd edn.

[45] The SNO Collaboration. *The SNOMAN User's Manual.* Available with the latest SNOMAN release.

[46] The SNO Collaboration. *The SNOMAN Programmer's Manual.* Available with the latest SNOMAN release.

[47] The SNO Collaboration. *The SNOMAN Companion.* Available with the latest SNOMAN release.

[48] CERN Program Library Long Writeups Q100/Q101. *ZEBRA* (1995). `http://wwwinfo.cern.ch/asdoc/zebra_html3/zebramain.html`

[49] Q. Ahmad *et al. Measurement of the rate of* $\nu_e + d \rightarrow p + p + e^-$ *interactions produced by* ^8B *solar neutrinos at the Sudbury Neutrino Observatory.* Physical Review Letters **87**, 071303 (2001). [nucl-ex/0106015]

[50] M. Butler, J. W. Chen and X. Kong. *Neutrino-deutron scattering in effective field theory at next-to-next-to leading order.* Physical Review C **63**, 035501 (2001).

[51] S. Biller *et al. SNO Electronic Calibration Constants.* Technical report SNO-STR-01-005, The Sudbury Neutrino Observatory (2001).

[52] James R. N. Cameron. *The Photomultiplier Tube Calibration of the Sudbury Neutrino Observatory.* D.Phil. thesis, Wolfson College, Oxford University (2001).

[53] M. Neubauer. *Reconstruction Plots.* Manhattan logbook entry (April 2001).

[54] SNO Collaboration. *Analysis for First Solar Neutrino Paper.* Technical report, The Sudbury Neutrino Observatory (May 2001).

[55] *MCNP, A Monte Carlo N-Particle Transport Code System (version 4C).* Los Alamos National Laboratory (November 1993). `http://www-xdiv.lanl.gov/XCI/PROJECTS/MCNP/`

[56] M. J. Lyon. *Neutron Transport in the Sudbury Neutrino Detector.* D.Phil. thesis, Balliol College, Oxford University (1996).

[57] M. Fowler and J. B. Wilhelmy. *Preparation of Acrylic Encapsulated Radioactive Calibration Sources for SNO.* Technical report SNO-STR-99-016, The Sudbury Neutrino Observatory (1999).

[58] M. R. Dragowsky. *Pure D_2O Neutron Calibration Results.* Technical report, Los Alamos National Laboratory (July 2001).

[59] M. R. Dragowsky *et al. Measurement of the ^{252}Cf Acrylic Source Standard.* Technical report, Los Alamos National Laboratory (August 2001).

[60] B. A. Moffat. *The Optical Calibration of the Sudbury Neutrino Observatory.* Ph.D. thesis, Queen's University (July 2001).

[61] A. Hamer. *Temporal Dependence of the Nhit Energy Scale.* Technical report, The Sudbury Neutrino Observatory (December 2001).

[62] The Salt Review Committee. *Salt Review.* Technical report SNO-STR-2000-03, The Sudbury Neutrino Observatory (1999).

[63] R. B. Firestone. *Table of Isotopes* (Wiley-Interscience, 1996), 8th edn. (cdrom).

[64] M. Isaac. *High Energy Gamma-Rays measurements in the SNO Cavity.* Technical report SNO-STR-97-09, The Sudbury Neutrino Observatory (1997).

[65] R. K. Heaton. *The alpha-induced Thick Target Yield for Light Elements.* Master's thesis, Queen's University (1994).

[66] M. C. Browne. *Preparation for the deployment of the Neutral Current Detectors for the Sudbury Neutrino Observatory.* Ph.D. thesis, North Carolina State University (1999).

[67] A. Noble. Private communication.

[68] N. Jelley, G. McGregor and H. Nguyen. *^{24}Na Containerless Source Proposal.* Technical report, The Sudbury Neutrino Observatory (July 2001).

[69] A. W. P. Poon. *Energy Calibration of the Sudbury Neutrino Observatory using Monoenergetic Gamma-Ray Sources.* Ph.D. thesis, The University of British Columbia (1998).

[70] N. K. McCauley. *Producing a Background Free Data Set for Measurement of the Charge Current Flux and Day-Night Asymmetry at the Sudbury Neutrino Observatory.* D.Phil. thesis, The Queen's College, Oxford University (2001).

[71] Xin Chen. *Monte Carlo Simulations and Analyses of Backgrounds in the Sudbury Neutrino Observatory.* D.Phil. thesis, Balliol College, Oxford University (1997).

[72] G. Doucas *et al. Light concentrators for the Sudbury Neutrino Observatory.* Nuclear Instruments and Methods in Physics Research A **370**, 579 (1996).

[73] S. J. Brice. *Monte Carlo and Analysis Techniques for the Sudbury Neutrino Observatory.* D.Phil. thesis, Balliol College, Oxford University (1996).

[74] A. W. P. Poon. *Dependence of the Extracted* ^{232}Th *and* ^{238}U *on the Systematic Uncertainty in the* θ_{ij} *Distribution.* Technical report, The Sudbury Neutrino Observatory (2001).

[75] Louis Lyons. *Statistics for nulear and particle physicists* (Cambridge University Press, 1986).

[76] M. Smith. Private communication.